

Ocean Eddy-Mean Flow Interactions Over Topography

Oriel College

University of Oxford

Author:

Mark Edward Forshaw

Degree:

M. Sc. by Research

Pages: 104

Ocean Eddy-Mean Flow Interactions Over Topography

M. Sc. by Research

Mark Edward Forshaw

Oriel College

Abstract

Climate modelling fails to accurately represent the global oceans in a number of ways. One area where models are consistently flawed is in the Atlantic Water Layer of the Arctic Ocean, by failing to predict the predominantly cyclonic circulation observed. In this thesis we discuss the most likely explanation for this failing, namely that most, if not all, climate models fail to have a physically consistent representation of mesoscale eddies, whether resolved or parameterised.

We will explore recent developments in eddy-mean interaction theory, and use it to investigate eddy-mean interactions over topography. To do this we will use an idealised stacked shallow water model in which large topographic slopes and realistic mesoscale eddy fields can be well represented. The effect of these eddy fields on the larger scale is diagnosed using the theory to determine how the eddy-mean interaction is characterised by both the topography and the properties of the eddy field.

It is shown that the eddy energy and eddy enstrophy provide useful bounds. In the specific configurations explored in this thesis, the eddy energy is shown to be a highly constraining bound and hence an important factor for the structure of the eddy stresses. Also, despite the two definitions of mean potential vorticity allowed by eddy-mean interaction theory, we show that these definitions are effectively identical in our configurations, and hence that the eddy enstrophy bound is applicable to both definitions. These results will hopefully contribute to developing a dynamically-consistent parameterisation of eddies over variable topography. And hence, help to improve the ability of ocean models to reproduce circulation patterns observed in the Atlantic Water Layer of the Arctic.

Acknowledgements

I would first like to thank my thesis advisor, Professor David P Marshall of the Atmospheric, Oceanic and Planetary Physics Department (AOPP) at the University of Oxford. The construction of this thesis has been fraught with many of my own personal issues and I am grateful for the patience and support that David has shown me; especially when I personally struggled to find the value in my work. He also steered me in the right direction whenever it was unclear how to progress.

In the same vain, I would also like to thank the entire Ocean Climate research group at Oxford. The welcoming and friendly nature of the group, along with the exciting and interesting science that happens within, were a strong motivation for completing this thesis. Specifically, I would like to thank Fenwick Cooper for our deep conversations about science over a pint at the end of the week, and Edward Doddridge for his enthusiasm in involving the group in enjoyable activities such as punting and croquet.

As with all the endeavours and decisions I make throughout my life, I am extremely grateful for the unwavering support and encouragement of my family. I am especially thankful to my parents, who have had the unenviable task of delivering encouragement when I have been most despondent and support when I have had little confidence in my own abilities and decisions.

Finally, I would also like to thank my friends who have provided continuous moral support over the past few years; in particular my fellow members of Oriel College and AOPP who have become some of my closest friends during my time at Oxford. I would like to thank them for their unwavering belief in me and the encouragement they have freely given when I have needed it.

Chapter 1

Introduction

1.1 Arctic Ocean

Despite its small size (only 3% of the Earth's surface), the Arctic Ocean is a disproportionately important part of the global ocean and has the potential to affect the world's climate in major ways. Located above 70 °N, the Arctic is characterised by its seasonally varying ice cap. This ice cap, along with its counterpart in the Antarctic, is a major contribution to the planet's albedo as well as being a huge reservoir of freshwater. The Arctic Ocean is a key component in how the polar ice cap interacts with the climate and, in turn, how the climate affects the ice cap. The Arctic itself is a highly stable body of water with strong stratification, which means that the water column can be divided into well defined water masses. The Arctic Ocean is commonly divided into four different layers (Figure 1.1.1): the polar mixed layer, which is a well mixed layer in contact with the atmosphere and surface ice; the halocline, a reservoir of fresh water penetrating down to around 200 m, which acts as a buffer between the sea ice and the Atlantic Water Layer (AWL); the AWL, which is body of warm salty water which originates from the North Atlantic and Nordic Sea via Fram Strait and typically sits at around 400 m deep; and finally, the Polar Deep Water, defined by the water masses that aren't able to communicate freely with the global ocean due to being trapped by the Arctic basin walls.

Because of the strong stratification, forcing from the ocean surface struggles to pen-

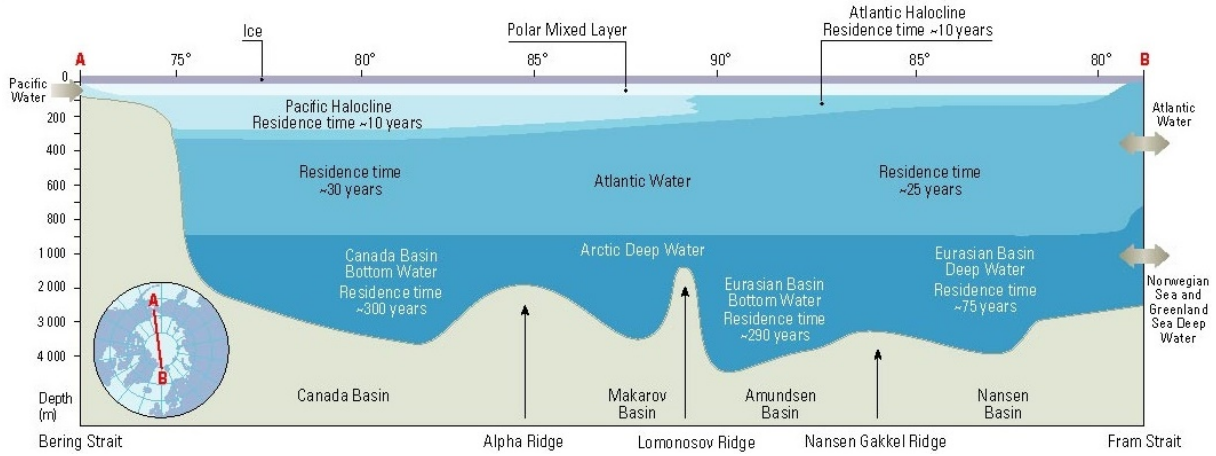


Figure 1.1.1: A schematic representation of the four-layer structure of the Arctic Ocean, with the Mixed Layer and Halocline above the Atlantic Water and Arctic Deep Water (Aagaard and Carmack (1989)). The residence time for the different water masses are also shown (Bönisch and Schlosser (1995)). Reproduced from Wilson et al. (1998).

etrate deep into the ocean; and so, whether forced directly by wind or by sea ice stress, the circulation directly forced from the surface is contained within the polar mixed layer and halocline in the upper 200 m of the Arctic Ocean. This surface circulation has been well documented by observations from cruises and moorings dropped from the ice shelf or deployed on the shallower continental shelves (Gerdes and Schauer (1997), Jones (2001)). On the other hand, it is a very different story for the circulation in the AWL and lower layers. Observations made inside the Arctic's basins rarely are able to profile the structure and circulation below 500m although much progress has been made here in the past decade. This lack of observations means that we still only have a sense of the circulation of the AWL and the deep waters. The observations we do have infer stable cyclonic rim currents about each of the basins in the AWL and it is believed that this trend extends through the deep water to the ocean floor (Figure 1.1.2). It is apparent that the surface flows have little correlation with these deep circulations, this is because of the strong stratification in the halocline, and hence only leaves a handful of other possibilities for determining the processes that set the deep water circulation.

There has been much discussion of how the fluxes in and out of the Arctic could influence the circulation, for example, by forcing a balance of potential vorticity (PV) within the region by the fluxes of PV though the boundaries. Yang (2005) demonstrates,

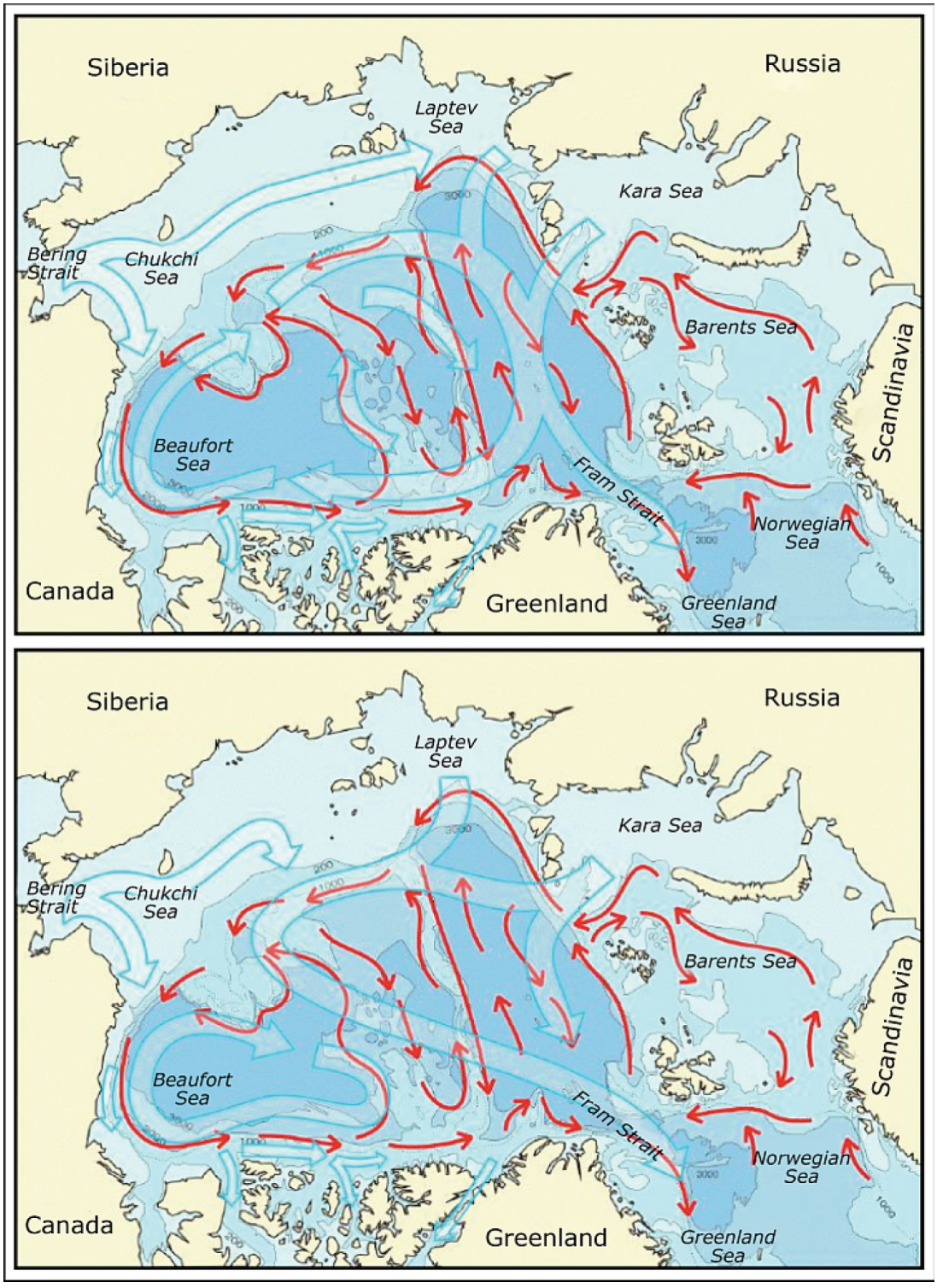


Figure 1.1.2: Two freshwater layer regimes (light blue arrows) overlaying the cyclonic rim currents of the AWL (red arrows). Whilst the Freshwater regimes are vastly different from each other, the AWL is unaffected and remains persistently cyclonic. Topography is represented in the background running from shallow water (light blue) to deep water (dark blue). Reproduced from Proshutinsky et al. (2005).

how in an idealised barotropic model of a basin the circulation in the basin can be switched between cyclonic and anti-cyclonic circulations (Figure 1.1.3), by controlling the flux of PV through inflows and outflows at the boundary. This principle suggests that the persistent cyclonic nature of the AWL is induced by a net influx of PV via the Arctic Gateways.

Fortunately, permanent moorings covering the majority of the ocean gateways into the Arctic Ocean have built up a detailed picture of the transport in and out of the Arctic Ocean (Tsubouchi et al. (2012), Figure 1.1.4). The net advective flux of PV into the Arctic is then estimated by integrating the distributions of PV fluxes multiplied by the volume transports through the open boundaries. Whilst there is a tendency to infer a net positive influx of PV, the results are not convincing; Münchow et al. (2006) show that by including the Canadian Archipelago in the Yang (2005) calculation, the flux can be negated whilst Tsubouchi et al. (2012) demonstrate large variations of transport from the mean over time. These factors, especially the large variability, make it unclear that it is the PV transport, or in fact any properties of the gateway fluxes, that determines the cyclonic nature of the AWL. Hence, the deep water circulation in the Arctic Ocean is may be determined by internal processes, which are poorly understood, especially in an Ocean with such sparse observations.

A likely candidate for generating a cyclonic circulation is geostrophic turbulence. A number of studies have demonstrated how, in an eddying system, sloping topography can generate along-topography flows (Bretherton and Haidvogel (1976), Rhines and Young (1982), Treguier (1989), Salmon (1998), Adcock and Marshall (2000), Nøst et al. (2008)). Hence, in the absence of stronger forcing, this effect is likely to become the dominant feature. An obvious question that then comes to mind is how turbulent is the Arctic Ocean? Over recent years a large amount of effort has been made to observe and catalogue eddies in the Arctic (Zhao et al. (2014)) and has demonstrated their prevalence in the Arctic Ocean. Whilst these studies have frequently been focused on the halocline and the surface dynamics there is good reason to believe that eddies also penetrate deep into the Arctic (Figure 1.1.5, Woodgate et al. (2001)).

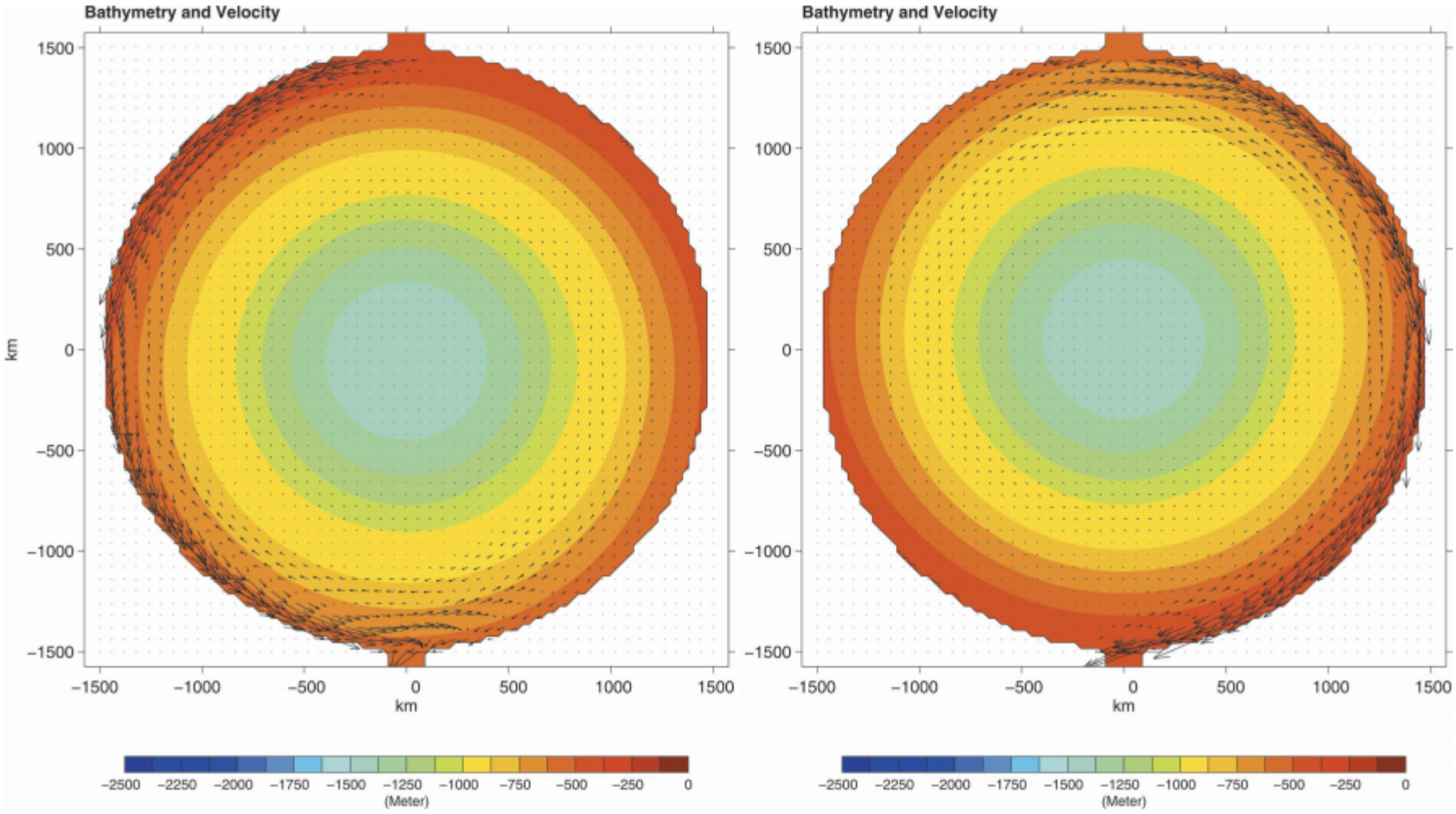


Figure 1.1.3: The circulation of two simple barotropic models. The background colour is the model bathymetry. The left plot has a net influx of PV (the inflow is shallower than the outflow) and a cyclonic circulation whilst the right plot has net outflux of PV and an anti-cyclonic circulation. Reproduced from Yang (2005).

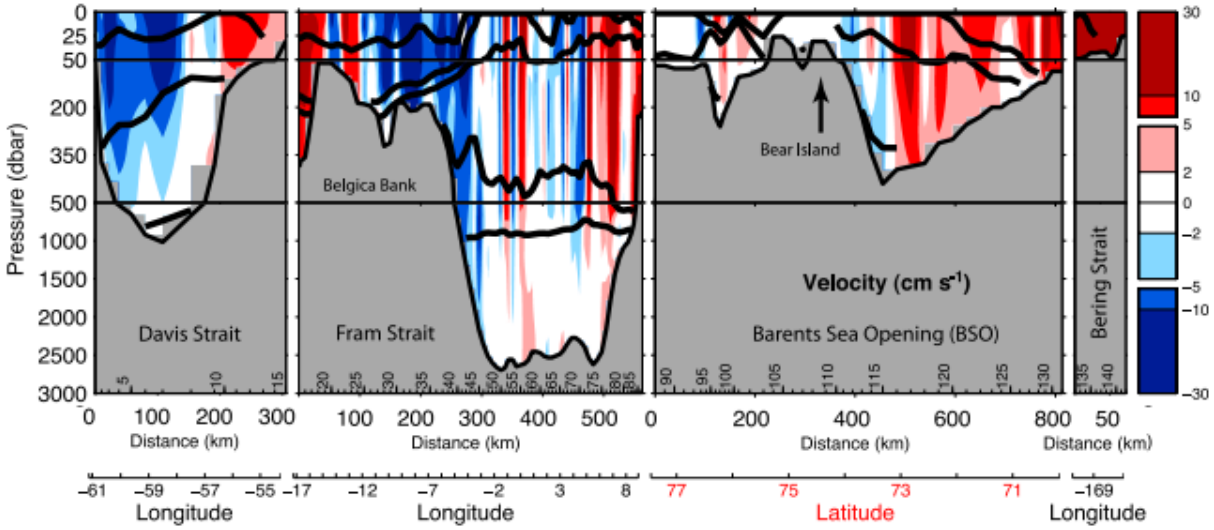


Figure 1.1.4: Velocity sections ($\mathrm{cm\,s^{-1}}$) from Arctic gateway mooring arrays. These demonstrate the pathways through the gateways, from which transport in to the Arctic can be calculated. Bold black lines show certain isopycnals, and the red (blue) colours show inflow into (outflow from) the Arctic. Reproduced from Tsubouchi et al. (2012).

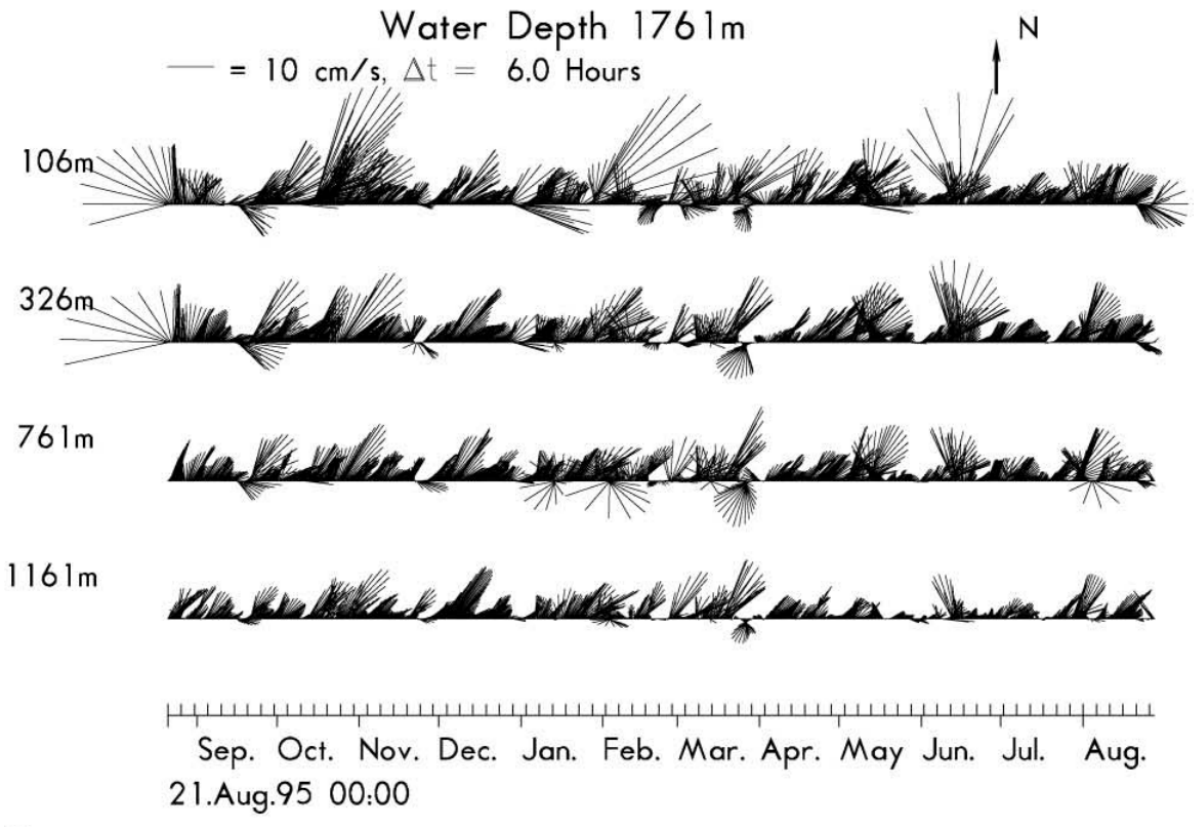


Figure 1.1.5: A stick-plot showing the velocity vectors at a year-long mooring at 78°30.8′ N, 133°57.7′ E, west of the Lomonosov Ridge for four depths. The plot shows a huge amount of variability over time, with many features being persistent throughout the water column. Adapted from Woodgate et al. (2001).

1.2 Entropy Maximisation

Holloway (1987) argues, using statistical mechanics theory, that in a barotropic quasi-geostrophic flow with variable topography eddies can be represented as a mechanical force made up of two terms. The precise details of these terms are beyond the scope of this thesis; however, the first term has the characteristics of a drag force, whilst the second term has little dependence on the direction of flow and can often represent an acceleration of the flow - this is known as the "Neptune Effect". However, little more information on the effect of eddies on the circulation can be extracted from this approach without making further assumptions.

The corner stone in the development of Neptune Effect parameterisation is the assumption that eddies act to maximise statistical entropy. Holloway (1992) uses this assumption to develop a parameterisation that captures the effect of the fluid trying to rearrange itself into a maximum entropic state. This state can be derived by applying variational calculus to the total entropy of the system of interest, whilst constraining the total energy and enstrophy. In the hope of developing a parameterisation that can be applied in general, Holloway (1992) uses a barotropic quasi-geostrophic flow in a re-entrant channel with rough topographic and a beta-plane. The resultant state of maximum entropy satisfies the equation

$$\left(\frac{\alpha_1}{\alpha_2} - \nabla^2\right) \langle\phi\rangle = h \tag{1.2.1}$$

where $\langle\phi\rangle$ is the expected stream-function of the flow, h represents the 'roughness' of the topography defined by $H = H_0\left(1 - \frac{h+\beta y}{f_0}\right)$, where H is the ocean depth, H_0 is some typical reference depth and $f_0 + \beta y$ is the linear approximation to the Coriolis Parameter, and α_1/α_2 is a quantity which represents the ratio of sensitivities to the total energy and enstrophy in the system and has dimensions which are the inverse square of length. Finally by assuming that, at the length-scales of interest, the Laplacian is small in comparison to

$$\frac{\alpha_1}{\alpha_2} = \frac{1}{\lambda^2},$$

we have that the state of maximum entropy has a flow given by

$$\boldsymbol{u}^* = \boldsymbol{k} \times \boldsymbol{\nabla}\phi^* = -\frac{\lambda^2}{H_0}\boldsymbol{\nabla} \times (fH\boldsymbol{k}) \tag{1.2.2}$$

where $\boldsymbol{k}$ is the vertical unit vector. So finally, to implement the Neptune Effect, substitute $\boldsymbol{u}$ with $\boldsymbol{u} - \boldsymbol{u}^*$ in the damping term, for example in the viscous acceleration, hence forcing the fluid to tend towards the state of maximum entropy rather than rest. A method of implementing the Neptune Effect in a rotating, hydrostatic fluid using the viscosity term could be

$$\frac{D\boldsymbol{u}}{Dt} + f\boldsymbol{k} \times \boldsymbol{u} + \frac{1}{\rho_0}\boldsymbol{\nabla}p = \mu\nabla^2\left(\boldsymbol{u} + \frac{\lambda^2}{H_0}\boldsymbol{\nabla} \times fH\boldsymbol{k}H\right) \tag{1.2.3}$$

where $\frac{D}{Dt}$ is the advective derivative, $\frac{1}{\rho_0}\boldsymbol{\nabla}p$ is the pressure gradient and μ is the kinematic viscosity.

A number of criticisms can be made about the implementation of this parameterisation. The main problem is that there are two variables which are only ever loosely defined, if at all. The first is λ, which is emerges from the energy and enstrophy of the system when applying calculus of variations; however, this only constrains its choice to being O(10 km) and is often chosen to be the Rossby radius of deformation, which implies $\lambda \to \infty$ as $\boldsymbol{f} \to 0$ a situation where the validity of the Neptune Effect is likely to already break down due to the quasi-geostrophic nature of the assumption made. The second unknown is the size of the coefficient of the damping term, e.g. the kinematic viscosity coefficient, which plays the role of determining the time-scale of relaxation back to the maximum entropic state. Combined with the possible choices for the type of damping that could be used, e.g. linear friction, viscosity or biharmonic diffusion, the Neptune becomes a highly ad-hoc parameterisation.

However, the main criticism is that a stationary, unforced ocean will be "spun up" by the Neptune Effect into a non-zero equilibrium. This is because the parameterisation is not respectful of the amount of available energy in the system to generate a non-mean flow. In the physical ocean, this energy is converted from eddy energy into mean energy

to drive an along-topography flow and hence likewise an eddy parameterisation must also do this in a controlled fashion. Since the advent of the Neptune parameterisation there have been other attempts to construct an eddy parameterisation using the idea of entropy maximisation, such as Maximum Entropy Production (Kazantsev et al. (1998) and Polyakov (2001)). However, whilst they have attempted to better constrain the introduction of energy none have done it in a widely applicable or entirely physically justified manner.

1.3 Numerical Models of Arctic

It was discussed in Section 1.1 that to understand the circulation of the Arctic Ocean it is necessary to use General Circulation Models (GCMs). However, due to poorly resolved processes or missing key physics, the GCMs available show significant variability between models and frequently display behaviour not depicted in observations. A detailed comparison of the major Global Climate Models applied to the Arctic Ocean is being carried out by the Arctic Ocean Model Inter–comparison Project (AOMIP) (see Proshutinsky et al. (2008) and Proshutinsky et al. (2011)). In this section we will specifically discuss the skill of these models in reflecting the Arctic circulation and specifically the difficulty these models have in replicating the perceived flow in the Atlantic Water Layer.

As mentioned in the previous section, the circulation in the freshwater layer is strongly governed by effects of surface forcing. To this extent, providing the various models being compared are given the same forcing, or equivalent depending on how the model is structured, then the resulting circulations are in good agreement (Proshutinsky et al. (2005)). They have been shown to have a good skill in simulating certain regimes which have been observed. However, despite good agreement of the general circulation inside the basin, there is still some variation between the climate models. The first is how the Pacific Water entering via Bering Strait is advected through the basin within the freshwater layer. The models, despite showing the same regime for the freshwater layer demonstrate different distributions of the Pacific Water when represented as a passive tracer added in Bering

Strait (Proshutinsky et al. (2011)). However, it is difficult to determine the legitimacy of the models due to limited observations and without an easy way of determining which water originates from the Pacific in the physical ocean. The most successful attempts at determining the distribution of Pacific Water have been done using tracers from other sources, such as radioactive tracers from the Atlantic and determining where they are being blocked by Pacific water such as in Karcher et al. (2004). More crucially models struggle to coherently and accurately represent mechanisms for the release of freshwater from the Arctic Ocean. This is most likely due to poor representation of the Arctic gateways specifically in the Canadian Archipelago, where many of the straits and channels are much narrower than can be comfortably resolved. However, whilst these discrepancies are important, they are not the main focus here due to the overall competence of climate models to represent the freshwater layer in the Arctic. The more distressing problem is their ability to represent the AWL.

Observations suggest that the AWL circulates counter clockwise around the Arctic basins at a depth of 200 to 800m (Figure 1.1.2). However, many attempts over the past twenty years to model the Atlantic Water Layer have resulted in confusing predictions where the circulation seemingly randomly organises into circulations that are cyclonic or anti-cyclonic with almost identical frequency. To attempt to diagnose the skill of a model to produce cyclonic boundary currents, Holloway et al. (2007) introduces the concept of "topostrophy", defined as $\tau = (f\boldsymbol{k}\wedge\boldsymbol{u})\cdot\boldsymbol{\nabla}H$, where $\boldsymbol{f}$ is the Coriolis force, $\boldsymbol{u}$ is velocity and H is the total depth. This so called topostrophy is a measure the strength of along slope flows and gives positive values for currents that flow with the up-slope to their right (e.g. for cyclonic rim currents) and negative values for the opposite. When calculated for the major AOMIP models, most show variable and ambiguous values for τ, whereas models that employ the "Neptune Effect" parameterisation, mentioned in Section 1.2, show a persistent and positive value for τ (Proshutinsky et al. (2011)). Thought this is most likely due to the nature of the parameterisation than there being any better representation of the underlying physics. Holloway and Wang (2009) examine simultaneous simulations using

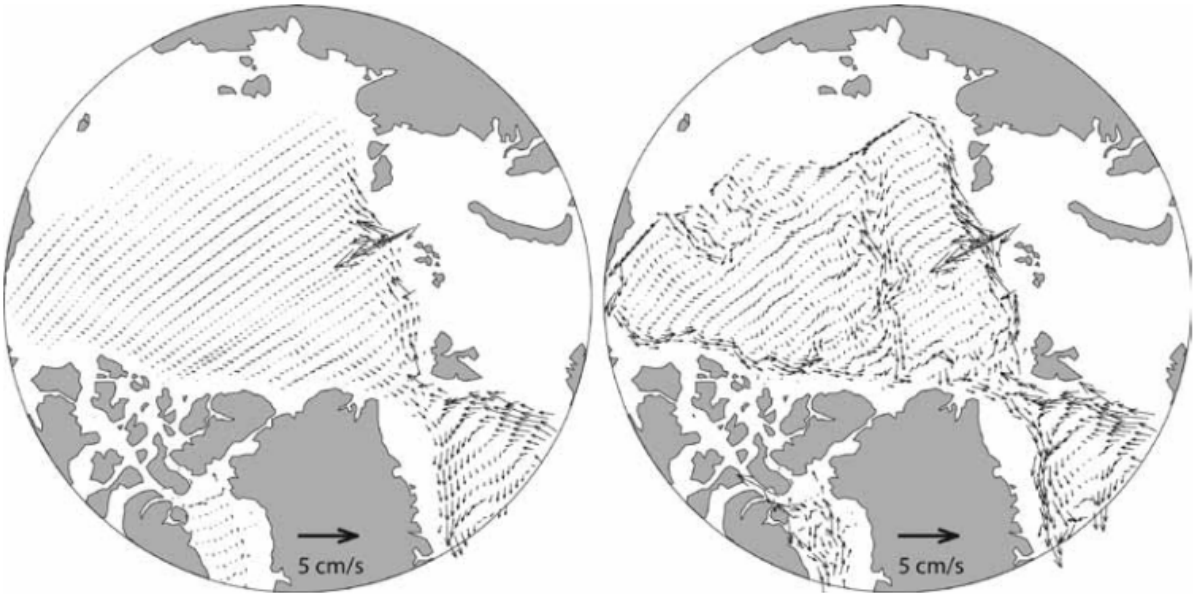


Figure 1.3.1: Left: The velocity field of the Arctic Ocean at 551m depth as simulated by the Nucleus for European Modelling of the Ocean (NEMO). Right: The velocity field at the same depth after NEMO was modified to include the Neptune Effect. The right panel clearly gives a better representation of the topographically aligned currents observed in the Arctic Ocean. Holloway and Wang (2009)

the NEMO model run with and without the "Neptune Effect" and show that the addition of this particular parameterisation is the likely cause of this tendency (Figure 1.3.1).

1.4 The Future of Modelling the Arctic Ocean and the AWL

In this chapter, we have discussed how the Arctic Ocean plays a crucial part in the climate system. The ice caps provide freshwater and cooling the Atlantic Waters as well as contributing in a major way to the planetary albedo. An understanding of how the Arctic will behave in the future is critical to our picture of the climate. A key player in this is the AWL; however, measurements in the Arctic are difficult and scarce, whilst the AOMIP has demonstrated that GCMs are woefully inadequate for predicting an accurate circulation of the AWL. The evidence of this failing seems to suggest that this is because, on climate time-scales, a GCM can at best be eddy-permitting and hence lack

the geostrophic turbulence that appears to be critical for setting the cyclonic circulation in the AWL.

As will be discussed in Chapter 2, the eddy parameterisations used in modern GCMs, namely Gent and McWilliams parameterisation (GM), are too dissipative and fail to express the driving nature of eddy-topography interactions. The models that are more successful either better resolve the eddy fields or apply a corrective force, such as the "Neptune Effect", in such a manner that does not respect the conserved properties of the system. It is therefore critical to physically understand how the mesoscale processes manifest their effect in the larger scale and hence develop a more accurate parameterisation of eddies that are physical consistent in terms of respecting the conservation of energy whilst being able to represent the effect of eddy-mean flow interactions observed over topographic slopes.

In Chapter 2 we will discuss the development of a description of these eddy-mean interactions, namely the Eliassen-Palm flux tensor, and how this tensor exhibits certain mathematical properties that should allow us to develop a physically consistent parameterisation of these eddy stresses. In Chapter 3 we develop an idealised model in which these properties can be tested, whilst the results of those experiments are presented in Chapter 4. The progress made in this thesis will then be summarised in Chapter 5 along with a roadmap of potential future work that should be carried out in order to fully develop a consistent eddy parameterisation.

Chapter 2

Development of Eddy-Mean Flow Interaction Theory

Whilst observations play a vital role in understanding the Arctic Ocean and its role in the global ocean, progress is limited by the sparsely available observations that only usefully reach back a handful of decades into the past. To be able to test possible scenarios and make future predictions it is vital that we have reliable simulations of the Arctic Ocean (Proshutinsky et al. (2008)); however, due to limitations in modern computing power and poor understanding of the unresolved processes in the ocean this is, more often than not, far from reality. Due to these computational limits a practical GCM is limited to a resolution of the order of tens of kilometres. This means that with a resolution cut off at around 10 km at higher latitudes, GCMs are unable to fully resolve a large portion of the mesoscale turbulence that is observed in the physical ocean. By attempting to understand the physics behind these unresolved processes and developing parameterisations that mimic their effect on the resolved ocean the value of computational models can be improved without dramatically increasing the computing power required.

The turbulent, chaotic nature of the ocean is caused by the non-linearity of its governing equations. Because of this, the discretisation of the equations generates cross-

correlation, or eddy, terms when applying the averaging operator,

$$\overline{\phi\psi} = \overline{\phi}\,\overline{\psi} + \overline{\phi'\psi'}, \tag{2.0.1}$$

where the $\overline{\phi}$ is the average of the variable ϕ, used in the discretisation and satisfying the expected properties of an averaging operator, and the prime denotes the residual, $\phi' = \phi - \overline{\phi}$. The operator could be an averaging over space, time, a large ensemble or a combination of these. The discretised system has no knowledge of the residual terms and hence the contributions to the full system by these eddy terms are ignored in the discretised system. It is, therefore, this "sub-grid scale process" that is missing from the model dynamics and so it is common practise to try and 'close' the system by including a parameterisation of the eddy term in place of the term itself, which is usually dependent on the averaged variables and some physical assumptions.

2.1 Gent and Mcwilliams (1990)

The earliest ocean models (Bryan (1969)) had depth-coordinates in the vertical with simple horizontal and vertical Laplacian diffusion to act as the closure. Whether these terms are interpreted as a parameterisation for the effects of unresolved turbulence or simply as a numerical tool to avoid noise at the grid scale, the viscosity parameter is tuned such that the turbulent energy cascade is dissipated at the grid scale whilst still allowing as active dynamics as possible. Assuming modern day computing power, this implies a horizontal viscosity of around $10^2 - 10^4 \mathrm{m}^2\mathrm{s}^{-1}$, a viscosity much greater than that of the physical ocean. This is usually represented by a horizontal diffusion, hence a second problem is that such a strong horizontal diffusion diffuses or mixes tracers excessively.

It has long been understood that tracers mix much more along isopycnal surfaces than across them (Iselin (1939), Montgomery (1940)), a property which helps maintain the definition of distinct water masses in the global ocean (for example, Emery and Meincke (1986)). In contrast, excessive horizontal diffusion of tracers in ocean models

leads to water mass properties being eroded and spurious sources and sinks of heat in the ocean interior, or the "Veronis Effect" (Veronis (1975)). Hence, a more physically appropriate eddy parameterisation is needed; and so, in a way that seems obvious today, it was found that eddies need to be parameterised in such a way that their effect is along isopycnals. The effort to do this in the 80's and early 90's gave birth to what is known as the GM parameterisation, first introduced in Gent and Mcwilliams (1990).

So what is the GM parameterisation? Since mixing occurs primarily along isopycnal surfaces it makes sense to have this discussion in isopycnal coordinates, that is in the coordinate space (x, y, ρ), where density, ρ, has replaced depth, z, as the vertical coordinate. Whilst the rigorous exploration of this coordinate system will be discussed in detail in Section 2.4, for our current purposes it is enough to say that this coordinate system produces an equation for isopycnal "thickness",

$$\frac{\partial z_\rho}{\partial t} + \boldsymbol{\nabla}_\rho \cdot (z_\rho \boldsymbol{u}) = 0, \tag{2.1.1}$$

where $z_\rho = \partial z / \partial \rho$ is the negative of what is known as the isopycnal thickness, $\boldsymbol{u}$ is the horizontal fluid velocity and $\boldsymbol{\nabla}_\rho$ is the horizontal divergence operator at constant density ρ, rather than constant buoyancy, b, as presented in Young (2012). Since it is non-linear, when this equation is discretised it produces an eddy covariance term as demonstrated by Equation (2.0.1); the averaged equation can be written as

$$\frac{\partial \overline{z_\rho}}{\partial t} + \boldsymbol{\nabla}_\rho \cdot (\overline{z_\rho}\, \overline{\boldsymbol{u}}) = -\boldsymbol{\nabla}_\rho \cdot \left(\overline{z_\rho{}' \boldsymbol{u}'}\right). \tag{2.1.2}$$

The eddies should therefore be parameterised by some representation of $\overline{z_\rho{}' \boldsymbol{u}'}$, say $\boldsymbol{F}$, so that the thickness equation becomes

$$\frac{\partial z_\rho}{\partial t} + \boldsymbol{\nabla}_\rho \cdot (z_\rho \boldsymbol{u}) + \boldsymbol{\nabla}_\rho \cdot \boldsymbol{F} = 0, \tag{2.1.3}$$

where the bars have been dropped for convenience. It can also be noted that by defining

$\hat{\boldsymbol{u}} = \boldsymbol{F}/z_\rho$ the above equation can be interpreted as the isopycnal thickness being advected by the mean horizontal velocity, $\boldsymbol{u}$, plus an eddy induced 'bolus velocity', $\hat{\boldsymbol{u}}$ (Gent et al. (1995)). Gent and Mcwilliams (1990) proposes that eddies act to flatten each isopycnal via baroclinic instability, achieved by setting

$$\boldsymbol{F} = -\frac{\partial}{\partial \rho}\left(\kappa \boldsymbol{\nabla}_\rho z\right), \tag{2.1.4}$$

where κ can be a spatially and temporally varying "eddy diffusivity". Combining this with Equation (2.1.3) we have

$$\frac{\partial z_\rho}{\partial t} + \boldsymbol{\nabla}_\rho \cdot \left(z_\rho \boldsymbol{u}\right) = \boldsymbol{\nabla}_\rho \cdot \frac{\partial}{\partial \rho}\left(\kappa \boldsymbol{\nabla}_\rho z\right). \tag{2.1.5}$$

By Gent et al. (1995), we can similarly, for a tracer, say τ, write an equation describing its transport,

$$\frac{\partial \tau}{\partial t} + \boldsymbol{u} \cdot \boldsymbol{\nabla}_\rho \tau = \boldsymbol{\nabla}_\rho \tau \cdot \frac{\partial}{\partial \rho}\left(\kappa \boldsymbol{\nabla}_\rho z\right)/z_\rho. \tag{2.1.6}$$

Here, it is assumed the thickness and tracer eddy terms are uncorrelated and so the term is dropped. It is also assumed that eddies mix tracers along isopycnals and not across them and so the correlation between the eddy thickness and velocity is parameterised as Fickian diffusion but is ignored in Equation (2.1.6) for simplicity.

There are a few properties of this parameterisation that can be noted to help describe the effect of its implementation in ocean models. Firstly, by writing $\boldsymbol{u}^\star = \boldsymbol{u} - \frac{\partial}{\partial \rho}\left(\kappa \boldsymbol{\nabla}_\rho z\right)/z_\rho$ we simply have that

$$\frac{\partial z_\rho}{\partial t} + \boldsymbol{\nabla}_\rho \cdot \left(z_\rho \boldsymbol{u}^\star\right) = 0 \tag{2.1.7}$$

and

$$\frac{\partial \tau}{\partial t} + \boldsymbol{u}^\star \cdot \boldsymbol{\nabla}_\rho \tau = 0 \tag{2.1.8}$$

indicating that the tracer τ is effectively advected by a transport velocity, $\boldsymbol{u}^\star$. Secondly,

an important question is, how does GM change the energy of the system? We gain the potential energy equation by multiplying Equation (2.1.5) by the Montgomery potential, ϕ, which is defined as

$$\phi = (p - g\rho z)/\rho_0, \qquad \phi_\rho = -gz/\rho_0,$$

where p is the pressure, g is the gravity and ρ_0 is a reference density. The addition them in the potential energy equation due to the parameterisation in Equation (2.1.5) can be written as

$$\phi \boldsymbol{\nabla}_\rho \cdot \frac{\partial}{\partial \rho}\left(\kappa \boldsymbol{\nabla}_\rho z\right) = \boldsymbol{\nabla}_\rho \cdot \frac{\partial}{\partial \rho}\left(\phi \kappa \boldsymbol{\nabla}_\rho z\right) - \frac{\partial}{\partial \rho}\left(\kappa \boldsymbol{\nabla}_\rho \phi \cdot \boldsymbol{\nabla}_\rho z\right) - \left(\kappa g \boldsymbol{\nabla}_\rho z \cdot \boldsymbol{\nabla}_\rho z\right)/\rho_0, \quad (2.1.9)$$

as demonstrated in Gent (2011). Integrating over an entire domain eliminates the first two terms leaving the final term as a positive definite sink of energy. These two properties characterise GM; the parameterisation acts along isopycnal surfaces to flatten isopycnal surfaces whilst dissipating potential energy.

The dissipative nature of GM is both a strength and a weakness. GM is incapable of introducing spurious energy, which allows it to be very robust and stable parameterisation, meaning it can be easily implemented into a GCM. However, it is also understood that ocean turbulence is not purely dissipative. Adcock and Marshall (2000) concisely demonstrate that in an idealised model, with no external forcing other than an initial eddy field, a persistent mean flow will develop along topography and the isopycnals will dome above the topography. Nøst et al. (2008) show that these flows develop asymmetrically, such that the flow is predominantly cyclonic above the sloped sides of a basin or anticyclonic over a sea-mount. For this to occur when the eddy field is unresolved there must be an injection of energy into the system representing the inverse cascade of energy from the eddy scales to the large scale. However, this is prohibited by the purely dissipative GM and so a different parameterisation is required to mimic this effect.

2.2 PV Closure

To proceed one might wonder what makes the continuity equation so special? In truth there are a number of non-linearities that crop up when examining the full equations of motion. Take, for example, the vertical component of the absolute vorticity equation, which can be written in the same flux form as the continuity equation, i.e.

$$\frac{\partial \omega}{\partial t} + \boldsymbol{\nabla} \cdot (\omega \boldsymbol{u}) = (\boldsymbol{\omega} \cdot \nabla)\, w + F, \tag{2.2.1}$$

where $\omega = f + \xi$ is the vertical component of the absolute vorticity, $\boldsymbol{\omega}$, $\xi = \boldsymbol{k} \cdot (\boldsymbol{\nabla} \wedge \boldsymbol{u})$ is the relative vorticity, $(\boldsymbol{\omega} \cdot \boldsymbol{\nabla})\, w$ is vortex tilting, w the vertical velocity and $F = \boldsymbol{k} \cdot (\boldsymbol{\nabla} \wedge \boldsymbol{F})$ is the diabatic forcing term with $\boldsymbol{F}$ inherited from the forcing in the momentum equations. By applying an average operator to Equation (2.2.1), and taking $F = 0$ and $(\boldsymbol{\omega} \cdot \nabla)\, w = 0$ for simplicity, we have the same averaged equation as Equation (2.1.2) but for the mean absolute vorticity, $\overline{\omega}$,

$$\frac{\partial \overline{\omega}}{\partial t} + \boldsymbol{\nabla} \cdot (\overline{\omega}\, \overline{\boldsymbol{u}}) = -\boldsymbol{\nabla} \cdot \left(\overline{\omega' \boldsymbol{u}'} \right), \tag{2.2.2}$$

which to close in a numerical model requires the right hand side, $-\boldsymbol{\nabla} \cdot \left(\overline{\omega' \boldsymbol{u}'} \right)$, to be parameterised. Greatbatch (1998) makes the observation here that the mechanism this equation is describing is much clearer if we note the following; if we take $\overline{q}$ to be the thickness weighted mean of q, i.e. $\overline{q} = \overline{z_\rho q} / \overline{z}_\rho$, then $\overline{\omega} = \overline{q}\, \overline{z}_\rho$ and $\omega' = \overline{z}_\rho q' + \overline{q} z'_\rho$. By combining this with Equation (2.1.2) we gain a conservative equation for PV,

$$\frac{\partial \left(\overline{z}_\rho \overline{q} \right)}{\partial t} + \boldsymbol{\nabla} \cdot \left(\overline{z}_\rho\, \overline{q}\, \overline{\boldsymbol{u}} + \overline{q} \overline{z'_\rho \boldsymbol{u}'} \right) = -\boldsymbol{\nabla} \cdot \left(\overline{z}_\rho\, \overline{q' \boldsymbol{u}'} \right). \tag{2.2.3}$$

This is the form of PV conservation which, with the inclusion of $\overline{F}$, leads to the impermeability theorems of Haynes and McIntyre (1987) and Haynes and McIntyre (1990).

Now, by making the same assumption that was made for isopycnal thickness in GM for PV, that ocean eddies mix PV along isopycnals in the down-gradient direction, Equa-

tion (2.2.3) becomes

$$\frac{\partial\left(\overline{z}_\rho\overline{q}\right)}{\partial t}+\boldsymbol{\nabla}\cdot\left(\overline{z}_\rho\,\overline{q}\,\overline{\boldsymbol{u}}+\overline{q}\overline{z'_\rho\boldsymbol{u}'}\right)=\boldsymbol{\nabla}\cdot\left(\kappa\overline{z}_\rho\,\boldsymbol{\nabla}\overline{q}\right), \tag{2.2.4}$$

where, as demonstrated in Gent and Mcwilliams (1990), the small slope approximation has been used. By using Equations (2.1.2) and (2.2.4) we have exactly the equation for an arbitrary tracer given in Equation (6) of Gent et al. (1995),

$$\frac{D^\star\overline{q}}{Dt}\equiv\frac{\partial\overline{q}}{\partial t}+\boldsymbol{u}^\star\cdot\boldsymbol{\nabla}\overline{q}=\boldsymbol{\nabla}\cdot\left(\kappa\overline{z}_\rho\boldsymbol{\nabla}\overline{q}\right)/\overline{z}_\rho, \tag{2.2.5}$$

applied to the mean PV, which is advected by the transport velocity $\boldsymbol{u}^\star$ and diffused along isopycnal surfaces. This is the PV closure as first proposed by Greatbatch (1998).

Equation (2.2.5) represents the interaction of eddies as the down-gradient diffusion of PV, and hence suggests that eddies act to homogenise PV. Since PV can be approximately written as $q=f/\sigma$ for small relative vorticity, the parametrisation acts to homogenise isopycnal thickness. In the case where there is no topography this is identical to the flattening of isopycnals. However, in the presence of topography, in trying to homogenise isopycnal thickness the isopycnals end up mimicking the shape of the topography. Unfortunately, allowing this to happen freely clearly violates energy conservation, as demonstrated schematically in Figure 2.2.1. In reality, the ocean attempts to homogenise PV but only if there is energy available to do so. The result is the slight "cold doming" above topography as observed in Adcock and Marshall (2000).

However, whilst, unlike GM, the down-gradient dissipation of PV is capable of introducing spurious energy, it does dissipate another important quantity: the "Potential Enstrophy". By multiplying through by $\overline{z}_\rho\overline{q}$, Equation (2.2.5) becomes

$$\frac{\partial}{\partial t}\left(\frac{1}{2}z_\rho q^2\right)+\boldsymbol{\nabla}\cdot\left(z_\rho q\boldsymbol{u}^\star-\kappa z_\rho q\boldsymbol{\nabla}q\right)=-\kappa z_\rho\boldsymbol{\nabla}q\cdot\boldsymbol{\nabla}q \tag{2.2.6}$$

where the bars have been dropped for convenience. Integrating over the entire domain

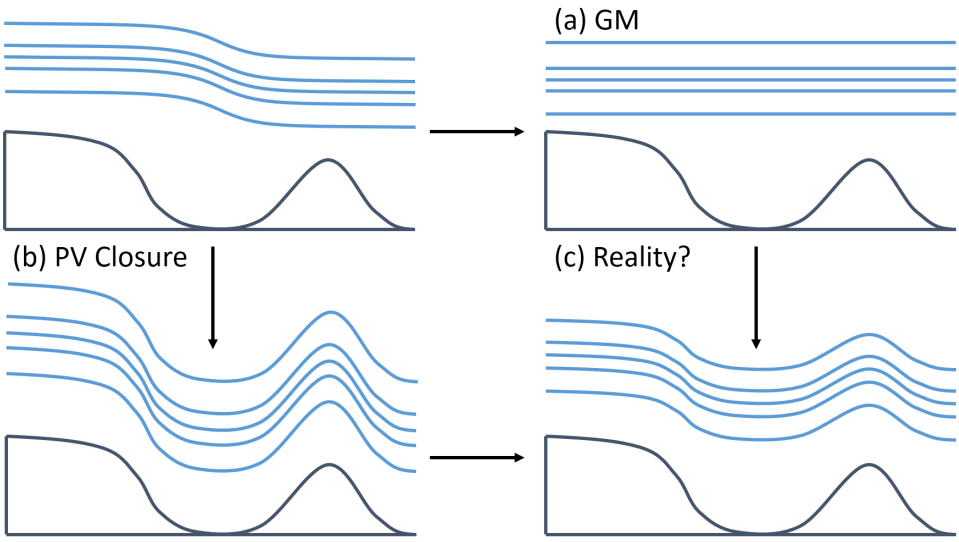


Figure 2.2.1: The effect of different eddy parameterisation schemes on a baroclinic front in the presence of topography. The light blue lines are isopycnals. (a) Gent and McWilliams extracts potential energy and flattens the isopycnals. (b) The PV closure homogenises the PV within isopycnal layers. This causes the isopycnals to rise excessively over the topography, violating energy conservation. (c) In reality there is some doming of the isopycnals over the topography, but the potential vorticity is not made uniform.

eliminates the divergent term leaving just a positive definite dissipation on the right hand side. Hence, in the same way that GM dissipates potential energy, this PV closure dissipates potential enstrophy. This suggests the tantalising possibility that eddy-mean interactions are GM-like when there is limited eddy energy available to transform into mean energy but diffuse PV when limited by available eddy potential enstrophy to transform into mean potential enstrophy.

2.3 Eliassen-Palm Flux Tensor

It is clear from these attempts to parameterise the eddy-mean interaction that the only way to proceed is by being able to take into account all eddy correlations that appear in the state equations. Residual-mean theory allows the directionally averaged primitive equations to be written such that only diabatic buoyancy fluxes appear in the thermodynamic equation whilst the eddy-mean interactions in the momentum equations appear as the divergence of Eliassen-Palm Flux vectors (Eliassen and Palm (1961), Andrews and

McIntyre (1976)). The Eliassen-Palm framework provides a useful tool for describing eddy fluxes by combining the eddy momentum and eddy heat fluxes into a single structure with which there direction, magnitude and relative importance can be determined.

The Eliassen-Palm flux vectors also appear in other descriptions of ocean dynamics. In the averaged hydrostatic primitive equations, the eddy-mean interactions appear as two Eliassen-Palm flux vectors, one for each component of the horizontal velocity (Young (2012)). Similarly, a rank-two Eliassen-Palm flux tensor can be derived for the statistically steady quasi-geostrophic equations (Cronin (1996)). Maddison and Marshall (2013) demonstrate the geometric relationship between Eliassen-Palm fluxes and how they collapse into a single coordinate invariant tensor in the quasi-geostrophic limit up to a gauge transformation. In this limit the Eliassen-Palm flux tensor can be written as

$$\boldsymbol{E} = \begin{pmatrix} -M+P & N & 0 \\ N & M+P & 0 \\ -S & R & 0 \end{pmatrix} \tag{2.3.1}$$

(Plumb (1986)), where

$$\begin{aligned} M &= \tfrac{\overline{v'^2-u'^2}}{2}, \quad N = \overline{u'v'}, \quad P = \tfrac{\overline{b'^2}}{2\mathcal{N}_0^2}, \\ R &= \tfrac{f_0}{\mathcal{N}_0^2}\overline{b'u'}, \qquad \text{and} \qquad S = \tfrac{f_0}{\mathcal{N}_0^2}\overline{b'v'}; \end{aligned} \tag{2.3.2}$$

and where b is buoyancy, f_0 is zeroth order approximation of the Coriolis parameter and

$$\mathcal{N}_0 = \sqrt{-\frac{g}{\rho_0}\frac{d\rho}{dz}}$$

is the buoyancy frequency, where g is gravity, ρ density and ρ_0 is a reference density. Marshall et al. (2012) demonstrates that by taking a weighted Frobenius norm on $\boldsymbol{E}$ and applying the Cauchy-Schwarz inequality a handful of times, the tensor is bounded by the eddy energy,

$$\|\boldsymbol{E}\| \leq (K+P) \equiv E, \tag{2.3.3}$$

where $K = \overline{u'^2 + v'^2}/2$ is the eddy kinetic energy. Without any loss of generality, this bound allows us to rewrite the components of the tensor in the form

$$\begin{aligned} M = -\gamma_m E \cos 2\phi_m \cos^2\lambda, \quad & N = \gamma_m E \sin 2\phi_m \cos^2\lambda, \\ P = E \sin^2\lambda, \quad & K = E\cos^2\lambda, \\ R = \gamma_b \tfrac{f_0}{\mathcal{N}_0^2} E \cos\phi_b \sin 2\lambda, \quad & S = \gamma_b \tfrac{f_0}{\mathcal{N}_0^2} E \sin\phi_b \sin 2\lambda. \end{aligned} \tag{2.3.4}$$

Here we have introduced two eddy anisotropies, $0 \leq \gamma_m, \gamma_b \leq 1$, two eddy flux angles $0 \leq \phi_m, \phi_b \leq \pi$ and an eddy energy partition angle, $0 \leq \lambda \leq \pi/2$. Now the Eliassen-Palm flux tensor is written in terms of five non-dimensional, bounded parameters and E, the eddy energy. See Marshall et al. (2012) for further details.

2.4 Thickness Weighted Averaging

Returning to the Arctic Ocean as discussed in Section 1.1, the ocean is a relatively quiescent and highly stratified. With that in mind, an appropriate framework for describing the dynamics of the Arctic is the hydrostatic primitive equations in isopycnal coordinates. Young (2012) carefully constructs these from Cartesian coordinate hydrostatic primitive equations,

$$\frac{Du}{Dt} - fv + p_x = \mathcal{X}, \tag{2.4.1a}$$

$$\frac{Dv}{Dt} + fu + p_y = \mathcal{Y}, \tag{2.4.1b}$$

$$p_z = b, \tag{2.4.1c}$$

$$u_x + v_y + w_z = 0, \tag{2.4.1d}$$

$$\frac{Db}{Dt} = \omega; \tag{2.4.1e}$$

where $b(\boldsymbol{x}, t)$ is the buoyancy, $\rho = \rho_0 (1 - g^{-1} b)$; $\mathcal{X}$, $\mathcal{Y}$ denote adiabatic processes and body forces and ω represents any diabatic forcing.

In isopycnal coordinates this becomes

$$\frac{Du}{Dt} - fv + m_x = \mathcal{X}, \tag{2.4.2a}$$

$$\frac{Dv}{Dt} + fu + m_y = \mathcal{Y}, \tag{2.4.2b}$$

$$m_b + \eta = 0, \tag{2.4.2c}$$

$$\frac{\partial \sigma}{\partial t} + (\sigma u)_x + (\sigma v)_y + (\sigma \omega)_b = 0. \tag{2.4.2d}$$

Here $z \equiv \eta(x, y, b, t)$, where the symbol η is used to distinguish it as a dependent function;

$$\frac{D}{Dt} \equiv \frac{\partial}{\partial t} + u\frac{\partial}{\partial x} + v\frac{\partial}{\partial y} + \omega\frac{\partial}{\partial b}$$

is the convective derivative in isopycnal coordinates; $m \equiv p - b\eta$ is the Montgomery potential and $\sigma \equiv \eta_b = -m_{bb}$. Compare the continuity equation, Equation (2.4.2d), with Equation (2.1.1), noting that $\sigma = \eta_b$ is equivalent to $-z_\rho$. Using Equations (2.4.2), an energy equation can also be derived,

$$\frac{\partial \sigma \frac{1}{2}\left|\boldsymbol{u}\right|^2}{\partial t} + \frac{\partial \eta^2}{\partial t} = -\boldsymbol{\nabla}_\rho \left(\sigma \frac{1}{2}\left|\boldsymbol{u}\right|^2 \boldsymbol{u} + \sigma m \boldsymbol{u} \right) - \left(\frac{\partial \eta}{\partial t} m \right)_b, \tag{2.4.3}$$

where $\mathcal{X}$, $\mathcal{Y}$ and ω have been taken to be zero for convenience and where $\frac{1}{2}\left|\boldsymbol{u}\right|^2$ is kinetic energy and η^2/σ is potential energy. Integrating over the entire domain, the right hand side vanishes.

Now, by defining a thickness weighted average, $\overline{\psi} = \langle \sigma\psi \rangle / \langle \sigma \rangle$, where $\langle \psi \rangle$ is the standard average and their residuals, $\psi' = \psi - \overline{\psi}$ and $\psi^{\#} = \psi - \langle \psi \rangle$, Young (2012) constructs the Eliassen-Palm flux vectors, $\boldsymbol{E}^u$ and $\boldsymbol{E}^v$, for these equations so that the momentum equations become

$$\frac{\mathring{D}\overline{u}}{Dt} - f\overline{v} + \langle m \rangle_x + \langle \sigma \rangle^{-1} \boldsymbol{\nabla} \cdot \boldsymbol{E}^u = \overline{\mathcal{X}}, \tag{2.4.4a}$$

$$\frac{\mathring{D}\overline{v}}{Dt} + f\overline{u} + \langle m \rangle_y + \langle \sigma \rangle^{-1} \boldsymbol{\nabla} \cdot \boldsymbol{E}^v = \overline{\mathcal{Y}}, \tag{2.4.4b}$$

where

$$\frac{\mathring{D}}{Dt} =\equiv \frac{\partial}{\partial t} + \overline{u}\frac{\partial}{\partial x} + \overline{v}\frac{\partial}{\partial y} + \overline{\omega}\frac{\partial}{\partial b}$$

is the mean convective derivative, whilst the continuity equation is just

$$\frac{\partial \langle \sigma \rangle}{\partial t} + \left(\langle \sigma \rangle \overline{u}\right)_x + \left(\langle \sigma \rangle \overline{v}\right)_y + \left(\langle \sigma \rangle \overline{\omega}\right)_b = 0. \tag{2.4.4c}$$

Here, $\boldsymbol{E}^u$ and $\boldsymbol{E}^v$ are defined as

$$\begin{aligned} \boldsymbol{E}^u &= \langle \sigma \rangle \begin{pmatrix} \overline{u'u'} \\ \overline{u'v'} \\ \overline{u'\omega'} \end{pmatrix} + \begin{pmatrix} \frac{1}{2}\left\langle \eta^{\#}\eta^{\#} \right\rangle \\ 0 \\ \left\langle \eta^{\#} m_x^{\#} \right\rangle \end{pmatrix}, \\ \boldsymbol{E}^v &= \langle \sigma \rangle \begin{pmatrix} \overline{u'v'} \\ \overline{v'v'} \\ \overline{v'\omega'} \end{pmatrix} + \begin{pmatrix} 0 \\ \frac{1}{2}\left\langle \eta^{\#}\eta^{\#} \right\rangle \\ \left\langle \eta^{\#} m_y^{\#} \right\rangle \end{pmatrix}. \end{aligned} \tag{2.4.4d}$$

Crucially, in Young (2012) the first two components of $\boldsymbol{E}^u$ and $\boldsymbol{E}^v$ are directed along the isopycnals, whilst only the third component is directed through isopycnal surfaces; hence, in the adiabatic case (i.e. when $\omega = 0$) $\langle \sigma \rangle^{-1} \left\langle \eta^{\#} m_x^{\#} \right\rangle$ and $\langle \sigma \rangle^{-1} \left\langle \eta^{\#} m_y^{\#} \right\rangle$ are precisely the "inviscid pressure drag" or "form drag" identified by Rhines and Holland (1979) and represents the transfer of momentum across isopycnal surfaces. One key feature of this formulation is that the eddy stresses are all entirely described in the momentum equations; hence one might wonder what has happened to the bolus velocity described by Gent et al. (1995)? It turns out that the thickness weighted velocity is precisely the transport velocity, since $\overline{\boldsymbol{u}} = \langle \sigma \boldsymbol{u} \rangle / \langle \sigma \rangle = \langle \boldsymbol{u} \rangle + \left\langle \sigma^{\#} \boldsymbol{u}^{\#} \right\rangle / \langle \sigma \rangle$ and $\left\langle \sigma^{\#} \boldsymbol{u}^{\#} \right\rangle / \langle \sigma \rangle$ is the bolus velocity. Hence, this implies that the equations explicitly represent the mean velocities as the transport velocities. To retrieve the bounds derived by Marshall et

al. (2012), we write $\boldsymbol{E} = (\boldsymbol{E}^u, \boldsymbol{E}^v, 0)$ and note that in the geostrophic limit $m_x \sim fv$ and $m_y \sim -fu$. Then by writing

$$\begin{aligned} M &= \tfrac{\overline{v'^2 - u'^2}}{2}, & N &= \overline{u'v'}, \\ K &= \tfrac{\overline{u'^2 + v'^2}}{2}, & P &= \left\langle \eta^{\#^2} \right\rangle / \langle \sigma \rangle, \\ R &= f \left\langle \eta^{\#} u^{\#} \right\rangle / \langle \sigma \rangle, & \text{and} \qquad S &= f \left\langle \eta^{\#} v^{\#} \right\rangle / \langle \sigma \rangle; \end{aligned} \tag{2.4.5}$$

we have (in the adiabatic case) that

$$\boldsymbol{E} = \langle \sigma \rangle \begin{pmatrix} -M + K + P & N & 0 \\ N & M + K + P & 0 \\ S & -R & 0 \end{pmatrix}. \tag{2.4.6}$$

By applying a weighted Frobenius norm, defined as the square root of a weighted sum of the squares,

$$\sqrt{\langle \sigma \rangle^2 (-M + K + P)^2 + 2 \langle \sigma \rangle^2 N^2 + \langle \sigma \rangle^2 (M + K + P)^2 + \frac{1}{f^2} S^2 + \frac{1}{f^2} R^2},$$

in a similar fashion to Marshall et al. (2012) we recover an energy bound on $\boldsymbol{E}$,

$$\|\boldsymbol{E}\| \leq 2 (K + P) \equiv 2E. \tag{2.4.7}$$

The factor of 2 difference in this bound, in comparison to Marshall et al. (2012) is due to slightly different definitions of the Frobenius norm.

Equations (2.4.4) are of the same form as Equations (2.4.2). Hence, it is possible to derive an Rossby-Ertel PV for the thickness weighted system as

$$\frac{\mathring{D}\mathring{q}}{Dt} + \langle m \rangle_x + \langle \sigma \rangle^{-1} \boldsymbol{\nabla} \cdot \mathring{\boldsymbol{F}} + \langle \sigma \rangle^{-1} \boldsymbol{\nabla} \cdot \mathring{\boldsymbol{\Gamma}} = 0, \tag{2.4.8}$$

where

$$\mathring{q} \equiv \frac{f + \overline{v}_x - \overline{u}_y}{\langle \sigma \rangle}, \tag{2.4.9}$$

is the Rossby-Ertel PV, Γ contains only the diabatic terms involving $\overline{\mathcal{X}}$, $\overline{\mathcal{Y}}$ and $\overline{\varpi}$ and

$$\mathring{\boldsymbol{F}} = \langle\sigma\rangle^{-1} \begin{pmatrix} \boldsymbol{\nabla}\cdot\boldsymbol{E}^v \\ -\boldsymbol{\nabla}\cdot\boldsymbol{E}^u \\ 0 \end{pmatrix}. \tag{2.4.10}$$

Hence, the PV fluxes can be written in terms of the momentum fluxes, whilst the momentum fluxes, $\boldsymbol{\nabla}\cdot\boldsymbol{E}^u = -\langle\sigma\rangle\,\mathring{\boldsymbol{F}}\cdot\boldsymbol{j}$ and $\boldsymbol{\nabla}\cdot\boldsymbol{E}^v = \langle\sigma\rangle\,\mathring{\boldsymbol{F}}\cdot\boldsymbol{i}$, can be written in terms of the PV fluxes. Rather than $\mathring{q}$, Greatbatch (1998) suggest the use of a thickness weighted Rossby-Ertel PV,

$$\overline{q} = \frac{\langle\sigma q\rangle}{\langle\sigma\rangle} = \frac{f + \langle v\rangle_x - \langle u\rangle_y}{\langle\sigma\rangle}, \tag{2.4.11}$$

which leads to

$$\frac{\mathring{D}\left(\overline{q}\right)}{Dt} + \langle\sigma\rangle^{-1}\boldsymbol{\nabla}\cdot\left(\langle\sigma\rangle\,\overline{q'\boldsymbol{u}'}\right) + \langle\sigma\rangle^{-1}\boldsymbol{\nabla}\cdot\boldsymbol{\Upsilon} = 0, \tag{2.4.12}$$

where, again, $\boldsymbol{\Upsilon}$ only contains diabatic terms. Compare with Equation (2.2.3), and by noting that $\langle\sigma\rangle\,\overline{\boldsymbol{u}} = \langle\sigma\rangle\,\langle\boldsymbol{u}\rangle + \left\langle\sigma^{\#}\boldsymbol{u}^{\#}\right\rangle$, we have the Greatbatch (1998) form of PV closure. Using the Cauchy-Schwarz inequality, it is easily noted that the norm of $\overline{q'\boldsymbol{u}'}$ is bounded

$$\left\|\overline{q'\boldsymbol{u}'}\right\| \leq 2\sqrt{KQ}, \tag{2.4.13}$$

recalling that $K = \frac{\overline{u'^2+v'^2}}{2}$ is the eddy kinetic energy and $Q = \frac{\overline{q'^2}}{2}$ is the eddy potential enstrophy. Providing $\mathring{q} \sim \overline{q}$, which is equivalent to the curl of the bolus velocities $\left(\left\langle\sigma^{\#}v^{\#}\right\rangle / \langle\sigma\rangle\right)_x - \left(\left\langle\sigma^{\#}u^{\#}\right\rangle / \langle\sigma\rangle\right)_y$ being small, then it can be assumed, in the adiabatic case, that $\boldsymbol{\nabla}\cdot\mathring{\boldsymbol{F}} \sim \boldsymbol{\nabla}\cdot\left(\overline{q'\boldsymbol{u}'}\right)$ and so $\mathring{\boldsymbol{F}}$, and hence $\boldsymbol{\nabla}\cdot\boldsymbol{E}$ is also bounded by $2\sqrt{KQ}$.

2.5 Summary and Hypotheses

Since the likes of Young et al. (1982), Holloway (1987) and Gent and Mcwilliams (1990), we have seen much development of how to describe the mean-eddy interaction. Attempting to parameterise this in non-eddy-resolving models has lead to continuity and PV

closure parameterisations such as Gent and Mcwilliams (1990) and Greatbatch (1998) as well maximum entropy principle parameterisations such as the "Neptune Effect" (Holloway (1992)) and Polyakov (2001) discussed in Section 1.2. However, to date these parameterisations fail woefully over topography. Either they are far to dissipative, like GM, and fail to represent the driving nature of eddies-topographic interactions, or they violate energy conservation by failing to appropriately control the energy injected into the system, as in the cases of PV closure and the "Neptune Effect". To avoid this, models attempting to use non-dissipative parameterisations often attempt to tune the parameterisation in an ad-hoc fashion to avoid spurious energy injection. However, by carefully implementing the framework put forward by Marshall et al. (2012) and generalised in Maddison and Marshall (2013), one might create a parameterisation which is inherently bounded by energy and enstrophy constraints.

The discussion in this Section has shown that the mean-eddy interactions emerge with competing GM-like and "Neptune Effect"-like natures, as in Adcock and Marshall (2000). Meanwhile it is possible to show that the Eliassen-Palm flux tensor can be bounded by eddy energy and eddy potential enstrophy (Marshall et al. (2012)). Diagnosis of the contributions to the eddy stress tensor from the eddy kinetic and potential energy, as well as the Reynolds stress angle and eddy buoyancy flux angle will allow the investigation of the following:

- The extent to which finite eddy energy inhibits the ability of eddies to generate a mean along-topography flow.

- The extent to which the topographic slope is the controlling factor for the structure of the eddy stresses in eddy-mean flow interactions over variable bottom topography.

- The extent to which the two definitions for the mean PV are quantifiably different, that is $\mathring{q}$ the PV derived from the mean equations and $\overline{q}$ the thickness weighted mean of the full PV.

- Hence, the extent to which the enstrophy bound holds for $\mathring{F}$ and hence, the extent

to which the eddy stresses are inhibited by the available eddy potential enstrophy.

The investigation of these hypotheses allows for a deeper understanding of how to develop an eddy parameterisation that is not purely dissipative but instead exhibits more realistic properties whilst still remaining physically consistent.

Chapter 3

Development of Stacked Shallow Water Equations

With the hope of taking advantage of the invariance demonstrated by Maddison and Marshall (2013), we need to be able to diagnose the eddy terms in a controlled and repeatable environment. Hence, we turn our attention to idealised models as a representation of ocean dynamics. This has an advantage over using observational data as well as output from GCMs for a number of reasons.

- The main limitation is that for this analysis to work, it must be possible to define an averaging operator that splits the eddy components of the system from the mean components; the most effective way of achieving this is to have a large data sample whose average is the mean state. Due to the lack of observational data, especially in the Arctic Ocean, this technique is not feasible.

- Similarly, defining what is meant by the "mean component" is non-trivial in the physical ocean. Ideally, we would require a mean such that the residual term is precisely the geostrophic turbulence that we are interested in. However, the ocean exhibits a multitude oscillations and variability, such as seasonal and diurnal cycles, tides and many other non-linear effects from a combination of these and other processes, hence an average which is applied across this variability will include these

effects in the residual components.

- This problem also applies to GCMs which are often the culmination of a number of generations of research and development with respect to ocean processes. This means that a GCM often has numerous parameterisations and modules, which are designed to give a better representation of the ocean but make separating the useful components for this study non-trivial.

- Finally, the complex nature of GCMs mean that there is potentially a large saving of computational power than can be made by simplifying the problem into an idealised situation.

Starting from the full primitive equations, we need to carefully make assumptions and simplifications to create a representation of the ocean which is simple enough for our purposes but still a close enough approximation to the ocean that any results are ultimately useful. Hence, we now set out the criteria required for such a model.

- Firstly, the governing equations obviously must be non-linear or else there will be no turbulence and nothing to diagnose.

- The models must be able to cope with a realistic range of topographic slopes. In the Arctic Ocean the sea floor drops by around 3000 metres over 10's of kilometres in places.

- Baroclinic effects must be represented. It is well understood that a major effect of eddies is the baroclinic instability process that GM attempts to represent.

- The model must be fast. The whole point of making these idealisation is to have model that can be run at high resolution quickly.

- As mentioned above, we must be able to define an averaging operator which allows for the decomposition into a reasonable "mean component" and "eddy component".

In this section we follow the development of such a model

3.1 Stacked Shallow Water Theory

For our study, the equations that will give us the most efficient model whilst capturing the processes we would like are the stacked shallow water equations. Whilst this is a common simplification it is worth investigating whether it is an appropriate simplification to make here. In deriving the shallow water equations we make approximations which are frequently made in most GFD analyses. The first of these approximations to make is that the ocean incompressible or specifically the Boussinesq approximation. This is reasonable given the small size of deviations in density from the mean state that occurs in the ocean (Vallis (2006)). The second approximation that is made is that the fluid is hydrostatic. That is to say that the equation

$$\partial p/\partial z + \rho g = 0$$

holds, where p is pressure, ρ is density, g is gravitational acceleration and z is the vertical coordinate. Despite the fact that non-hydrostatic effects are likely to affect the vertical velocity, since there are only limited areas in the Arctic where dense water could overspill into less dense water, it is sensible to assume the hydrostatic approximation by scale arguments: the vertical components of velocity will be orders of magnitude smaller than the horizontal velocities. Finally we assume the are are no non-adiabatic processes. This give us the hydrostatic, Boussinesq primitive equations:

$$\frac{Du}{Dt} - fv = -\frac{1}{\rho}\frac{\partial p}{\partial x} + F_u - D_u, \tag{3.1.1a}$$

$$\frac{Dv}{Dt} + fu = -\frac{1}{\rho}\frac{\partial p}{\partial y} + F_v - D_v, \tag{3.1.1b}$$

$$\frac{\partial p}{\partial z} + \rho g = 0, \tag{3.1.1c}$$

$$\frac{\partial u}{\partial x} + \frac{\partial v}{\partial y} + \frac{\partial w}{\partial z} = 0, \tag{3.1.1d}$$

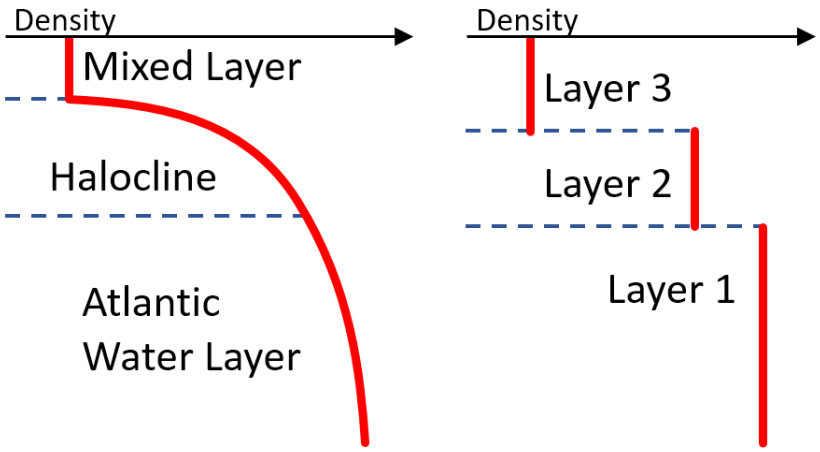


Figure 3.1.1: A more realistic continuous density profile (left) compared to the discontinuous, piecewise constant density profile of the stacked shallow water equations with 3 layers (right)

where (u, v) are the horizontal velocities, w the vertical velocity, f is the Coriolis parameter, and F_u, F_v, D_u and D_v are the u- and v-components of the forcing and dissipation.

The next step is to approximate the vertical density profile as a stack of layers of fluid of constant densities, as in Figure 3.1.1. This is to allow the shallow water approximation to be made whilst allowing for baroclinic effects by deriving the shallow water equations for each layer separately. Formally, the density profile is split into N sections with constant densities ρ_1 through to ρ_N, where $n = 1$ is the lowest layer and $n = N$ is the uppermost layer. Integrating the hydrostatic equation downwards from the surface yields

$$p(x, y, z) = \sum_{k=n+1}^{N} (g\rho_k h_k) + g\rho_n \left(\eta_{n+\frac{1}{2}} - z\right) \tag{3.1.2}$$

for $\eta_{n-\frac{1}{2}} \leq z \leq \eta_{n+\frac{1}{2}}$. Here $\eta_{n+\frac{1}{2}}(x, y, t)$, $\eta_{n-\frac{1}{2}}(x, y, t)$ are the depths of the interfaces above and below layer n respectively and $h_n = \eta_{n+\frac{1}{2}} - \eta_{n-\frac{1}{2}}$ is the vertical thickness of layer n. Similarly, by integrating the continuity equation over a layer, since we have

assumed that we are adiabatic, we have

$$\begin{aligned} 0 &= \int_{\eta_{n-\frac{1}{2}}}^{\eta_{n+\frac{1}{2}}} \left(\frac{\partial u}{\partial x} + \frac{\partial v}{\partial y} + \frac{\partial w}{\partial z} \right) \mathrm{d}z \\ &= \frac{\partial}{\partial x} \int_{\eta_{n-\frac{1}{2}}}^{\eta_{n+\frac{1}{2}}} u \mathrm{d}z + \frac{\partial}{\partial y} \int_{\eta_{n-\frac{1}{2}}}^{\eta_{n+\frac{1}{2}}} v \mathrm{d}z - \left[u \frac{\partial z}{\partial x} \right]_{\eta_{n-\frac{1}{2}}}^{\eta_{n+\frac{1}{2}}} - \left[v \frac{\partial z}{\partial y} \right]_{\eta_{n-\frac{1}{2}}}^{\eta_{n+\frac{1}{2}}} + [w]_{\eta_{n-\frac{1}{2}}}^{\eta_{n+\frac{1}{2}}} \\ &= \frac{\partial h_n}{\partial t} + \frac{\partial h_n u_n}{\partial x} + \frac{\partial h_n v_n}{\partial y}. \end{aligned} \tag{3.1.3}$$

Here we have used that

$$w = \frac{\partial z}{\partial t} + u \frac{\partial z}{\partial x} + v \frac{\partial z}{\partial y} \qquad \text{at} \qquad z = \eta_{n+\frac{1}{2}}, \eta_{n-\frac{1}{2}},$$

and

$$u_n = \tfrac{1}{h_n} \textstyle\int_{\eta_{n-\frac{1}{2}}}^{\eta_{n+\frac{1}{2}}} u \mathrm{d}z \qquad \text{and} \qquad v_n = \tfrac{1}{h_n} \textstyle\int_{\eta_{n-\frac{1}{2}}}^{\eta_{n+\frac{1}{2}}} v \mathrm{d}z.$$

By also defining the Montgomery potential as

$$m_n(x, y, t) = p + g \rho_n z = \sum_{k=n}^{N} \left(\rho_N g_{k+\frac{1}{2}} \eta_{k+\frac{1}{2}} \right)$$

where $g_{n+\frac{1}{2}} = (\rho_n - \rho_{n+1}) / \rho_N$, we have the stacked shallow water equations as derived in Vallis (2006) and Cushman-Roisin and Beckers (2011),

$$\frac{Du_n}{Dt} - f v_n = -\frac{1}{\rho_n} \frac{\partial m_n}{\partial x} + F_{u_n} - D_{u_n}, \tag{3.1.4a}$$

$$\frac{Dv_n}{Dt} + f u_n = -\frac{1}{\rho_n} \frac{\partial m_n}{\partial y} + F_{v_n} - D_{v_n}, \tag{3.1.4b}$$

$$0 = \frac{\partial h_n}{\partial t} + \frac{\partial h_n u_n}{\partial x} + \frac{\partial h_n v_n}{\partial y}. \tag{3.1.4c}$$

We have three equations and the unknowns, h_n, u_n and v_n, for each layer n.

It is worth noticing, here, the similarity between these equations and the isopycnal primitive equations set out by Young (2012), and repeated in Section 2. However, one should be aware that the two sets of equations describe different realities; h_n, for ex-

ample, is not equivalent to $\sigma = -\partial z/\partial\rho$ since in the shallow water equations σ is not well-defined due to ρ being piecewise constant, vertically. This distinction is critical when considering the interfaces between each layer. In the isopycnal primitive equations the velocities, the Montgomery potential, the energetics are all continuous throughout the water column, whereas in shallow water there is a discontinuous jump between the layers. This causes problems when considering the transfer of information between different layers. To demonstrate this let us derive conservation of energy. By dotting the momentum equations, 3.1.4a and 3.1.4b, with $h_n\boldsymbol{u}_n$ we gain an equation for the kinetic energy, $K_n = \frac{1}{2}\left|\boldsymbol{u}_n\right|^2$,

$$\frac{\partial h_n K_n}{\partial t} + \frac{\partial h_n K_n u_n}{\partial x} + \frac{\partial h_n K_n v_n}{\partial y} = -h_n u_n \frac{1}{\rho_n}\frac{\partial m_n}{\partial x} - h_n v_n \frac{1}{\rho_n}\frac{\partial m_n}{\partial y}, \tag{3.1.5}$$

or in non-conservative form,

$$\frac{DK_n}{Dt} = -u_n \frac{1}{\rho_n}\frac{\partial m_n}{\partial x} - v_n \frac{1}{\rho_n}\frac{\partial m_n}{\partial y}, \tag{3.1.6}$$

where the forcing and dissipation terms have been ignored. Now, since the each layer has constant density, the total potential energy in a column of water is easily calculated as $\sum_{n=1}^{N}\rho_n g h_n \eta_n$ where $\eta_n = \frac{1}{2}\left(\eta_{n-\frac{1}{2}} + \eta_{n+\frac{1}{2}}\right)$ is the centre of mass of each layer in the water column. By using that $h_n = \eta_{n+\frac{1}{2}} - \eta_{n-\frac{1}{2}}$ and manipulating the summation indices, we can also write

$$\sum_{n=1}^{N}\rho_n g h_n \eta_n = \sum_{n=1}^{N}\frac{1}{2}\rho_n g\left(\eta^2_{n+\frac{1}{2}} - \eta^2_{n-\frac{1}{2}}\right) = \sum_{n=1}^{N}\frac{1}{2}\rho_N g_{n+\frac{1}{2}}\eta^2_{n+\frac{1}{2}} - \rho_1 g\eta^2_{\frac{1}{2}},$$

where we note that $\eta_{\frac{1}{2}}$ is the bottom topography and so is constant in time. The total energy in the water column must therefore be

$$\sum_{n=1}^{N}\rho_n\left(h_n K_n + g h_n \eta_n\right).$$

Combining this with Equation (3.1.5) we can write down an equation for the evolution of

this energy,

$$\begin{aligned}&\frac{\partial}{\partial t}\sum_{n=1}^{N}\rho_n\left(h_nK_n+gh_n\eta_n\right)\\&=-\sum_{n=1}^{N}\boldsymbol{\nabla}_\rho\left(\rho_nh_nK_n\boldsymbol{u}_n\right)-\sum_{n=1}^{N}h_n\boldsymbol{u}_n\boldsymbol{\nabla}_\rho m_n+\sum_{n=1}^{N}\frac{1}{2}\rho_Ng_{n+\frac{1}{2}}\frac{\partial}{\partial t}\eta_{n+\frac{1}{2}}^2.\end{aligned}\tag{3.1.7}$$

This can be manipulated to give a less opaque equation. Firstly by applying the product rule to $\sum_{n=1}^{N}h_n\boldsymbol{u}_n\boldsymbol{\nabla}_\rho m_n$ and using the continuity equation, Equation (3.1.4c), we obtain

$$\begin{aligned}\frac{\partial}{\partial t}\sum_{n=1}^{N}\rho_n\left(h_nK_n+gh_n\eta_n\right)=&-\sum_{n=1}^{N}\boldsymbol{\nabla}_\rho\left[h_n\left(\rho_nK_n+m_n\right)\boldsymbol{u}_n\right]\\&-\sum_{n=1}^{N}\frac{\partial}{\partial t}\left(h_n\right)m_n+\sum_{n=1}^{N}\frac{1}{2}\rho_Ng_{n+\frac{1}{2}}\frac{\partial}{\partial t}\eta_{n+\frac{1}{2}}^2.\end{aligned}\tag{3.1.8}$$

Now, by using $h_n=\eta_{n+\frac{1}{2}}-\eta_{n-\frac{1}{2}}$ and $m_n=m_{n+1}+\rho_Ng_{n+\frac{1}{2}}\eta_{n+\frac{1}{2}}$ we have

$$\begin{aligned}&\frac{\partial}{\partial t}\sum_{n=1}^{N}\rho_n\left(h_nK_n+gh_n\eta_n\right)+\sum_{n=1}^{N}\boldsymbol{\nabla}_\rho\left[h_n\left(\rho_nK_n+m_n\right)\boldsymbol{u}_n\right]\\&\qquad=-\sum_{n=1}^{N}\frac{\partial}{\partial t}\left(\eta_{n+\frac{1}{2}}\right)m_{n+1}+\sum_{n=1}^{N}\frac{\partial}{\partial t}\left(\eta_{n-\frac{1}{2}}\right)m_n\\&\qquad=-\frac{\partial}{\partial t}\left(\eta_{N+\frac{1}{2}}\right)m_{N+1}+\frac{\partial}{\partial t}\left(\eta_{\frac{1}{2}}\right)m_1.\end{aligned}\tag{3.1.9}$$

Integrating over the entire domain makes the right hand side equal to zero since $m_{n+1}=0$ and $\eta_{\frac{1}{2}}$ is the bottom topography and so is constant in time.

So far, there haven't been any problems; however, one would then expect to be able to write down an equation for the energy of a water column in a single layer, i.e. for $\rho_n\left(h_nK_n+gh_n\eta_n\right)$. But, this is not so simple because now the transfer of energy between layers which cancelled neatly through the full water column need to be taken accounted

for:

$$\begin{aligned}\frac{\partial}{\partial t}\rho_n\left(h_nK_n+gh_n\eta_n\right) =& -\boldsymbol{\nabla}_\rho\left(\rho_nh_nK_n\boldsymbol{u}_n\right)-h_n\boldsymbol{u}_n\boldsymbol{\nabla}_\rho m_n\\ &+\frac{1}{2}\rho_ng\frac{\partial}{\partial t}\left(\eta_{n+\frac{1}{2}}^2-\eta_{n-\frac{1}{2}}^2\right)\\ =& -\boldsymbol{\nabla}_\rho\left[h_n\left(\rho_nK_n+m_n\right)\boldsymbol{u}_n\right]\\ &-\frac{\partial}{\partial t}\left(h_n\right)m_n+\frac{1}{2}\rho_ng\frac{\partial}{\partial t}\left(\eta_{n+\frac{1}{2}}^2-\eta_{n-\frac{1}{2}}^2\right)\\ =& -\boldsymbol{\nabla}_\rho\left[h_n\left(\rho_nK_n+m_n\right)\boldsymbol{u}_n\right]\\ &-\frac{\partial}{\partial t}\left(\eta_{n+\frac{1}{2}}\right)\left(m_{n+1}-\rho_{n+1}g\eta_{n+\frac{1}{2}}\right)\\ &+\frac{\partial}{\partial t}\left(\eta_{n-\frac{1}{2}}\right)\left(m_n-\rho_ng\eta_{n-\frac{1}{2}}\right).\end{aligned} \tag{3.1.10}$$

Since $m_{n+1}-\rho_{n+1}g\eta_{n+\frac{1}{2}}=p|_{z=\eta_{n+\frac{1}{2}}}$ and $m_n-\rho_ng\eta_{n-\frac{1}{2}}=p|_{z=\eta_{n-\frac{1}{2}}}$ then the last two terms represent the transfer of energy to the layer above and from the layer below respectively. But Equation (3.1.10) can be rearranged both as

$$\begin{aligned}\frac{\partial}{\partial t}\left(\rho_nh_nK_n+\frac{1}{2}\rho_Ng_{n+\frac{1}{2}}\eta_{n+\frac{1}{2}}^2\right) =& -\boldsymbol{\nabla}_\rho\left[h_n\left(\rho_nK_n+m_n\right)\boldsymbol{u}_n\right]\\ &-\frac{\partial}{\partial t}\left(\eta_{n+\frac{1}{2}}\right)m_{n+1}+\frac{\partial}{\partial t}\left(\eta_{n-\frac{1}{2}}\right)m_n\end{aligned} \tag{3.1.11}$$

or

$$\begin{aligned}\frac{\partial}{\partial t}\left(\rho_nh_nK_n+\frac{1}{2}\rho_Ng_{n-\frac{1}{2}}\eta_{n-\frac{1}{2}}^2\right) =& -\boldsymbol{\nabla}_\rho\left[h_n\left(\rho_nK_n+m_n\right)\boldsymbol{u}_n\right]\\ &-\frac{\partial}{\partial t}\left(\eta_{n+\frac{1}{2}}\right)m_n+\frac{\partial}{\partial t}\left(\eta_{n-\frac{1}{2}}\right)m_{n-1};\end{aligned} \tag{3.1.12}$$

or in fact, any combination of the two

$$\begin{aligned}\frac{\partial}{\partial t}\left(\rho_nh_nK_n+\frac{1}{2}\lambda\rho_Ng_{n+\frac{1}{2}}\eta_{n+\frac{1}{2}}^2+\frac{1}{2}\left(1-\lambda\right)\rho_Ng_{n-\frac{1}{2}}\eta_{n-\frac{1}{2}}^2\right) =& -\boldsymbol{\nabla}_\rho\left[h_n\left(\rho_nK_n+m_n\right)\boldsymbol{u}_n\right]\\ &-\lambda\frac{\partial}{\partial t}\left(\eta_{n+\frac{1}{2}}\right)m_{n+1}+\lambda\frac{\partial}{\partial t}\left(\eta_{n-\frac{1}{2}}\right)m_n\\ &-\left(1-\lambda\right)\frac{\partial}{\partial t}\left(\eta_{n+\frac{1}{2}}\right)m_n+\left(1-\lambda\right)\frac{\partial}{\partial t}\left(\eta_{n-\frac{1}{2}}\right)m_{n-1},\end{aligned} \tag{3.1.13}$$

where $0 \leq \lambda \leq 1$. The reason for this is that the Montgomery potential, m_n, is constant in the vertical in the layers and discontinuous across the interfaces between the layers. Compare with Equation (2.4.3) where the vertical transfer of energy is given by $\left(\frac{\partial \eta}{\partial t} m\right)_b$ and recall that since density is constant within a layer, $\frac{\partial}{\partial b}$ is not well-defined, and so for these equations the idea of potential energy is degenerative. However, for the sake of making progress with this discussion we will take the appropriate definition of potential energy as the term which appears in Equation (3.1.11).

3.2 Eddy Stresses

In a similar fashion to the thickness weighted average formulation for the primitive equations derived by Young (2012) (see Section 2.4), we can derive mean equations for Equation (3.1.4) using a thickness weighted averaging operator. First we define the operator to be $\overline{\psi} = \langle h_n \psi \rangle / \langle h_n \rangle$, for a variable ψ living in layer n, where $\langle \psi \rangle$ is a standard average operator, satisfying the standard axioms of an averaging operator (for a more precise definition see Maddison and Marshall (2013)); and their residuals, $\psi' = \psi - \overline{\psi}$ and $\psi^{\#} = \psi - \langle \psi \rangle$. By multiplying Equations (3.1.4a) and (3.1.4b) by h_n and using Equation (3.1.4c), we have that

$$\frac{\partial}{\partial t}(h_n u_n) + \frac{\partial}{\partial x}(h_n u_n u_n) + \frac{\partial}{\partial y}(h_n u_n v_n) - f h_n v_n = -\frac{1}{\rho_n} h_n \frac{\partial m_n}{\partial x} + h_n F_{u_n} - h_n D_{u_n}, \quad \text{(3.2.1a)}$$

$$\frac{\partial}{\partial t}(h_n v_n) + \frac{\partial}{\partial x}(h_n u_n v_n) + \frac{\partial}{\partial y}(h_n v_n v_n) + f h_n u_n = -\frac{1}{\rho_n} h_n \frac{\partial m_n}{\partial y} + h_n F_{v_n} - h_n D_{v_n}, \quad \text{(3.2.1b)}$$

$$0 = \frac{\partial h_n}{\partial t} + \frac{\partial}{\partial x}(h_n u_n) + \frac{\partial}{\partial y}(h_n v_n). \quad \text{(3.2.1c)}$$

Applying the non-thickness weighted averaging operator to these equations then gives us

$$\begin{aligned} \frac{\partial}{\partial t}\left(\langle h_n \rangle \overline{u_n}\right) + \frac{\partial}{\partial x}\left(\langle h_n \rangle \overline{u_n u_n}\right) + \frac{\partial}{\partial y}\left(\langle h_n \rangle \overline{u_n v_n}\right) - f \langle h_n \rangle \overline{v_n} \\ = -\frac{1}{\rho_n}\left\langle h_n \frac{\partial m_n}{\partial x} \right\rangle + \langle h_n \rangle \overline{F}_{u_n} - \langle h_n \rangle \overline{D}_{u_n}, \end{aligned} \quad \text{(3.2.2a)}$$

$$\begin{aligned}\frac{\partial}{\partial t}\left(\langle h_n\rangle\,\overline{v_n}\right)+\frac{\partial}{\partial x}\left(\langle h_n\rangle\,\overline{u_n v_n}\right)+\frac{\partial}{\partial y}\left(\langle h_n\rangle\,\overline{v_n v_n}\right)+f\,\langle h_n\rangle\,\overline{u_n}&\\ =-\frac{1}{\rho_n}\left\langle h_n\frac{\partial m_n}{\partial y}\right\rangle+\langle h_n\rangle\,\overline{F}_{v_n}-\langle h_n\rangle\,\overline{D}_{v_n},&\end{aligned}\tag{3.2.2b}$$

$$0=\frac{\partial\,\langle h_n\rangle}{\partial t}+\frac{\partial}{\partial x}\left(\langle h_n\rangle\,\overline{u_n}\right)+\frac{\partial}{\partial y}\left(\langle h_n\rangle\,\overline{v_n}\right).\tag{3.2.2c}$$

Applying Reynolds decomposition it is clear that the advection terms will supply Reynolds stresses; however, the Montgomery potential term is more complicated. Recall that $h_n = \eta_{n+\frac{1}{2}} - \eta_{n-\frac{1}{2}}$ and that, by the definition of m_n, we have that $m_n = m_{n+1} + \rho_N g_{n+\frac{1}{2}}\eta_{n+\frac{1}{2}}$; hence,

$$\begin{aligned}h_n\frac{\partial m_n}{\partial x}&=\eta_{n+\frac{1}{2}}\frac{\partial m_n}{\partial x}-\eta_{n-\frac{1}{2}}\frac{\partial m_n}{\partial x}\\ &=\eta_{n+\frac{1}{2}}\frac{\partial}{\partial x}\left(m_{n+1}+\rho_N g_{n+\frac{1}{2}}\eta_{n+\frac{1}{2}}\right)-\eta_{n-\frac{1}{2}}\frac{\partial m_n}{\partial x}\\ &=\left(\eta_{n+\frac{1}{2}}\frac{\partial m_{n+1}}{\partial x}-\eta_{n-\frac{1}{2}}\frac{\partial m_n}{\partial x}\right)+\frac{1}{2}\rho_N g_{n+\frac{1}{2}}\frac{\partial}{\partial x}\left(\eta^2_{n+\frac{1}{2}}\right),\end{aligned}\tag{3.2.3}$$

and the equivalent for the y-component. Comparing this with the second terms in Equation (2.4.4d) and it is easy to identify these terms as being the form stress between layer n and the layers above and below plus the potential energy. This also means that there is the same degeneracy as we had when deriving the energy equations in Section 3.1 meaning that

$$\begin{aligned}h_n\frac{\partial m_n}{\partial x}=&\lambda\left[\left(\eta_{n+\frac{1}{2}}\frac{\partial m_{n+1}}{\partial x}-\eta_{n-\frac{1}{2}}\frac{\partial m_n}{\partial x}\right)+\frac{1}{2}\rho_N g_{n+\frac{1}{2}}\frac{\partial}{\partial x}\left(\eta^2_{n+\frac{1}{2}}\right)\right]\\ &+(1-\lambda)\left[\left(\eta_{n+\frac{1}{2}}\frac{\partial m_n}{\partial x}-\eta_{n-\frac{1}{2}}\frac{\partial m_{n-1}}{\partial x}\right)+\frac{1}{2}\rho_N g_{n-\frac{1}{2}}\frac{\partial}{\partial x}\left(\eta^2_{n-\frac{1}{2}}\right)\right]\end{aligned}\tag{3.2.4}$$

for $0 \leq \lambda \leq 1$. However, for the sake of simplicity, let us just consider the case $\lambda = 1$. By decomposing Equation (3.2.2) and dividing through by $\langle h_n\rangle$ we have that

$$\frac{\mathring{D}\overline{u}_n}{Dt}-f\overline{v}_n=-\frac{1}{\rho_n}\frac{\partial\,\langle m\rangle_n}{\partial x}-\langle h_n\rangle^{-1}\boldsymbol{\nabla}_3\cdot\boldsymbol{E}^u+\overline{F}_{u_n}-\overline{D}_{u_n},\tag{3.2.5a}$$

$$\frac{\mathring{D}\overline{v}_n}{Dt}+f\overline{u}_n=-\frac{1}{\rho_n}\frac{\partial\,\langle m\rangle_n}{\partial y}-\langle h_n\rangle^{-1}\boldsymbol{\nabla}_3\cdot\boldsymbol{E}^v+\overline{F}_{v_n}-\overline{D}_{v_n},\tag{3.2.5b}$$

$$0 = \frac{\partial \langle h_n \rangle}{\partial t} + \frac{\partial}{\partial x}\left(\langle h_n \rangle \overline{u_n}\right) + \frac{\partial}{\partial y}\left(\langle h_n \rangle \overline{v_n}\right). \tag{3.2.5c}$$

Here

$$\frac{\mathring{D}\overline{v}_n}{Dt} = \frac{\partial}{\partial t} + \overline{u}_n \frac{\partial}{\partial x} + \overline{v}_n \frac{\partial}{\partial y}$$

is the mean convective derivative in layer n; $\boldsymbol{\nabla}_3$ is a special operator defined as

$$\boldsymbol{\nabla}_3 = \left(\frac{\partial}{\partial x}, \frac{\partial}{\partial y}, \frac{\partial}{\partial n}\right),$$

such that

$$\frac{\partial \psi}{\partial n} = \left(\psi_{n+\frac{1}{2}} - \psi_{n-\frac{1}{2}}\right),$$

where $\psi_{n+\frac{1}{2}}$ and $\psi_{n-\frac{1}{2}}$ are the values of ψ on the interfaces above and below layer n respectively; and $\boldsymbol{E}^u$, $\boldsymbol{E}^v$ are the eddy stresses

$$\begin{aligned}
\boldsymbol{E}^u &= \langle h_n \rangle \begin{pmatrix} \overline{u'_n u'_n} \\ \overline{u'_n v'_n} \\ 0 \end{pmatrix} + \begin{pmatrix} \frac{1}{2}\rho_N g_{n+\frac{1}{2}} \left\langle \eta^{\#}_{n+\frac{1}{2}} \eta^{\#}_{n+\frac{1}{2}} \right\rangle \\ 0 \\ \left\langle \eta^{\#} m^{\#}_x \right\rangle \end{pmatrix}, \\
\boldsymbol{E}^v &= \langle h_n \rangle \begin{pmatrix} \overline{u'_n v'_n} \\ \overline{v'_n v'_n} \\ 0 \end{pmatrix} + \begin{pmatrix} 0 \\ \frac{1}{2}\rho_N g_{n+\frac{1}{2}} \left\langle \eta^{\#}_{n+\frac{1}{2}} \eta^{\#}_{n+\frac{1}{2}} \right\rangle \\ \left\langle \eta^{\#} m^{\#}_y \right\rangle \end{pmatrix}.
\end{aligned} \tag{3.2.5d}$$

As before, this can be written as a tensor,

$$\boldsymbol{E} = \begin{pmatrix} -M + K + P & N & 0 \\ N & M + K + P & 0 \\ R & S & 0 \end{pmatrix}, \tag{3.2.5e}$$

where

$$\begin{aligned} M &= \tfrac{\langle h_n\rangle}{2}\left(\overline{v_n'v_n'} - \overline{u_n'u_n'}\right), \quad K = \tfrac{\langle h_n\rangle}{2}\left(\overline{u_n'u_n'} + \overline{v_n'v_n'}\right), \quad N = \langle h_n\rangle \overline{u_n'v_n'}, \\ P &= \tfrac{1}{2}\rho_N g_{n+\frac{1}{2}}\left\langle \eta^{\#}_{n+\frac{1}{2}}\eta^{\#}_{n+\frac{1}{2}}\right\rangle, \quad R = \left\langle \eta^{\#} m_x^{\#}\right\rangle \qquad \text{and} \qquad S = \left\langle \eta^{\#} m_y^{\#}\right\rangle; \end{aligned} \tag{3.2.6}$$

once again this can be bounded by the eddy energy,

$$\|\boldsymbol{E}\| \leq 2\left(K + P\right) \equiv 2E. \tag{3.2.7}$$

3.2.1 Potential Vorticity Equations

With the above, we have a formulation for the averaged system which is equivalent to the unaveraged system but with the addition of an eddy stress term in the momentum equation. This means that one can derive an equation for PV using the averaged system in an identical way to the unaveraged system. Hence we have that the PV for the averaged system is given by

$$\mathring{q}_n = \frac{f + \frac{\partial \overline{v}_n}{\partial x} - \frac{\partial \overline{u}_n}{\partial y}}{\langle h_n\rangle}, \tag{3.2.8}$$

satisfying

$$\frac{\mathring{D}\mathring{q}_n}{Dt} = -\left\langle h_n\right\rangle^{-1} \boldsymbol{\nabla}\cdot\mathring{\boldsymbol{F}}, \tag{3.2.9}$$

where $\mathring{\boldsymbol{F}} = \langle h_n\rangle^{-1}\left(\boldsymbol{\nabla}_3\cdot\left(\langle h_n\rangle\boldsymbol{E}^v\right), -\boldsymbol{\nabla}_3\cdot\left(\langle h_n\rangle\boldsymbol{E}^u\right)\right)^{\top}$ and $\boldsymbol{E}^u$, $\boldsymbol{E}^v$ are the columns of $\boldsymbol{E}$. Here the forcing and dissipation terms, $\overline{\boldsymbol{F}}$ and $\overline{\boldsymbol{D}}$, have been ignored, but would be inherited from the momentum equation in the natural way. It should be noted that whilst $\overline{\mathring{q}_n} = \mathring{q}_n$, $\mathring{q}_n \neq \overline{q}_n$. However, $\mathring{q}_n$ is more useful than the averaged PV, $\overline{q}_n$, because the eddy flux $\mathring{\boldsymbol{F}}$ is directly related to the Eliassen-Palm tensor, whilst $\mathring{q}_n$ involves the weighted mean velocities and so is precisely the PV for the averaged system. Despite this, it is worth discussing $\overline{q}_n$ for comparison. By applying the thickness weighted averaging operator to the definition of q_n we get

$$\overline{q}_n = \frac{f + \frac{\partial\langle v\rangle_n}{\partial x} - \frac{\partial\langle u\rangle_n}{\partial y}}{\langle h_n\rangle}. \tag{3.2.10}$$

Then we can derive the dynamical equation for $\overline{q}$,

$$\begin{aligned}
0 &= \left\langle h_n \left(\frac{\partial q_n}{\partial t} + \boldsymbol{u}_n \cdot \boldsymbol{\nabla} q_n \right) \right\rangle = \left\langle \frac{\partial}{\partial t} \left(h_n q_n \right) + \boldsymbol{\nabla} \cdot \left(h_n \boldsymbol{u}_n q_n \right) \right\rangle \\
&= \frac{\partial}{\partial t} \left(\langle h_n \rangle \, \overline{q}_n \right) + \boldsymbol{\nabla} \cdot \left(\langle h_n \rangle \, \overline{\boldsymbol{u}_n q_n} \right) \\
&= \frac{\partial}{\partial t} \left(\langle h_n \rangle \, \overline{q}_n \right) + \boldsymbol{\nabla} \cdot \left(\langle h_n \rangle \, \overline{\boldsymbol{u}}_n \, \overline{q}_n \right) + \boldsymbol{\nabla} \cdot \left(\langle h_n \rangle \, \overline{\boldsymbol{u}'_n q'_n} \right) \\
&= \langle h_n \rangle \left(\frac{\partial \overline{q}_n}{\partial t} + \overline{\boldsymbol{u}}_n \cdot \boldsymbol{\nabla} \overline{q}_n \right) + \boldsymbol{\nabla} \cdot \left(\langle h_n \rangle \, \overline{\boldsymbol{u}'_n q'_n} \right)
\end{aligned} \tag{3.2.11}$$

as used by Greatbatch (1998) and Smith (1999).

3.2.2 Eddy Energy Equation

Similarly we can take the unweighted average of the conservative energy equation, Equation (3.1.11), to give an energy budget for the mean state. For the mean of the energy equation we have

$$\begin{aligned}
\frac{\partial}{\partial t} \left(\rho_n \langle h_n \rangle \, \overline{K_n} + \frac{1}{2} \rho_N g_{n+\frac{1}{2}} \left\langle \eta^2_{n+\frac{1}{2}} \right\rangle \right) + \boldsymbol{\nabla} \left[\langle h_n \rangle \, \overline{\left(\rho_n K_n + m_n \right) \boldsymbol{u}_n} \right] \\
= - \left\langle \frac{\partial}{\partial t} \left(\eta_{n+\frac{1}{2}} \right) m_{n+1} \right\rangle + \left\langle \frac{\partial}{\partial t} \left(\eta_{n-\frac{1}{2}} \right) m_n \right\rangle .
\end{aligned} \tag{3.2.12}$$

But because we also have an equation for the mean dynamics, we can also write down the equation for the mean energy as

$$\begin{aligned}
\frac{\partial}{\partial t} \left(\rho_n \langle h_n \rangle \, \frac{1}{2} \left| \overline{\boldsymbol{u}}_n \right|^2 + \frac{1}{2} \rho_N g_{n+\frac{1}{2}} \left\langle \eta_{n+\frac{1}{2}} \right\rangle^2 \right) + \boldsymbol{\nabla} \left[\langle h_n \rangle \left(\rho_n \frac{1}{2} \left| \overline{\boldsymbol{u}}_n \right|^2 + \langle m_n \rangle \right) \overline{\boldsymbol{u}}_n \right] \\
= - \overline{\boldsymbol{u}}_n \cdot \left(\boldsymbol{\nabla}_3 \cdot \boldsymbol{E} \right) - \frac{\partial}{\partial t} \left(\left\langle \eta_{n+\frac{1}{2}} \right\rangle \right) \langle m_{n+1} \rangle + \frac{\partial}{\partial t} \left(\left\langle \eta_{n-\frac{1}{2}} \right\rangle \right) \langle m_n \rangle ,
\end{aligned} \tag{3.2.13}$$

where we note that this equation differs from Equation (3.1.11) by simply the eddy stress term $\overline{\boldsymbol{u}}_n \cdot \left(\boldsymbol{\nabla}_3 \cdot \boldsymbol{E} \right)$. We can therefore difference Equation (3.2.13) from Equation (3.2.12)

to retrieve an equation for the eddy energy,

$$\begin{aligned}
&\frac{\partial}{\partial t}\left(\rho_n \langle h_n\rangle \frac{1}{2}\overline{|\boldsymbol{u}_n'|^2} + \frac{1}{2}\rho_N g_{n+\frac{1}{2}}\left\langle {\eta_{n+\frac{1}{2}}}^2{}^{\#}\right\rangle\right)\\
&+\boldsymbol{\nabla}\left[\langle h_n\rangle \overline{(\rho_n K_n + m_n)\,\boldsymbol{u}_n} - \langle h_n\rangle\left(\rho_n\frac{1}{2}|\overline{\boldsymbol{u}}_n|^2 + \langle m_n\rangle\right)\overline{\boldsymbol{u}}_n\right] \qquad (3.2.14)\\
&\quad = \overline{\boldsymbol{u}}_n\cdot(\boldsymbol{\nabla}_3\cdot\boldsymbol{E}) - \left\langle\frac{\partial}{\partial t}\left(\eta^{\#}_{n+\frac{1}{2}}\right)m^{\#}_{n+1}\right\rangle + \left\langle\frac{\partial}{\partial t}\left(\eta^{\#}_{n-\frac{1}{2}}\right)m^{\#}_{n}\right\rangle.
\end{aligned}$$

Unfortunately, this equation is not entirely helpful as it introduces some triple correlations, or eddy-eddy interactions, namely $\overline{K_n\boldsymbol{u}_n} - \frac{1}{2}|\overline{\boldsymbol{u}}_n|^2\overline{\boldsymbol{u}}_n$ and $\langle h_n\rangle\overline{m_n\boldsymbol{u}_n} - \langle h_n\rangle\langle m_n\rangle\overline{\boldsymbol{u}}_n = \langle h_n m_n\boldsymbol{u}_n\rangle - \langle h_n\rangle\langle m_n\rangle\overline{\boldsymbol{u}}_n$. Noting that $\overline{K_n} = \frac{1}{2}|\overline{\boldsymbol{u}}_n|^2 + \frac{1}{2}\overline{|\boldsymbol{u}_n'|^2}$ we can further write that $\overline{K_n\boldsymbol{u}_n} - \frac{1}{2}|\overline{\boldsymbol{u}}_n|^2\overline{\boldsymbol{u}}_n = \overline{K_n'\boldsymbol{u}_n'} + \frac{1}{2}\overline{|\boldsymbol{u}_n'|^2}\overline{\boldsymbol{u}}_n$. Similarly we also have $\langle h_n\rangle\overline{m_n\boldsymbol{u}_n} - \langle h_n\rangle\langle m_n\rangle\overline{\boldsymbol{u}}_n = \langle h_n\rangle\overline{m_n^{\#}\boldsymbol{u}_n'} + \langle h_n^{\#}m_n^{\#}\rangle\overline{\boldsymbol{u}}_n$. Since $\langle h_n^{\#}m_n^{\#}\rangle$ is in some sense related to the eddy potential energy we have an equation for the time evolution of eddy energy. This is, however, of limited use without making some assumptions about $\overline{K_n'\boldsymbol{u}_n'}$, $\langle h_n\rangle\overline{m_n^{\#}\boldsymbol{u}_n'}$ and the vertical transfer of eddy energy, $\left\langle\frac{\partial}{\partial t}\left(\eta^{\#}_{n-\frac{1}{2}}\right)m^{\#}_{n}\right\rangle$. But if we could say something about these correlations then we would be able to create a closure which would allow us to determine the eddy energy of the system.

3.2.3 Eddy Potential Enstrophy Equation

Potential enstrophy is more straight-forward. The unweighted average of the conservative enstrophy equation,

$$\frac{\partial}{\partial t}\left(h_n Q_n\right) + \boldsymbol{\nabla}\left(h_n\boldsymbol{u}_n Q_n\right) = 0,$$

where $Q_n = \frac{1}{2}q_n^2$, gives an enstrophy budget for the mean state,

$$\frac{\partial}{\partial t}\left(\langle h_n\rangle\overline{Q}_n\right) + \boldsymbol{\nabla}\left(\langle h_n\rangle\overline{\boldsymbol{u}_n Q_n}\right) = 0.$$

We can also write down an equation for the mean potential enstrophy, $\frac{1}{2}\overline{q}_n^2$, as

$$\frac{\partial\,\langle h_n\rangle\frac{1}{2}\overline{q}_n^2}{\partial t} + \boldsymbol{\nabla}\cdot\left(\langle h_n\rangle\overline{\boldsymbol{u}}_n\frac{1}{2}\overline{q}_n^2\right) = -\overline{q}_n\boldsymbol{\nabla}\cdot\left(\langle h_n\rangle\overline{\boldsymbol{u}_n' q_n'}\right).$$

Subtracting these equations from one another we attain

$$\frac{\partial \langle h_n \rangle \frac{1}{2}\overline{q_n'^2}}{\partial t} + \boldsymbol{\nabla} \cdot \left(\langle h_n \rangle \overline{\boldsymbol{u}_n' Q_n'} + \langle h_n \rangle \overline{\boldsymbol{u}}_n \frac{1}{2}\overline{q_n'^2} \right) = \overline{q}_n \boldsymbol{\nabla} \cdot \left(\langle h_n \rangle \overline{\boldsymbol{u}_n' q_n'} \right) \tag{3.2.15}$$

Again we have a correlation, $\overline{\boldsymbol{u}_n' Q_n'}$, where $Q_n' = Q_n - \overline{Q}_n$, which causes problems; but if this can be ignored or parameterised in some other way then we would have an equation for the evolution of eddy potential enstrophy.

The discussion of these equations is important since the structure of the Eliassen-Palm tensor is dependent on the eddy energy and eddy potential enstrophy. Hence, for a viable eddy parameterisation to be achieved from this theory a model must be able to judge how much eddy energy and eddy potential enstrophy it has available. This can of course be done by prescribing the eddy energy and eddy potential enstrophy, but ideally it would be useful to have a way of predicting these quantities from the dynamics of the system. What Equations (3.2.14) and (3.2.15) demonstrate is how the eddy energy and eddy potential enstrophy interact with the mean field through $\overline{\boldsymbol{u}}_n \cdot (\boldsymbol{\nabla}_3 \cdot \boldsymbol{E})$ and $\overline{q}_n \boldsymbol{\nabla} \cdot \left(\langle h_n \rangle \overline{\boldsymbol{u}_n' q_n'} \right)$.

In order to apply the theory in this section we need to define an averaging operator that correctly splits a field up into its mean and eddy components. There are a number of ways to do this. The more legitimate way of achieving this is to average over a large ensemble of models where the eddy field in each ensemble member is in a different state. However, this method is hugely computationally expensive, requiring a large number of ensemble members to achieve an appropriate mean and eddy decomposition. Plus if the mean state of the system being modelled happens to diverge between ensemble members then the ensemble mean stops being representative of the mean state. Two other ways of decomposing the system into mean and eddy components is with temporal or spatial averages. Spatial means require a large domain to average over to be effective on their own and a certain amount of spatial symmetry; a zonal average will have problems if the topography, for example, varies in the zonal direction. However, if there is a usable spatial symmetry, then it is possible to use an averaging operator that averages both temporally and spatially without much of a loss in computational efficiency. However, for a temporal

average to be valid the system needs to be in a statistically steady state, or ergodic. That is to say that over a long averaging window $\partial\overline{\phi}/\partial t \sim 0$ for any variable ϕ in the system.

Overall we have highlighted how the eddy field interacts with the mean field, as well as a way of decomposing a model into its mean and eddy fields. The momentum equations admit an Eliassen-Palm flux tensor, which can be bounded by eddy energy and eddy potential enstrophy as proposed by Marshall et al. (2012) and Maddison and Marshall (2013). The energy and potential enstrophy equations are more complicated as the mean equations for the eddy component of these quantities, Equations (3.2.14) and (3.2.15), both contain triple correlations. However, the equations still demonstrate how the mean and eddy energy and potential enstrophy interact. To decompose a system into its mean and eddy components we will use spatial and temporal averages; the first requires a certain amount of spatial symmetry whilst the second requires the system to be in a statistically steady state. The greatest challenge to come is the creation a model that will allow the application of the diagnostics we have derived in the most effective way possible.

3.3 Model Setup

Now that we have our governing equations, we need to solve them. To do this we discretise the equations onto an Arakawa C-grid and then solve for future times using the 3rd-order Adams-Bashforth scheme. Next, to satisfy the Courant-Friedrichs-Lewy condition (Courant et al. (1928)), the time-step and grid spacing must satisfy $\Delta x/\Delta t \leq c_{\max}$ where Δx is the smallest grid spacing, Δt is the time-step and $c_{\max}$ is the fastest speed at which information is propagated. In our equations this is the surface gravity wave speed, $\sqrt{gH}$, where H is the maximum fluid depth. However, since the next fastest waves are the internal gravity waves with speeds of order $\sqrt{g_{n+\frac{1}{2}}H}$, approximately 1000 times slower than the surface gravity waves, it makes sense to suppress the surface gravity waves. To do this in such a way that is consistent with mass, momentum and energy conservation, we impose the rigid-lid approximation. By imagining a flat plate placed across the surface,

we can re-interpret the pressure fluctuations from a free surface as the fluid pushing or pulling on the plate and the resulting force applied to the fluid in reaction.

3.3.1 Rigid-Lid Approximation

In practise, to apply the rigid-lid approximation we add a barotropic pressure gradient to the momentum equations. This corrects the time-stepped velocities to ensure that conservation of mass is satisfied. Since the rigid-lid imposes a boundary above the fluid whilst the topography imposes a similar one below we have that

$$0 = \frac{\partial}{\partial t}\sum_{n=1}^{N} h_n = -\sum_{n=1}^{N}\left(\frac{\partial}{\partial x}(u_n h_n) + \frac{\partial}{\partial y}(v_n h_n)\right), \tag{3.3.1}$$

where $(u_n, v_n) = (u_n^*, v_n^*) - \Delta t \boldsymbol{\nabla} p$ is the corrected velocities, p is the barotropic pressure correction, Δt is the time-step and (u_n^*, v_n^*) are the time-stepped velocities. This implies that to calculate p we need to solve

$$\frac{\partial}{\partial x}\left(H\frac{\partial p}{\partial x}\right) + \frac{\partial}{\partial y}\left(H\frac{\partial p}{\partial y}\right) = \sum_{n=1}^{N}\left(\frac{\partial}{\partial x}(u_n^* h_n) + \frac{\partial}{\partial y}(v_n^* h_n)\right) \tag{3.3.2}$$

where $H = \sum_{n=1}^{N} h_n$. The right hand side is known after time-stepping and so Equation (3.3.2) is simply an elliptic equation.

Equation (3.3.2) is solved using the conjugate gradient method to within a small tolerance. A bespoke solver was written for specifically for this purpose. Since the discretised left hand side of Equation (3.3.2) is sparse, the speed of the conjugate gradient method was improved by choosing an appropriate preconditioning matrix. The choice that appeared to make a reasonable improvement is the operation

$$\overline{\left(\overline{1/H}^{x} p\right)}^{x} + \overline{\left(\overline{1/H}^{y} p\right)}^{y} \tag{3.3.3}$$

applied to p, where bars denote averaging in the x and y directions respectively.

3.3.2 Eddy Deformation Radius and Model Resolution

Typical scales in the Arctic are ~ 10km for the lateral scale of mesoscale eddies, $3-5$km for ocean depth, whilst typical speeds are a few $\mathrm{cm\,s^{-1}}$; because of this we shall rescale the dimensions so that the model is not operating with values of vastly different magnitudes and hence reduces the chance for floating point errors. Firstly, the layer thicknesses, h_n, are scaled by the mean depth of the topography so that $\int_D \left(\sum_{n=1}^{N} h_n\right) \mathrm{d}A / \int_D \mathrm{d}A \equiv 1$, where D is the domain, N the number of layers and $\mathrm{d}A = \mathrm{d}x\,\mathrm{d}y$. The first baroclinic deformation radius is approximately $L_D = \sqrt{g'H}/f_0$, where $g' = g\,(\rho_1 - \rho_N)/\rho_N$ and f_0 is the local Coriolis parameter, and sets the scale of the mesoscale eddies. Hence, we take $g\,(\rho_1 - \rho_N)/\rho_N = 1$ and $f_0 = 1$ so that time is scaled by $1/f_0$ and the horizontal velocities and distances are scaled by the wave speed, $\sqrt{g'H}$ and deformation radius, $L_D = \sqrt{g'H}/f_0$.

In order to have well resolved eddies, we choose a grid resolution of $L_D/20$; meanwhile we want a domain that is at least around 10 or 20 times the mesoscale. This immediately give around a hundred thousand degrees of freedom, since we are limited by available computation resources it is not sensible to have a large domain or finer grid than this. To remove this limitation we use a doubly re-entrant domain rather than a basin with boundaries, exploiting the fact we would expect the ocean to be statistically similar across a symmetric domain and avoiding the large domain required to incorporate an entire ocean basin's dynamics. This choice does have some obvious drawbacks. Firstly, the doubly-periodic symmetry is incredibly unrealistic, the ocean is not divided into identical cubes; and so the fact that a piece of dynamics will have an identical neighbour nearby may cause some unrealistic properties. However, this will hopefully only be a problem on the largest scales. Secondly, this requires a constant Coriolis parameter which may lose us some important dynamical processes such as Rossby waves; however, at high latitudes, the Coriolis parameter is nearly constant at leading order. Finally, there is a similar issue with topography, any choice must be translationally symmetric in both the zonal and meridional directions. This limits the choices to sea mounts and ridges.

3.3.3 Wind Stress

Now, to generate dynamically interesting system we manipulate the system using the forcing and dissipation terms, $\boldsymbol{F_u} = (F_u, F_v)$ and $\boldsymbol{D_u} = (D_u, D_v)$, in Equation (3.1.4). This is typically achieved by applying parameterisations for wind stress and bottom friction. An appropriate way to parameterise wind stress in terms of relative velocity between the atmospheric velocity at 10m above sea-level and the sea surface velocity, for example as the quadratic stress

$$\boldsymbol{\tau} = \rho_a c_d \left|\boldsymbol{U}_{10} - \boldsymbol{u}_a\right| \left(\boldsymbol{U}_{10} - \boldsymbol{u}_a\right), \tag{3.3.4}$$

where $\boldsymbol{\tau}$ is the surface wind stress, ρ_a is the density of air at sea level, c_d is the drag coefficient, $\boldsymbol{u}_a$ is the ocean surface velocity and $\boldsymbol{U}_{10}$ is the wind velocity at 10m above the sea surface. The importance of using the relative velocities is well established (Duhaut and Straub (2006), Zhai and Greatbatch (2007), Hughes and Wilson (2008), Zhai et al. (2012)); however, consistent with the idealised framework in which we are working in, we assume that $|\boldsymbol{u}_a| \ll |\boldsymbol{U}_{10}|$ and $\boldsymbol{\tau} = \rho_a c_d |\boldsymbol{U}_{10}| \boldsymbol{U}_{10}$, which is simply a vector set by the magnitude and direction of the wind. Since the momentum within each layer is defined to be constant within each layer, the input of momentum from the wind is distributed through the layer giving

$$(F_{u_N}, F_{v_N}) = \boldsymbol{\tau} / (\rho_N h_N) \equiv (\tau_u, \tau_v) / (\rho_N h_N)$$

in the uppermost layer, $n = N$.

3.3.4 Bottom Friction

Now that we have a mechanism to force the system we need a mechanism of dissipating the energy input from the winds. The most physically reasonable way to do this is to introduce bottom friction to the model. Bottom friction is a drag intended to represent the shear stress felt by the ocean as it flows over the ocean floor; however, in a layered model, the bottom drag must be applied throughout the lowest layer. Since we want

the bottom friction to remove momentum from the system, it seems sensible for this to be of the form $\boldsymbol{\tau} \propto -\boldsymbol{u}_1$, where $\boldsymbol{u}_1$ is the horizontal velocity in the bottom layer. A first guess might be a linear drag, similar to the wind stress, given by $h_1 \boldsymbol{D}_{\boldsymbol{u}_1} = -r\boldsymbol{u}_1$ for some speed r. However, studies have shown (for example Grianik et al. (2004) and Arbic and Scott (2008)) that a straight-forward linear bottom friction gives rise to large, unrealistic eddies and that using a higher order polynomial gives more realistic results. One advantage of an n-polynomial bottom friction rather than a linear bottom friction is that it can be scale selective, in the sense that it is found to damp the largest eddies. We take the bottom friction to have the form

$$\boldsymbol{D}_{\boldsymbol{u}_1} = -r \left(\frac{|\boldsymbol{u}_1|}{|\boldsymbol{u}^*|} \right)^n \boldsymbol{u}_1 / h_1$$

for some typical velocity $\boldsymbol{u}^*$, natural number n and friction coefficient r. Now for $n \geq 1$ (note that for $n = 0$, this is just linear bottom friction), $\boldsymbol{D}_{\boldsymbol{u}_1}$ is stronger when $|\boldsymbol{u}_1| > |\boldsymbol{u}^*|$ and weaker when $|\boldsymbol{u}_1| < |\boldsymbol{u}^*|$ than in the linear case. Hence, the higher order polynomials limit the flows from becoming too strong by selectively limiting the stronger currents. This means it is possible that, by tuning r, $|\boldsymbol{u}^*|$ and n, a bottom friction can be chosen that limits the along-topography flow with minimal effect on the eddy field.

In order to tune these parameters, we will diagnose the topostrophy which we introduced in Section 1.3, defined as $\tau = (\boldsymbol{f} \wedge \boldsymbol{u}) \cdot \boldsymbol{\nabla} H$. Topostrophy represents the extent to which the flow follows topography. With this tool we can explore the sensitivity of the models ability to generate along-topography flow to the choice of bottom friction. Figure 3.3.1 shows the mean topostrophy for the initial spin up of several models with a topographic ridge similar to the schematics in Figure 4.0.1 and Figure 4.0.2. The first thing to note is how damped the topostrophy is in the linear bottom friction case. It is clear that the bottom friction is inhibiting the eddies greatly and so stopping the formation of along-topography flows. In the quadratic cases, there is a lot more variability in the topostrophy, indicating that there is a much more active eddy field. However again, there is no obvious along-topography flow, meaning the bottom friction is still too broadly dissipative. It

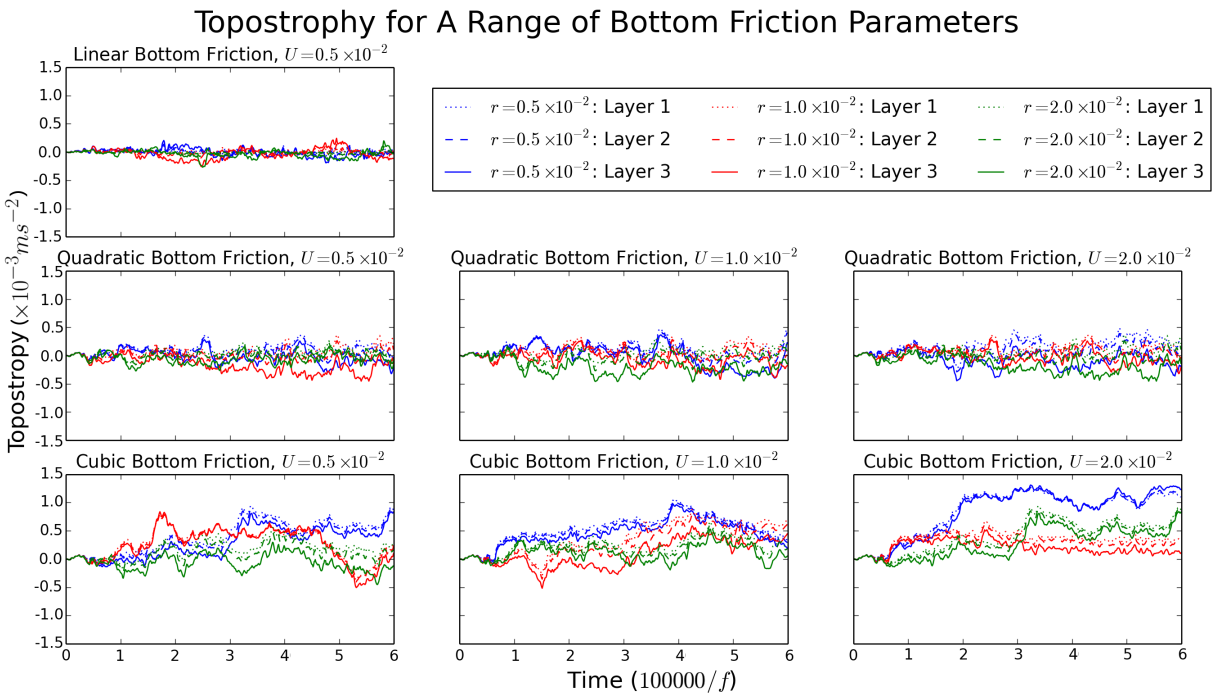


Figure 3.3.1: Topostrophy for a range of different bottom friction parameters. Each plot shows a certain choice of $|\boldsymbol{u}^*|$ and n, with three different friction coefficients shown in red, green and blue. The topostrophies calculated from the velocities in layers 1, 2 and 3 in each model are shown by dotted, dashed and solid line respectively. Since $|\boldsymbol{u}^*|$ is non-existent in the linear case only one plot is needed. Note that $100000/f \sim 20$ years at $\sim 70^\circ$ North.

should however be noted that the lower layers have more positive topostrophy than the upper layers, indicating that there is some along-topography flow in the lower layers but that it is not being replicated throughout the water column; the cubic drag models are much more interesting. The flow appears to have much more freedom to generate flows, whilst still being capped by $|\boldsymbol{u}^*|$. $|f| = 1$, $\boldsymbol{\nabla} H \sim 0.1$ and so $|\boldsymbol{u}| \sim 0.01 < |\boldsymbol{u}^*|$. Given these results it seems sensible to use the cubic parameterisation for bottom friction. It is worth noticing that there is little physical rationale for choosing one parameterisation over another, other than one might produce more physically appealing results. Finally, we also require grid-scale dissipation. This is to dissipate the numerical noise which develops at the grid-scale from the cascade of enstrophy In these models we use biharmonic diffusion with the Smagorinsky viscosity (Smagorinsky (1963)).

3.3.5 Summary of Model Setup and Example Output

In summary, we have created a model that is simple and fast to run, but still is a reasonable representation of a stratified ocean over variable topography. Using this model, we can apply averaging operators to diagnose eddy-mean interactions in the presence of topography using the theory developed in Section 3.2. However, before we get to topography, let us convince ourselves that we have a model that is consistent with the equations derived in Chapter 3 and our conception of ocean dynamics. Using the wind stress that we will discuss in detail in Section 4.1 in a three-layered domain without topography we spin up a model to examine the resulting eddy field and momentum and energy balances. Equation (3.1.11) demonstrates there is an energy that is conserved except for forcing and dissipation, in this case due to the wind stress, bottom friction and viscosity. In Figure 3.3.2, it is seen that the bottom friction balances the energy input from the wind over a large time window beyond the initial spin up. Figure 3.3.3 shows a snapshot of

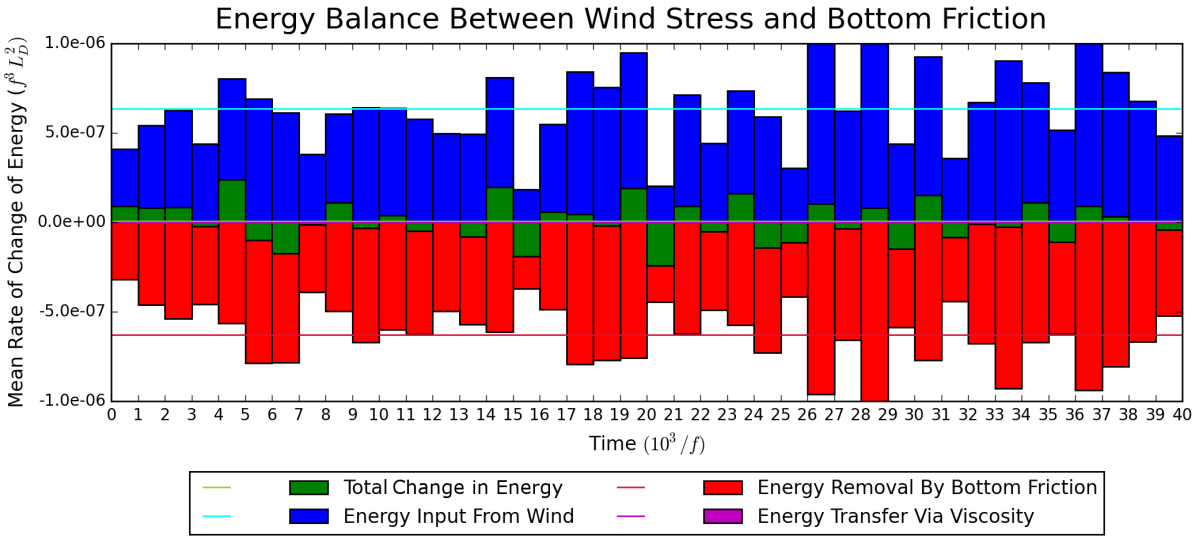


Figure 3.3.2: Energy change in topography-less model represented by mean rate of change of energy per unit column over $10^3/f$ time window. Energy change is split into energy input by wind stress (blue), dissipation through bottom friction (red) and transfer to small scale through the viscosity (magenta), and hence the viscosity is negligible. The sum of these is the total change in energy shown by the green bars. The lines are the mean changes over the whole time window for wind stress, bottom friction, viscosity and total (blue, red, magenta and green respectively). The overall energy change is only about 1% of the wind input and friction dissipation but is vanishingly small when the first few averaging windows, i.e. the spin up period, are excluded.

the PV field at a time around $40 \times 10^3/f$ into the integration. The surface layer shows a strong eddy field with eddies around the scale of the deformation radius and some filamentation. The middle layer has basically uniform PV as one would expect since the only non-conservative term in the PV equation for this layer is the viscosity, which is small. In the lowest layer the eddy field is mostly dissipated by the bottom friction, which is scale selective for strong flows leaving only shallow PV gradients. This means there is slow and large scale barotropic flow present in all layers whose magnitude is set by the bottom friction and spatial scale appears to be set by the domain size, whilst in there is a strong eddying baroclinic flow whose spatial scale is set by the first baroclinic deformation radius and strength is set by the wind. In the time averaged mean, the variations of the PV from the mean f/h_n are vanishingly small, as shown in Figure 3.3.4, where with an averaging window of around $30 \times 10^3/f$ the time-mean PV varies by around 10% of the variability of the snapshot PV in Figure 3.3.3 whilst the time-mean flow speed is around 5%.

3.4 Summary

In this chapter we have seen the development of the Eliassen-Palm flux tensor for the stacked shallow water equations. We have demonstrated how the eddy stresses for the momentum equations are linked with the PV eddy stress, as well as re-deriving the bounds for this specific case. We have discussed in which limits these bounds hold true, i.e. in the geostrophic limit for the energy bound and in the limit of $\mathring{q} \sim \overline{q}$ for the enstrophy bound. We have the justified the steps that need to be taken to discretise our equations in order to develop a computational model that is both quick and accurately represents the original stacked shallow water equations. This has included a discussion of the rigid-lid approximation as well as forcing and dissipation in terms of the wind stress, bottom friction and grid-scale viscosity.

Overall, we have done the best we can with the tools available to satisfy the criteria set out at the start of Chapter 3. In Chapter 4 we proceed by analysing results of experiments

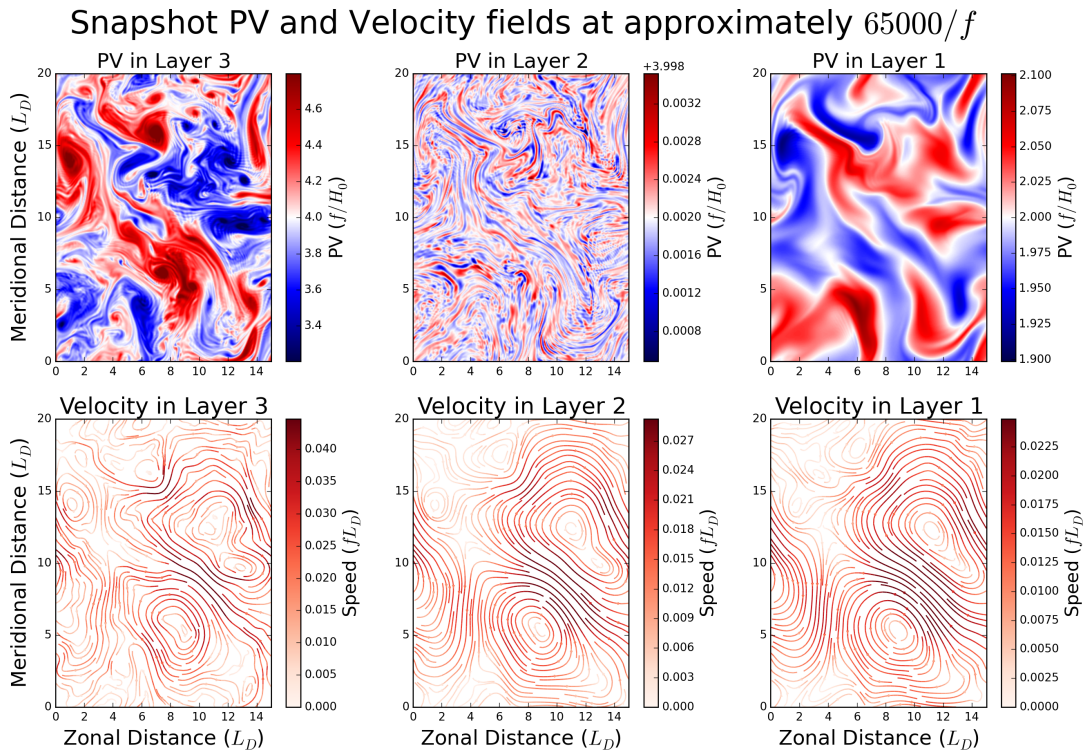


Figure 3.3.3: A snapshot of the PV and velocities in each of the three layers at around $65000f$ in time in a domain without topography. Notice that the middle layer only exhibit small fluctuations in PV whilst the lowest layer has a relatively inactive eddy field, probably dissipated by the bottom friction.

that have been generated using this model in an attempted to verify the hypotheses set out in Section 2.5.

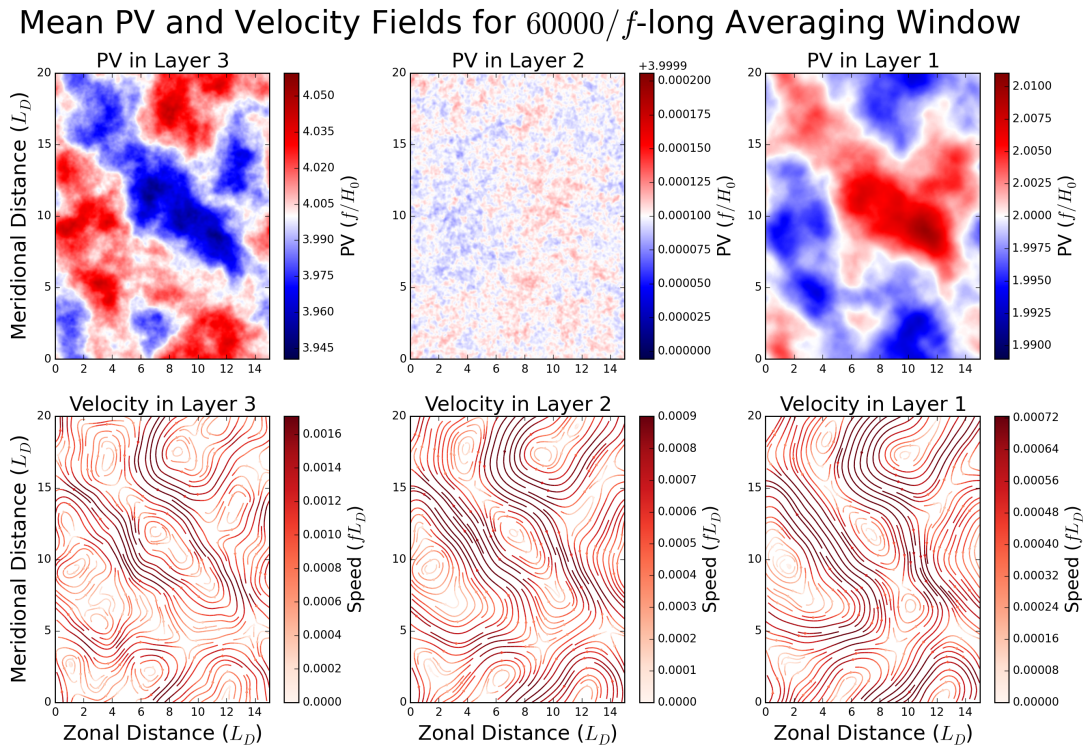


Figure 3.3.4: The thickness weighted averaged PV and velocities in each of the three layers over a window of around $60000f$ in time in a domain without topography. Notice that the PV and velocities are much reduced in the mean in comparison to Figure 3.3.3.

Chapter 4

Analysis of a hierarchy of models

Now that we have system that suits the needs that we outlined in the introduction of Chapter 3, we can proceed with investigating the role of mean-eddy flow interaction in the presence of topography. As mentioned in the previous section, due to choosing to have a doubly re-entrant domain, the choice of topography must be, zonally and meridionally, translationally symmetric. Hence, we choose to have a zonal ridge as shown in the schematics Figure 4.0.1 as well as Figure 4.0.2. Figure 4.0.2 depicts a cross-section of the initial configuration of the domain where the layer thicknesses are chosen in such a way as to attempt to reduce the chance of a layer outcropping by evenly distributing the layers above the shallowest topography. Our understanding of eddy-topography interactions built from observational data and experiments that were outlined in Chapter 1 would lead us to expect an along-topography flow to develop with an westward flow on the south side of the ridge, and an eastward flow on the north side of the ridge for a positive f_0.

4.1 Zero-Mean Wind Stress

To begin, it seems most sensible to investigate the system with the simplest possible mean dynamics. That is to say a system where the dynamical equations for the mean variables (for example Equation (3.2.5)) is only forced by the eddy-mean interaction and

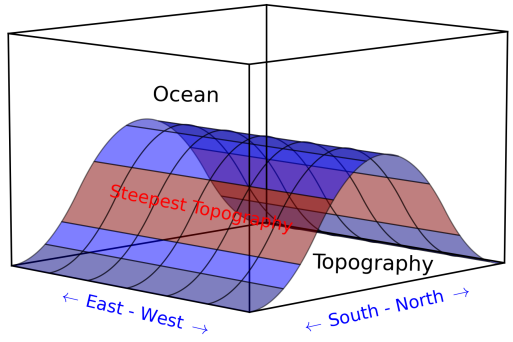


Figure 4.0.1: Schematic of the topography. The dimensions of the domain are $10L_D$ in the direction along the ridge, where L_D the deformation radius defined in the text, and $15L_D$ in the perpendicular direction. The shaded red regions demonstrate the areas of steepest topography and are replicated later on in the appropriate figures.

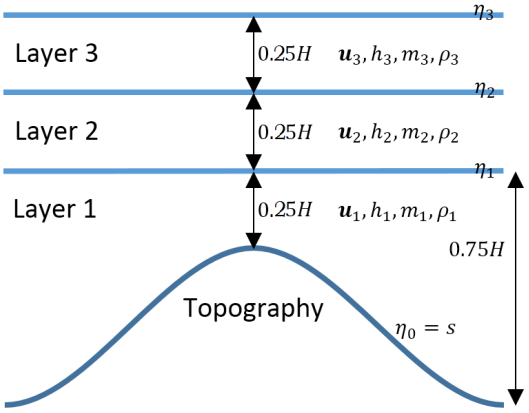


Figure 4.0.2: Cross-sectional schematic of the topography. Shows three layers of fluid, with densities ρ_1, ρ_2 and ρ_3, above the topography, s. Interfaces between individual layers, the surface and topography are labelled η_i for the interface above layer 'i' and $\eta_0 = s$.

dissipation, for example bottom friction. Of course, if the mean system is only forced by the eddy-mean interactions and dissipative forces then the only way interesting dynamics can occur is through the eddy-mean interactions. Hence, we try to generate an eddy field from some kind of forcing such that in the mean momentum equation there is no net contribution from the forcing, that is to say that for forcing, $\boldsymbol{\tau}$, we have $\overline{\boldsymbol{\tau}} \equiv 0$. On the other hand, in order to balance the energy sink due to dissipation the forcing must be a source of energy; in this case, since $\overline{\boldsymbol{\tau}} \equiv 0$, the energy must be introduced via the eddy dynamics.

To achieve such a system we introduce a spatially and temporally varying wind stress. There are a few ways this can be done. A common method is to generate a superposition of sine waves at various frequencies and phases as the stream function for the wind stress; this method is discussed at length in Koszalka et al. (2009), Thomson and McIntyre (2015) and Brannigan et al. (2015). Instead we randomly populate the domain with a collection of cyclones and anticyclones. This we achieve through a series of independent circular wind stresses that are vanishingly small far from their centres, each with a certain maximum amplitude and defined through a continuous stream function. The profile shown in

Figure 4.1.1 satisfies these conditions. This cyclone is given by

$$\frac{1}{2\pi r}(1 - e^{-r^2})e^{-r^2/2}\boldsymbol{e}_\theta,$$

where at the wrap around points half the domain away from the vortex centre the vortex is tapered rapidly to zero to avoid a discontinuity; here r is the distance from the centre of the vortex, normalised by the radius of the vortex, and $\boldsymbol{e}_\theta$ is the unit vector in the rotational direction. The vortices are also given a certain random duration, t_0, contained within a minimum and maximum duration; the vortices then grow and decline over this period in proportion to a sine wave in the range $[0, \pi]$. These vortices therefore have five properties which can be altered to create a stress field which can be implemented in the model; these are its amplitude, radius, position, duration and orientation (i.e. whether it is cyclonic or anticyclonic). By periodically generating these vortices with randomised properties we can sum them together to create a wind stress which varies in time, and in the limit of a long run time, the time-mean tends to zero. Examples of how the full wind stress field looks at different time steps are shown in Figure 4.1.2. To further ensure a vanishing mean wind stress over a long time averaging window we introduce the vortexes in cyclonic and anti-cyclonic pairs of equal size and duration to ensure that the spatial mean of the wind stress is precisely zero.

Now we must check that this wind stress satisfies our needs. The upper bound of momentum contribution from this wind stress to the time-averaged mean system is straight forward to calculate and is dependent on ratio between the longest t_0, or vortex duration, and the averaging window. So for similar wind stresses the contribution to the mean system is vanishingly small for longer averaging windows. The energy input is a little more complicated; adding the wind forcing into the mean and eddy energy equations described in Section 3.2 shows that applying the thickness weighted averaging operator to the energy equation, Equation (3.2.12), gives $\langle \boldsymbol{\tau} \rangle \cdot \langle \boldsymbol{u} \rangle$ and $\left\langle \boldsymbol{\tau}^{\#} \cdot \boldsymbol{u}^{\#} \right\rangle$ as the energy input into the mean and eddy components of the system. Taking averaging windows of $10^3/f$, Figure 4.1.3 shows that the contribution to the mean component is vanishingly

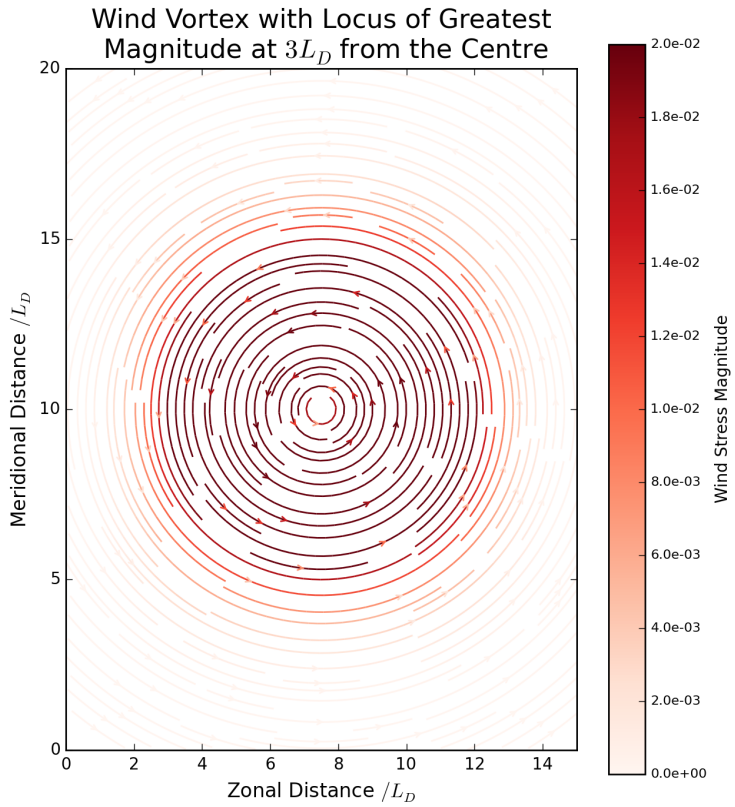


Figure 4.1.1: An example of the wind stress given by a cyclone with radius $3L_D$ centre in the middle of the domain. The heat-map shows the strength of the stresses, The stresses are tapered away from the centre of the vortex to avoid discontinuities as the domain wraps around.

small and hence the wind stress suits our purpose by almost exclusively inputting energy and momentum into the eddy component of the system.

4.2 Momentum and Energy Balances

Exploiting the symmetry of the ridge, we can average in the zonal direction as well as in time. This allows us to decompose the flow into mean field varying only in the meridional direction and an eddy field. Noting that $\frac{\partial}{\partial x}\langle ... \rangle \equiv 0$ for the zonal mean, we have that

$$\frac{\partial \overline{u}_n}{\partial t} - (f + \mathring{\zeta})\overline{v}_n = -\langle h_n \rangle^{-1} \boldsymbol{\nabla}_3 \cdot \boldsymbol{E}^u + \overline{F}_{u_n} - \overline{D}_{u_n}, \tag{4.2.1a}$$

$$\frac{\partial \overline{v}_n}{\partial t} + (f + \mathring{\zeta})\overline{u}_n = -\frac{\partial}{\partial y}\left(\frac{1}{\rho_n}\langle m \rangle_n + \frac{1}{2}|\overline{\boldsymbol{u}}_n|^2\right) - \langle h_n \rangle^{-1} \boldsymbol{\nabla}_3 \cdot \boldsymbol{E}^v + \overline{F}_{v_n} - \overline{D}_{v_n}, \tag{4.2.1b}$$

$$0 = \frac{\partial \langle h_n \rangle}{\partial t} + \frac{\partial}{\partial y}\left(\langle h_n \rangle \overline{v_n}\right), \tag{4.2.1c}$$

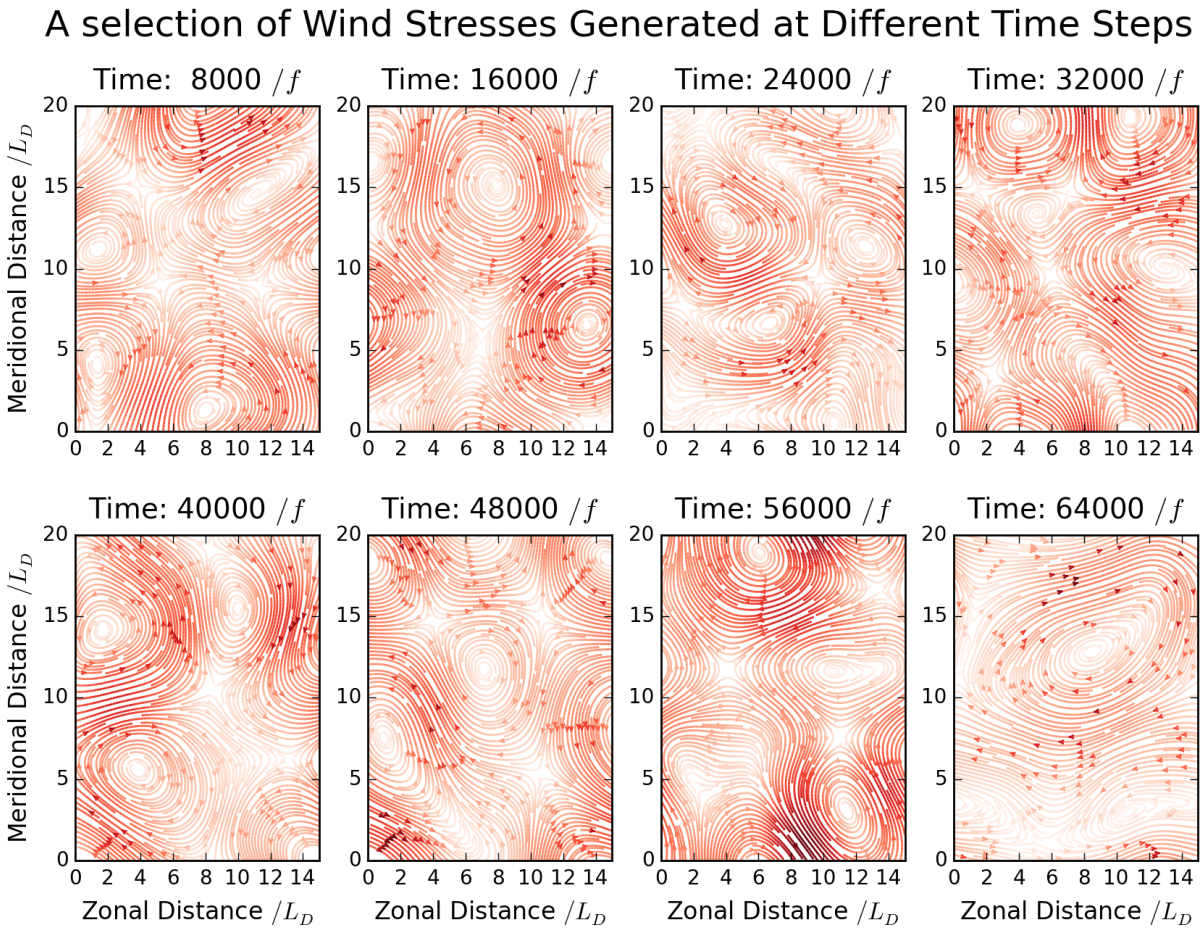


Figure 4.1.2: Eight different snapshots of the wind forcing generated by randomly seeding vortexes across the domain. These cyclones and anticyclones have a typical radii of between 5 times the Deformation Radius and half the domain size as well as a lifespan of a couple of weeks.

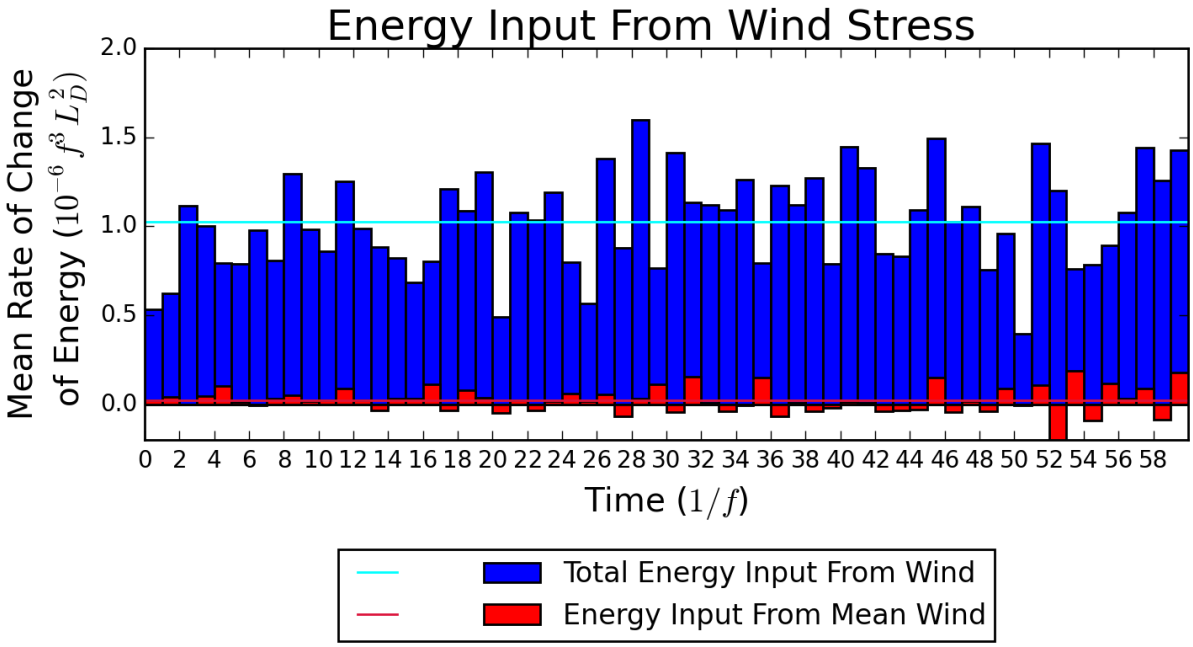


Figure 4.1.3: Energy input from the wind stress over each $10^3/f$ window. The red bars show the energy input from the mean component into the mean system, $\langle \boldsymbol{\tau} \rangle \cdot \langle \boldsymbol{u} \rangle$, in comparison to the total (mean + eddy) input (blue), $\langle \boldsymbol{\tau} \cdot \boldsymbol{u} \rangle = \langle \boldsymbol{\tau} \rangle \cdot \langle \boldsymbol{u} \rangle + \langle \boldsymbol{\tau}^{\#} \cdot \boldsymbol{u}^{\#} \rangle$. The input from the mean component into the mean system is around 2% of the total (mean + eddy) input.

where $\mathring{\zeta} = -\frac{\partial \overline{u}_n}{\partial y}$ is the relative vorticity. The eddy stresses become

$$\boldsymbol{E}^u = \begin{pmatrix} 0 \\ \langle h_n \rangle \, \overline{u_n' v_n'} \\ 0 \end{pmatrix} + \begin{pmatrix} 0 \\ 0 \\ \langle \eta^{\#} m_x^{\#} \rangle \end{pmatrix}, \tag{4.2.1d}$$

$$\boldsymbol{E}^v = \begin{pmatrix} 0 \\ \langle h_n \rangle \, \overline{v_n' v_n'} \\ 0 \end{pmatrix} + \begin{pmatrix} 0 \\ \frac{1}{2} \rho_N g_{n+\frac{1}{2}} \left\langle \eta^{\#}_{n+\frac{1}{2}} \eta^{\#}_{n+\frac{1}{2}} \right\rangle \\ \langle \eta^{\#} m_y^{\#} \rangle \end{pmatrix},$$

or as a tensor:

$$\boldsymbol{E} = \begin{pmatrix} 0 & 0 & 0 \\ N & M + K + P & 0 \\ R & S & 0 \end{pmatrix}. \tag{4.2.1e}$$

Hence in the steady state limit of $\frac{\partial \overline{\boldsymbol{u}}_n}{\partial t} \to 0$ over a long averaging window, we have that $-(f + \mathring{\zeta})\overline{v}_n$ balances the zonal eddy stresses, forcing and dissipation whilst $(f + \mathring{\zeta})\overline{u}_n + \frac{\partial}{\partial y}\left(\frac{1}{\rho_n}\langle m_n \rangle + \frac{1}{2}|\overline{\boldsymbol{u}}_n|^2\right)$ balances the meridional eddy stresses, forcing and dissipation. This can be used to demonstrate how the wind driven eddy field interacts with the mean dynamics to generate an along-topography flow.

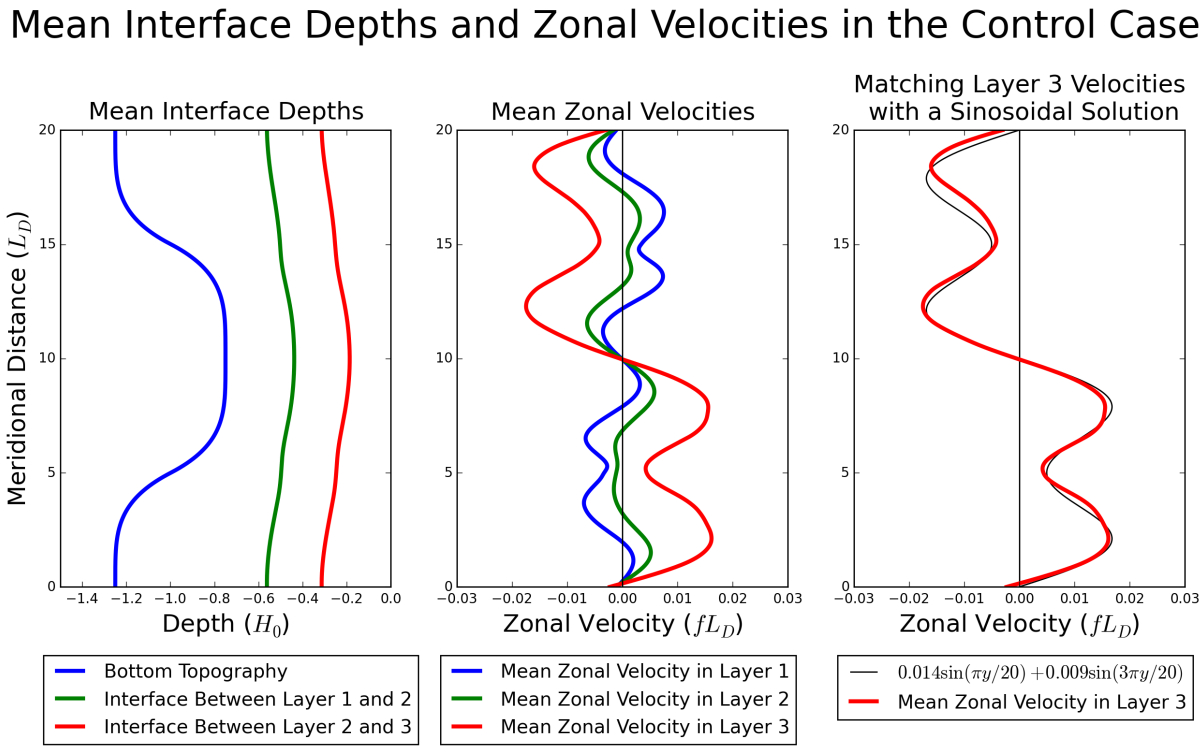


Figure 4.2.1: The mean depths of the interfaces between the layers and the thickness weighted means of the velocities average zonally and temporally over an averaging window of $6 \times 10^4/f$. The interfaces show a slight doming over the topography whilst the velocities in the lower two layers show along-topography flow in the westward direction south of the ridge and eastward, north of the ridge. The upper layer has a flow in the opposite direction to the lower layers. This flow is fitted to a periodic profile in the third frame and the claim that it could be due to homogeneous solutions produced by the elliptic solver.

Since the flow is mostly spun up well before $10.0 \times 10^3/f$ since initialisation, we take the time averaging window to be between $10.0 \times 10^3/f$ and $70.0 \times 10^3/f$, so $60.0 \times 10^3/f$ long; or assuming a latitude of around 70°N an averaging window of around 15 years. Figure 4.2.1 shows the mean depths of the interfaces and thickness weighted mean of the velocities over this time window. In the leftmost plot we see the expected slight doming over the topography, whilst in the centre plot we see along-topography flows. However,

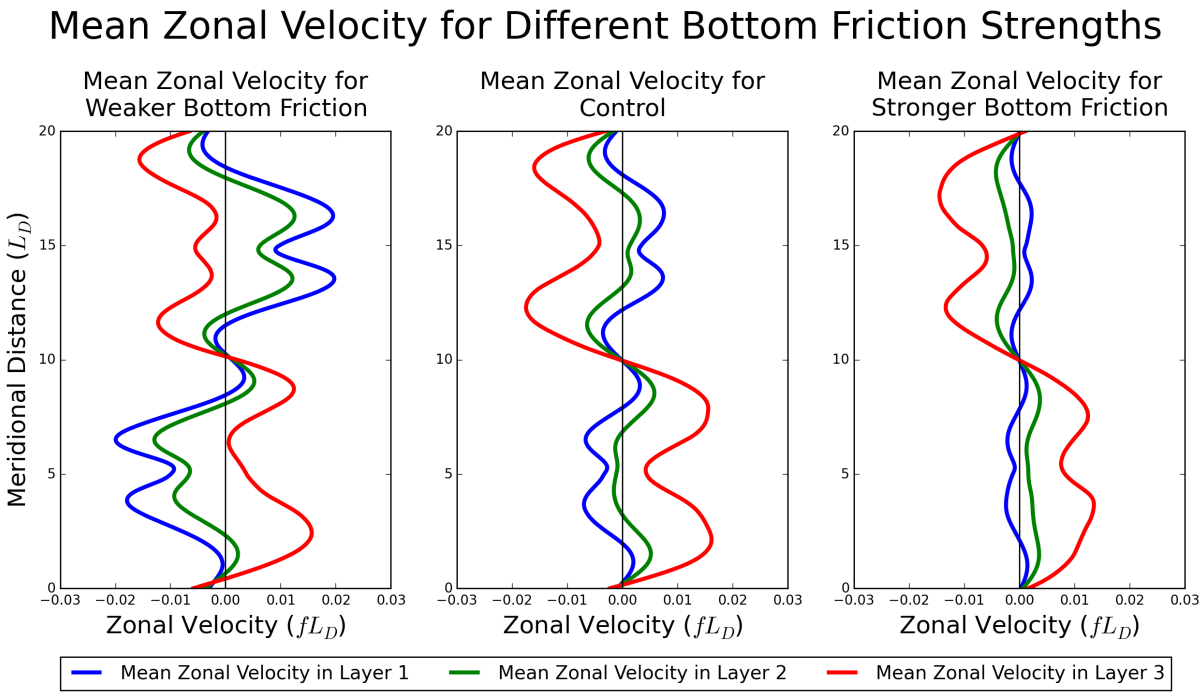


Figure 4.2.2: The thickness weighted means of the velocities average zonally and temporally over an averaging window of $6 \times 10^4/f$ for three different bottom frictions. Here the stronger bottom friction is twice as strong and the weaker bottom friction is half as strong. The along-topography flows in the bottom layers are much reduced for the stronger bottom friction and much larger when weaker. However, the flow in the upper layer is roughly the same magnitude indicating that is a persistent feature.

whilst the flows in the lowest layers are predominantly in the expected direction, that is to say in the westward direction south of the ridge and eastward north of the ridge, the uppermost layer has a flow in the opposite directions. This is a feature which occurs across all of the experiments presented in this chapter with similar magnitude and the same orientation. Take, for example, what happens when the strength of the bottom friction is varied (Figure 4.2.2). The stronger bottom friction dampens the hypothesised flow in the bottom two layers whilst the flow is stronger with weaker bottom friction, however the unexpected flow in the upper layer is unchanged in magnitude and even becomes more prominent in the middle layer when the bottom friction is stronger. Due to the persistent nature of this feature we believe that it is the result of the rigid lid approximation, specifically the application of the elliptic solver to give the barotropic pressure gradient. The idea is that the elliptic solved is admitting unrealistic homogeneous

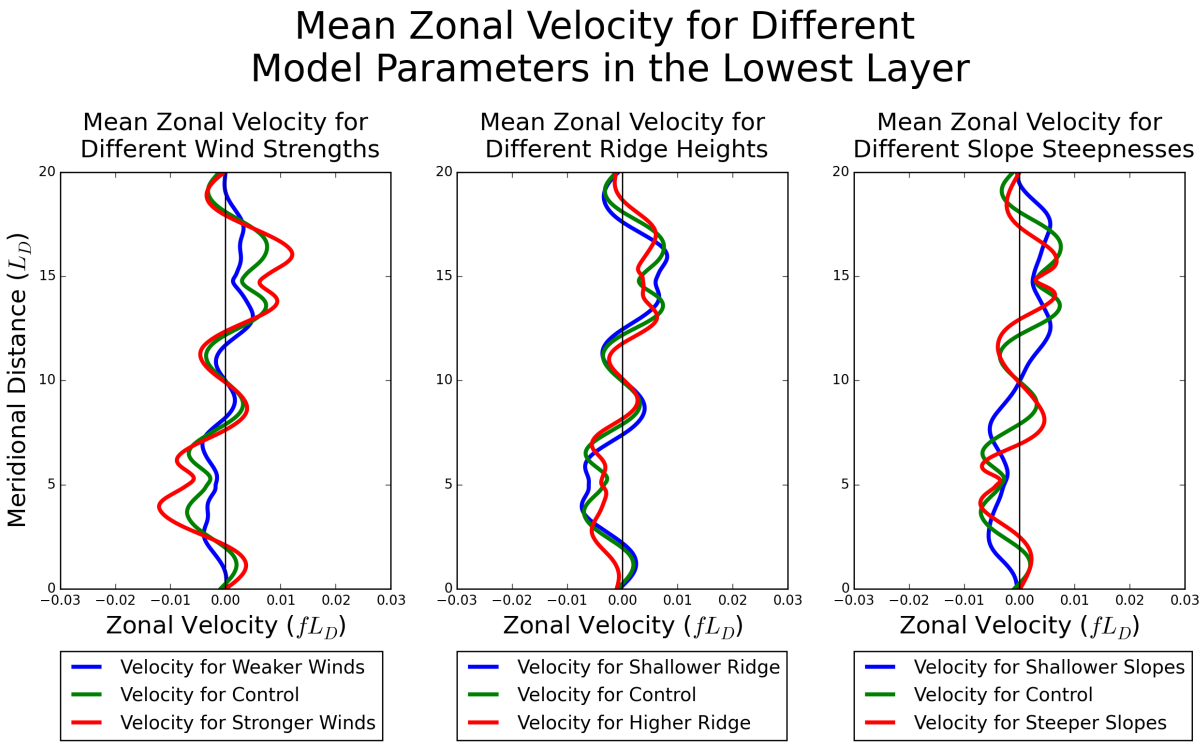


Figure 4.2.3: The thickness weighted means of the velocities in the lowest layer average zonally and temporally over an averaging window of $6 \times 10^4/f$ for three different values of three different model parameters. Changing the strength of the wind causes stronger or weaker along-topography flow as one would expect. However, changing the ridge height and steepness leads to roughly the same magnitude of along-topography flow. Instead, the structure of the flow is changed. For shallower ridges the flow is more over the steepest part of the slope than for higher ridges where the flow is more to either side. Meanwhile, the flow is broader for shallower slopes than for steeper slopes, where the flow is tighter.

periodic solutions in the meridional direction. This is then being balanced by the zonal velocities through geostophic balance. The third panel of Figure 4.2.1 shows the zonal velocities in the uppermost layer being fitted to a potential solution. In the more realistic case where there is a free-surface instead there would be eddy correlations in the form of a form stress at the surface. This form stress would act on the upper layer in an opposite direction to the form stress between the uppermost layer and the layer below, dampening the generation of such a flow. However, without running a costly free-surface model instead this theory cannot be tested and so we precede as best we can without explaining the flow in the uppermost layer.

We have just discussed, using varying bottom friction, how the flow in the uppermost layer may be a product of the pressure solver by comparing how the flow in the lowest

layer changes dramatically, whilst the uppermost layer remains effectively the same. However, varying the bottom friction is interesting in its own right; Figure 4.2.2 along with Figure 4.2.3 show how the mean zonal flow changes in the bottom layer as four different parameters are changed in the model. As we would expect, a weaker bottom friction gives a stronger flow than a stronger bottom friction, whilst a stronger wind gives a stronger flow than a weaker wind. Interestingly though, changing how extreme the topography is has little effect on the overall strength of the along-topography flow, even though one would expect more extreme topography to give a stronger along-topography flow. Instead, changing the topography changes the structure of the flow. A ridge with a smaller height allows for more of a flow along the steepest part of the topography, whilst for a higher ridge the fastest parts of the flow are moved away from the steepest part. Similarly, by keeping the ridge height the same but changing the slope steepness, the flow is more diffuse for a shallower slope, but tighter for a steeper one. Overall, it appears that that the forcing and drag are the main contributors to the strength of the along-topography flow, whilst the slope size and shape determines its structure. To understand this more deeply, we need to have a closer look at the averaged momentum balances.

Figure 4.2.4a shows hows the eddy field interacts with mean dynamics of the uppermost layer in two ways. Firstly, there are Reynolds stresses in the westward (negative) direction on the south side of the ridge and roughly equal Reynolds stresses in the eastward (positive) direction on the north side of the ridge. These Reynolds stresses are echoed in the lower layers, at least in sign if not shape or magnitude. This indicates an overall force from the eddy field in the direction of positive topostrophy. Secondly, the eddy field also generates a form stress upon the lower layers which mostly balances the Reynolds stresses and drives momentum down into the lower layers. The residual of these two components is balanced by the mean Coriolis force, which is generated by a small meridional velocity. The negative sign south of the ridge and positive north of the ridge demonstrates a migration of fluid away from the ridge in the upper layer, hinting that perhaps the fluid is not fully in a steady state and isopycnals are still increasing the

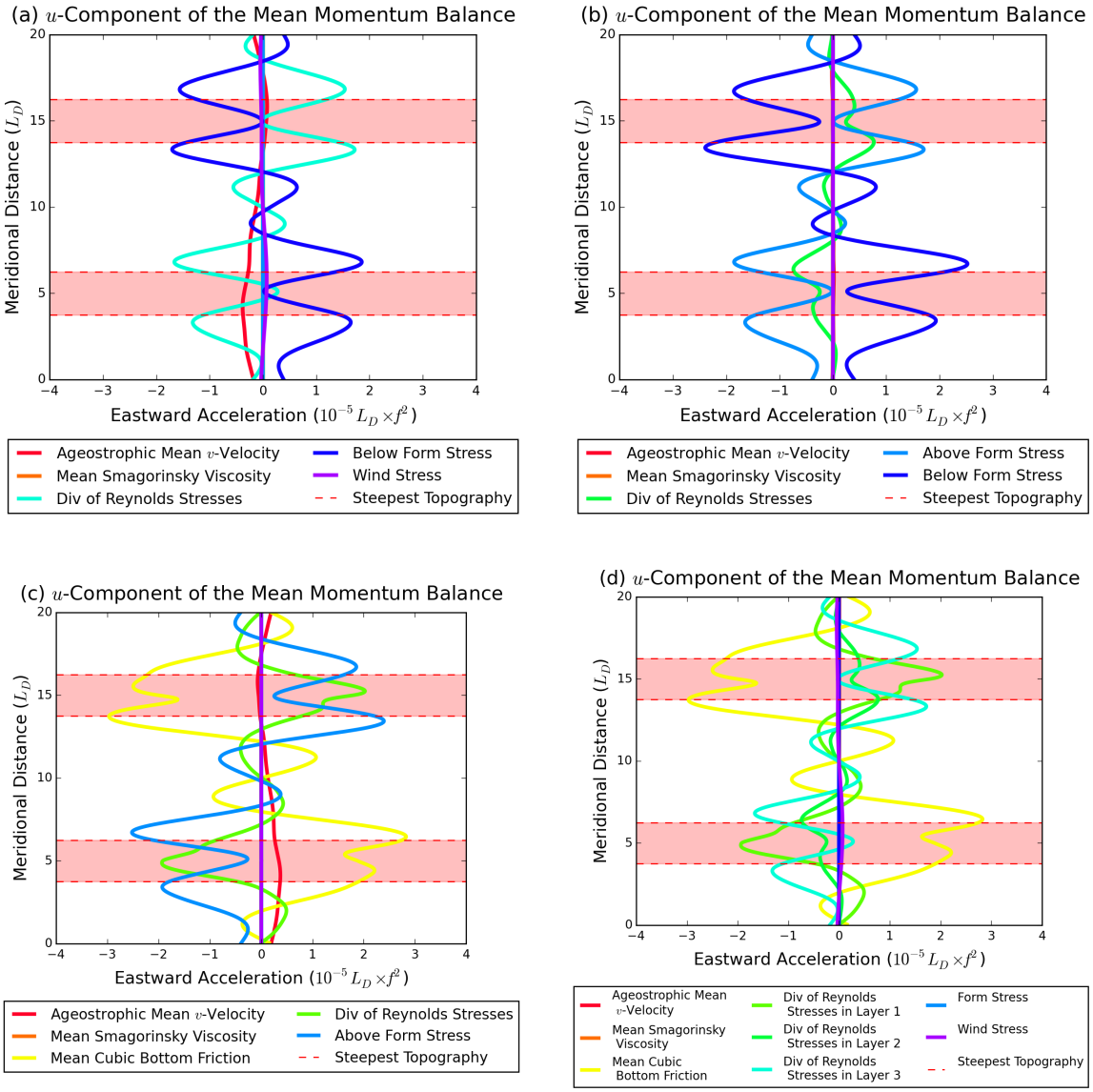


Figure 4.2.4: Zonal Momentum Balance in (a) the upper layer, (b) the middle layer (c) the lower layer and (d) the entire water column of a doubly re-entrant domain with zonal ridge and varying zero-mean wind. Red bands show regions of steepest topography. In the uppermost layer (a) the Divergence of the Reynolds stress almost precisely balances the form stress between this layer and the one below. In the middle layer (b), the difference between the form stresses balance the Reynolds stress. Finally, in the lower layer (c) the form stress and the divergence of the Reynolds stress balance the bottom friction. The upper and lower layers have a small ageostrophic Coriolis force in the balance which signifies that flow has not fully reached steady state in the meridional direction, however this cancel out in (d). Hence, the Reynolds stress divergences in the entire column balance the bottom friction as shown in (d).

"cold doming" effect above the ridge. This is most like because the meridional velocities are much slower and hence has much longer spin-up time than the zonal velocities. In the central layer, shown in Figure 4.2.4b, the form stress inherited from the upper layer combines with a smaller Reynolds stress in the positive topostrophy direction whilst being balanced by the form stress between the central and lowest layer. The lowest layer, Figure 4.2.4c, has the form stresses built up in the upper and middle layers mostly balancing the bottom friction, again there is a small Coriolis force signifying the flow onto the ridge. The bottom friction is in opposition to a westward flow south of the ridge (hence positive) and an eastward flow north of the ridge (hence negative). This implies that over the entire water column, since the form stresses between layers must cancel each other, the Reynolds stresses must balance the bottom friction by pushing the flow in the direction of positive topostrophy as shown in Figure 4.2.4d.

In the meridional direction, how the momentum tendency balances is a lot less clear. To try and make sense of it, let us first look at the geostrophic balance. In the meridional direction this is the balance between the Coriolis force due to the mean zonal velocity, $f\overline{u}_n$, and the meridional gradient of the Montgomery potential, $\rho_n^{-1}\frac{\partial}{\partial y}\langle m_n\rangle$. Figures 4.2.5a through to 4.2.5d show that the model is in almost perfect geostrophic balance. The lowest layer, Figure 4.2.5c, clearly shows an along-topography flow in the expected directions; however, Figure 4.2.5a shows that the flows are in the opposite directions in the upper layer as was discussed earlier in the section. And so, the Coriolis force almost entirely balances the gradient of the Montgomery potential. The remaining ageostrophic velocity is then balanced by the eddy stresses, as shown in Figures 4.2.6a through to 4.2.6d. Figure 4.2.6a demonstrates the problem with trying to define the potential energy in a layer; the definition we have chosen to stick with from Equation (3.1.11) means there is zero eddy potential energy in the upper layer. Since Equation (3.1.11) is a special case of Equation (3.1.13) for $\lambda = 1$ that we chose for ease of discussion and, in fact, should be interpreted as the equation for potential energy near the top of the layer, where in the upper layer the eddy potential energy is zero, whilst $\lambda = 0$ is the eddy energy near the

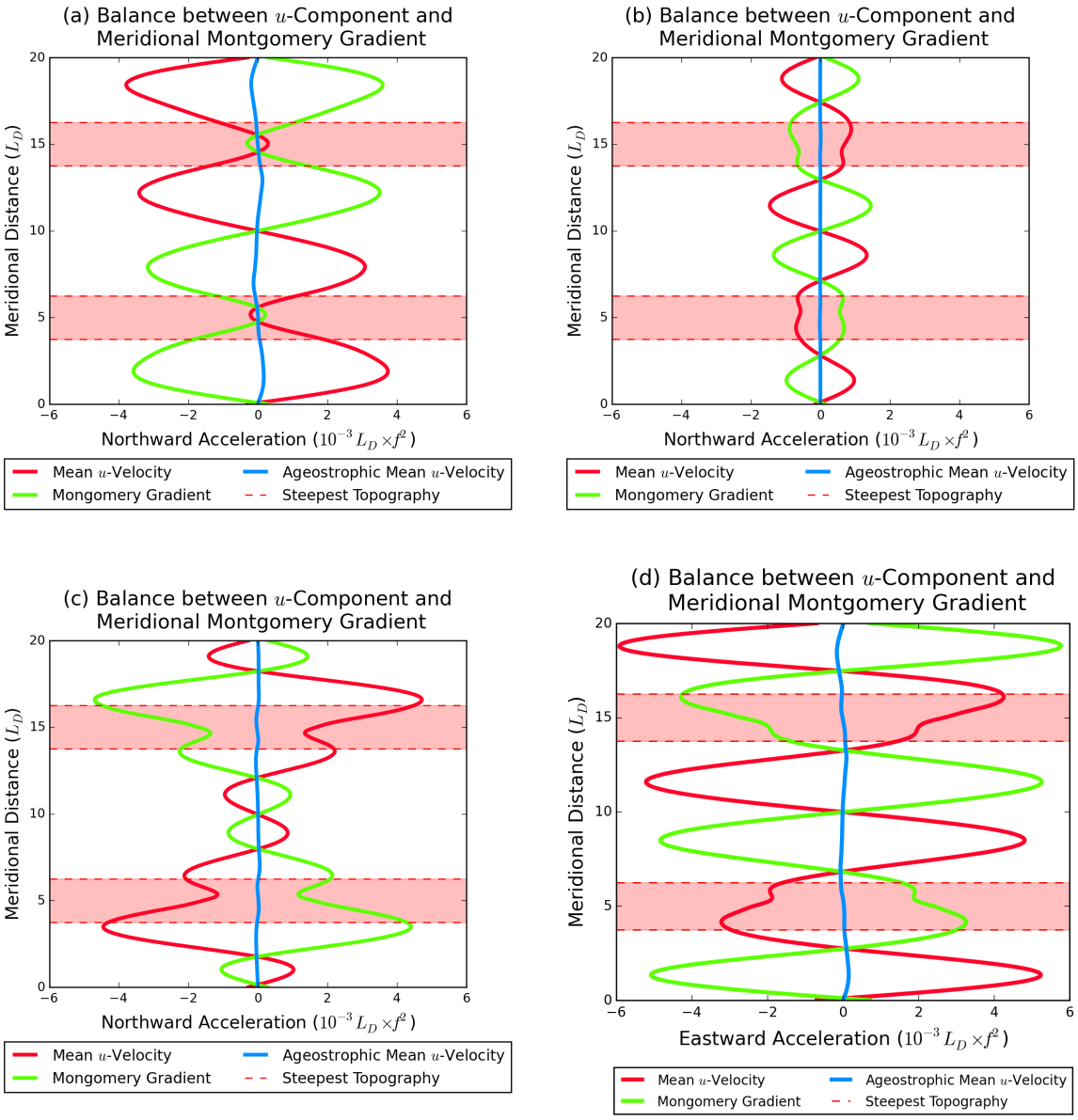


Figure 4.2.5: Balance between Coriolis force and the gradient of the Montgomery potential in the meridional direction in (a) the upper layer, (b) the middle layer (c) the lower layer and (d) the entire water column of a doubly re-entrant domain with zonal ridge and varying zero-mean wind. Red bands show regions of steepest topography. Here we see the zonal velocities that were shown in Figure 4.2.1 and how they are balanced by the meridional gradient of the Montgomery potential. (a) specifically also reflects how the zonal flow in the uppermost layer is linked to the solutions of the elliptic solver since the Montgomery potential in the uppermost layer is precisely the the pressure applied by the rigid lid.

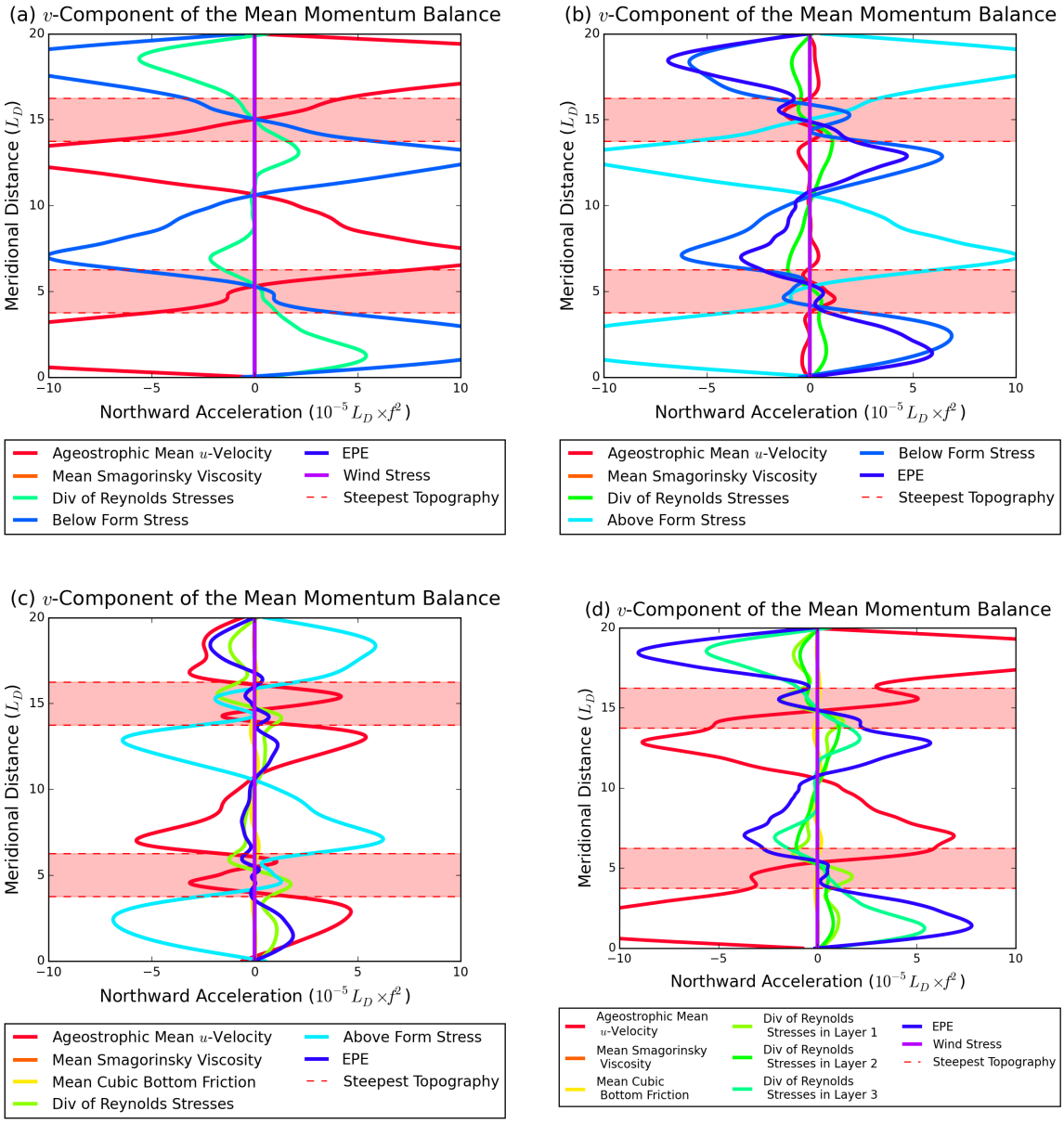


Figure 4.2.6: Meridional Momentum Balance in (a) the upper layer, (b) the middle layer (c) the lower layer and (d) the entire water column of a doubly re-entrant domain with zonal ridge and varying zero-mean wind. Red bands show regions of steepest topography.

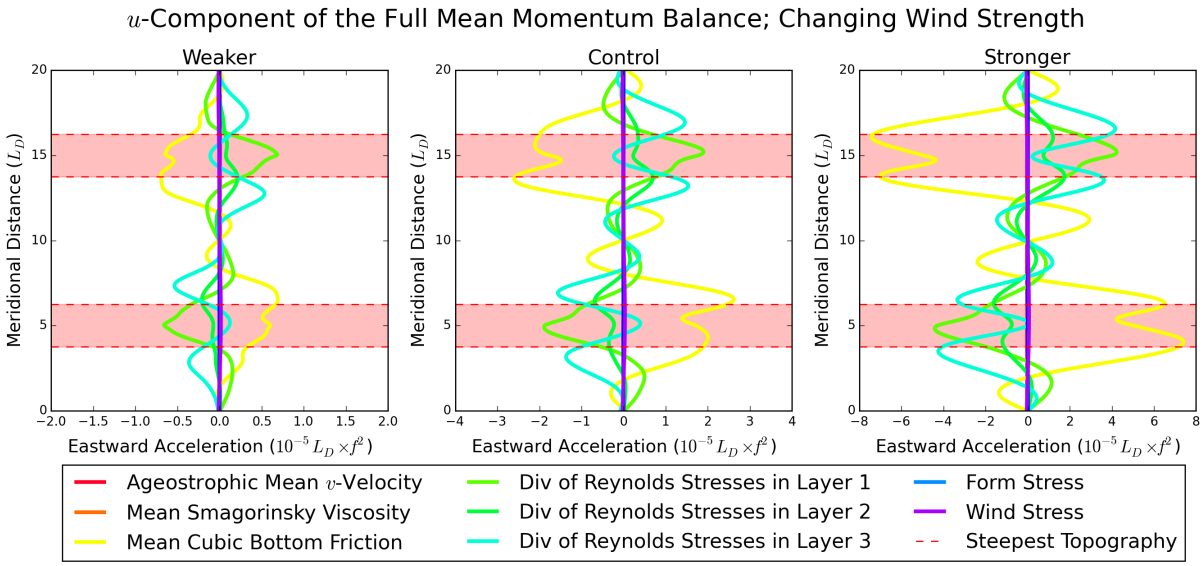


Figure 4.2.7: Depth integrated zonal momentum balance for three wind stress with magnitudes a factor of 2 different from one and another. Note that the x-axis is also scaled to allow the comparative magnitudes of the stresses to be compared. Red bands show regions of steepest topography. The bottom friction is almost 4 times stronger in the right-hand frame and 4 times weaker in the left-hand frame than in the control case despite the winds only changing by a factor of two.

bottom of the layer. Overall the eddy stresses simply balance anomalous ageostrophic components and are likely representing the effect of baroclinic instabilities. These are the results obtained using control parameters. Now lets explore parameter space to see how this affects the eddy stresses and hence the along-topography flow.

Firstly, let us tweak the wind stress. Changing parameters such as the frequency a vortex is spawned, their mean duration or their mean size are all either insignificant or equivalent to changing the magnitude of the overall wind stress. Hence, we will focus solely on the strength of the wind stress. Taking the control case that we have just discussed we generate two more models with half the wind stress and double the wind stress. A comparison of the resulting zonal momentum balances are shown in Figure 4.2.7 along with the control case. One might expect that by doubling the wind stress you would double the resulting stresses in the momentum balance. However, Figure 4.2.7 shows that bottom friction, and hence the Reynolds stresses that are balancing it are almost four times larger. This is similarly shown in the meridional momentum balances, Figure 4.2.8.

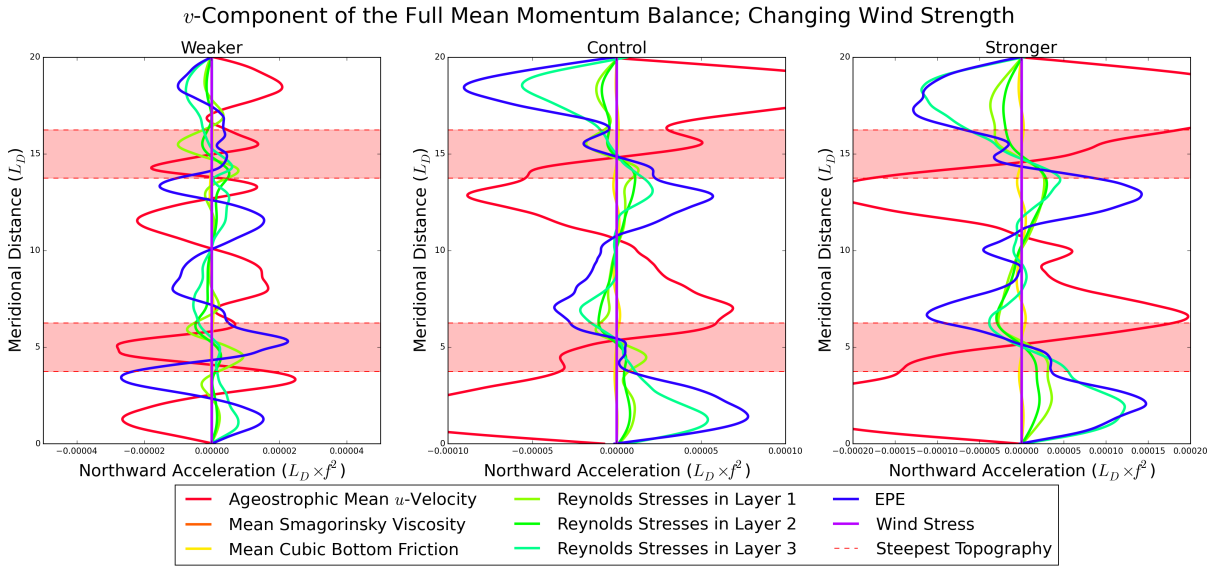


Figure 4.2.8: Depth integrated meridional momentum balance for three wind stress with magnitudes a factor of 2 different from one and another. Note that the x-axis is also scaled to allow the comparative magnitudes of the stresses to be compared. Red bands show regions of steepest topography.

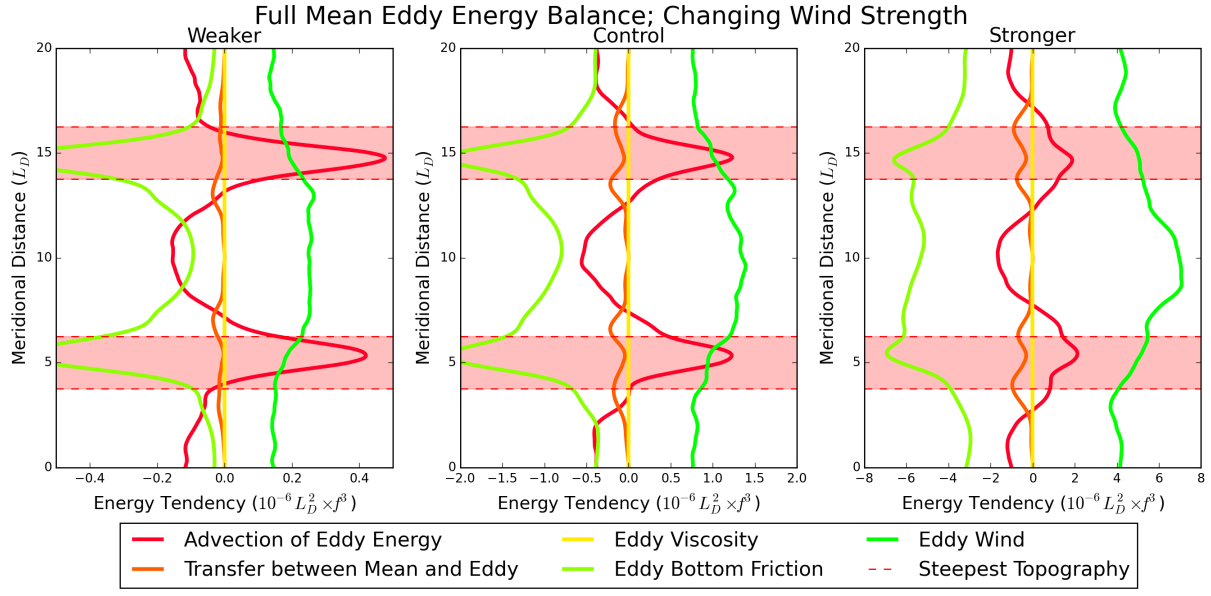


Figure 4.2.9: Depth integrated eddy energy balance for three wind stress with magnitudes a factor of 2 different from one and another. Note that the x-axis is also scaled to allow the comparative magnitudes of the stresses to be compared. Red bands show regions of steepest topography. The plots show that in all three configurations energy is introduced by the wind over the entire domain, it is then advected onto the steepest parts of the slope where it is mostly dissipated by the bottom friction. However, the rest is transformed into mean energy. The magnitude at which is happens changes by a factor of 4 for a factor of 2 change in wind strength.

To explain this look at the balance of terms in Equation (3.2.14), here we call

$$\boldsymbol{\nabla}_\rho \left[\langle h_n \rangle \, \overline{(\rho_n K_n + m_n)\, \boldsymbol{u}_n} \right] - \boldsymbol{\nabla}_\rho \left[\langle h_n \rangle \left(\rho_n \frac{1}{2} \left| \overline{\boldsymbol{u}}_n \right|^2 + \langle m_n \rangle \right) \overline{\boldsymbol{u}}_n \right]$$

the "eddy advection" and

$$- \left\langle \frac{\partial}{\partial t} \left(\eta^{\#}_{n+\frac{1}{2}} \right) m^{\#}_{n+1} \right\rangle \qquad \text{and} \qquad \left\langle \frac{\partial}{\partial t} \left(\eta^{\#}_{n-\frac{1}{2}} \right) m^{\#}_{n} \right\rangle$$

the "energy transfer between layers". Finally,

$$\overline{\boldsymbol{u}}_n \cdot (\boldsymbol{\nabla}_3 \cdot \boldsymbol{E})$$

is the "transfer of energy between the eddy and mean flow". The depth-integrated eddy energy in this balance, decomposed in this way, is shown in Figure 4.2.9. Here it is clear to see that much of the eddy energy introduced by the wind is removed by the bottom friction. However, the energy that is not removed is transferred into mean energy. The key is that, since the energy input from the wind,

$$\boldsymbol{\tau} \cdot \boldsymbol{u}_N,$$

and doubling the wind increases the velocity in the upper layer by about the same, doubling the wind increases energy by almost a factor of four. Hence, there is almost four times as much more eddy energy available for double wind, since the energy is injected into the eddy field. This is therefore tantalising evidence for how the eddy energy effects the strength of the eddy stresses.

An obvious contributor to generating an along-topography flow is the topography itself. There are two easy ways of changing the parameters of the ridge; either by raising or lowering the height of the ridge or by narrowing or widening it. The obvious effect of lowering the height of the ridge is that it would reduce the "cold doming" effect and hence a weaker along-topography flow would occur and vice versa for the higher ridge.

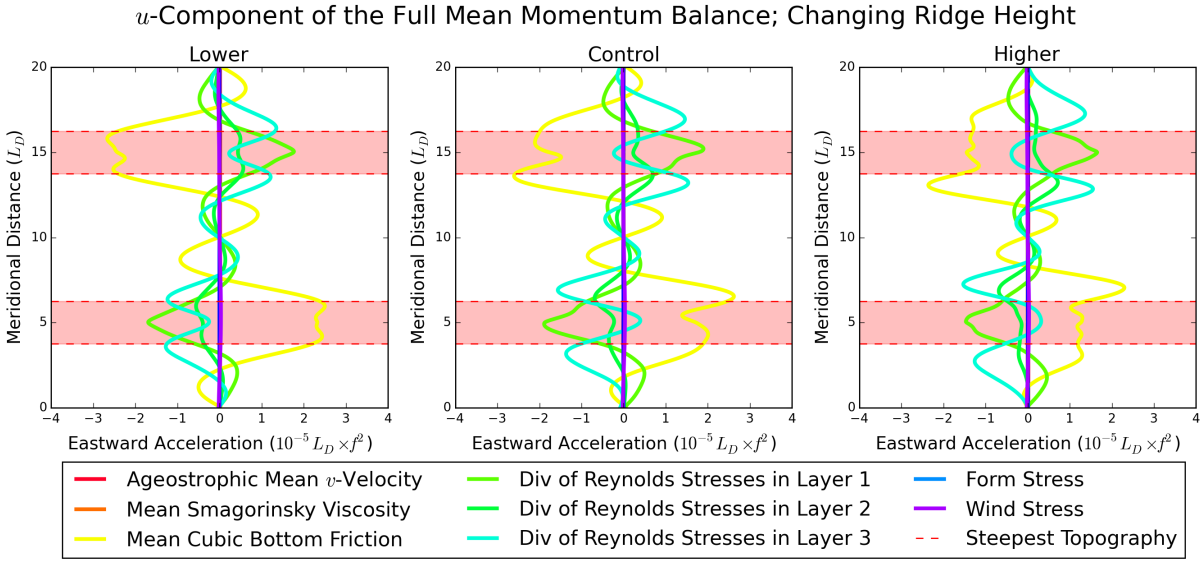


Figure 4.2.10: Depth integrated zonal momentum balance for three ridge heights: 1/8, 1/4 and 3/8 the mean ocean depth. Red bands show regions of steepest topography. Note that the stresses and bottome friction are almost identical for each frame.

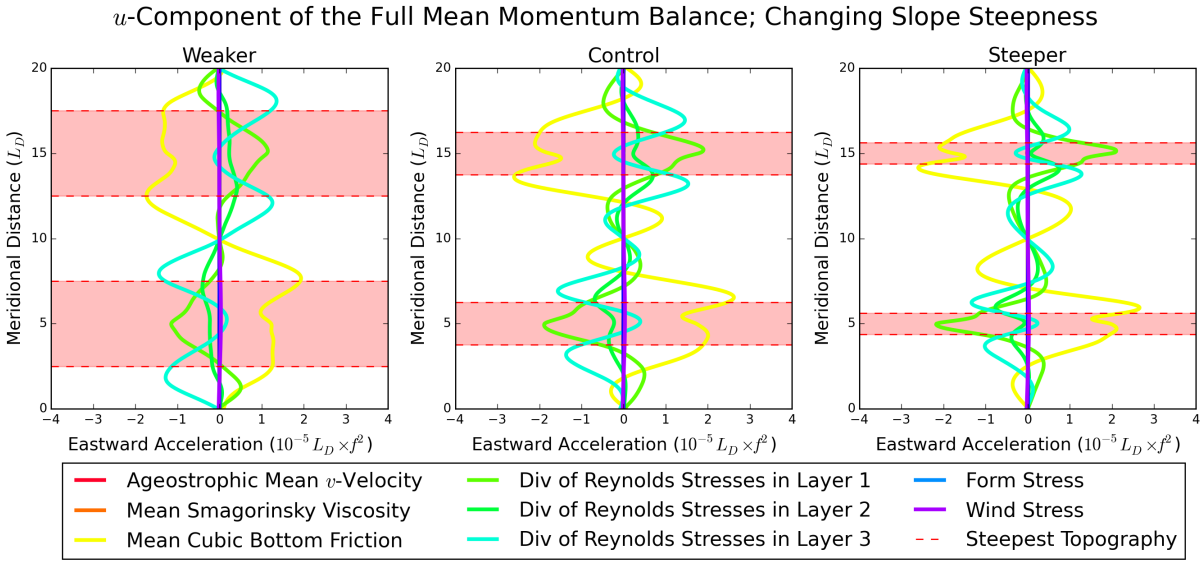


Figure 4.2.11: Depth integrated zonal momentum balance for three ridge widths: The slopes of the ridges span approximately 1/24, 1/4 and 1/8 of the domain respectively. Red bands show regions of steepest topography. The eddy stresses and bottom friction are tighter over the slope when the ridge is narrower but more spread-out when the ridge wider. However, there magnitude remain roughly the same indicating similar energy in the eddy fields.

However, this is not the case; Figure 4.2.10 demonstrates that the force from the bottom friction is roughly identical in all three models, indicating that the along-topography flow is of roughly equal magnitude in all of them. This can be understood in terms of the available driving power of the eddies, because the wind forcing is identical for all three models, the eddies fields will have a similar amount of energy and hence the eddy stresses in Figure 4.2.10 are almost identical. But, it is a different story when we narrow or widen the ridge (Figure 4.2.11); here the eddy stresses show much more dependence on the shape of the topography. This is because the area of topography available for the eddies to drive a flow over is smaller for the narrow ridge and larger for the wider ridge. However, because again the eddy fields are have the similar energy available, the eddies are only contributing a similar amount of stress; on the narrower ridge the stresses are even smaller as the eddies drive a certain amount of recirculation over the less steep topography. Overall, whilst the along-topography flow must depend on the topographic slope, the characteristics of the eddy field clearly also play a role.

4.3 Eddy-Mean Interaction Bounds

Recall that it is possible to bound the Eliassen-Palm flux tensor with the eddy energy, Equation (3.2.7), rewritten here as

$$\left\| \begin{array}{ccc} -M+K+P & N & 0 \\ N & M+K+P & 0 \\ R & S & 0 \end{array} \right\| \leq 2\,(K+P) \equiv 2E. \tag{4.3.1}$$

It turns out that the strictness of this bound is a strong determining factor for how the models behave in the parameter space described in Section 4.2. To make this discussion a little easier, we will use the fact that $(-M+K+P)^2+(M+K+P)^2 = 2M^2+2(K+P)^2$ to

decompose this bound into three more manageable parts. Firstly, the Reynolds Stresses,

$$\left\| \begin{array}{ccc} -M & N & 0 \\ N & M & 0 \\ 0 & 0 & 0 \end{array} \right\| \leq \sqrt{2}K; \tag{4.3.2}$$

secondly, the Form Stresses,

$$\left\| \begin{array}{ccc} 0 & 0 & 0 \\ 0 & 0 & 0 \\ R & S & 0 \end{array} \right\| \leq 2\sqrt{KP}, \tag{4.3.3}$$

at least in the geostrophic limit; just leaving the eddy energy

$$\left\| \begin{array}{ccc} K+P & 0 & 0 \\ 0 & K+P & 0 \\ 0 & 0 & 0 \end{array} \right\| = \sqrt{2}(K+P), \tag{4.3.4}$$

so that the norm of the full tensor is bound by,

$$\left\| \begin{array}{ccc} -M+K+P & N & 0 \\ N & M+K+P & 0 \\ R & S & 0 \end{array} \right\| \leq \begin{array}{c} \sqrt{2(K+P)^2+4KP+2K^2} \\ \leq 2(K+P). \end{array} \tag{4.3.5}$$

4.3.1 Reynolds Stress Bound

Let us begin by discussing the Reynolds stresses. The bounds Equation (4.3.2) for the control case are shown in Figure 4.3.1. The uppermost layer has a large amount of eddy kinetic energy. Around three times as much as is available in the lower layer, hence the bound on the Reynolds stresses in the uppermost layer is the least interesting. Because of this, and the problems generated in the upper most layer by the rigid lid approximation outlined in Section 4.2, we will ignore the uppermost layer and only discuss the bottom

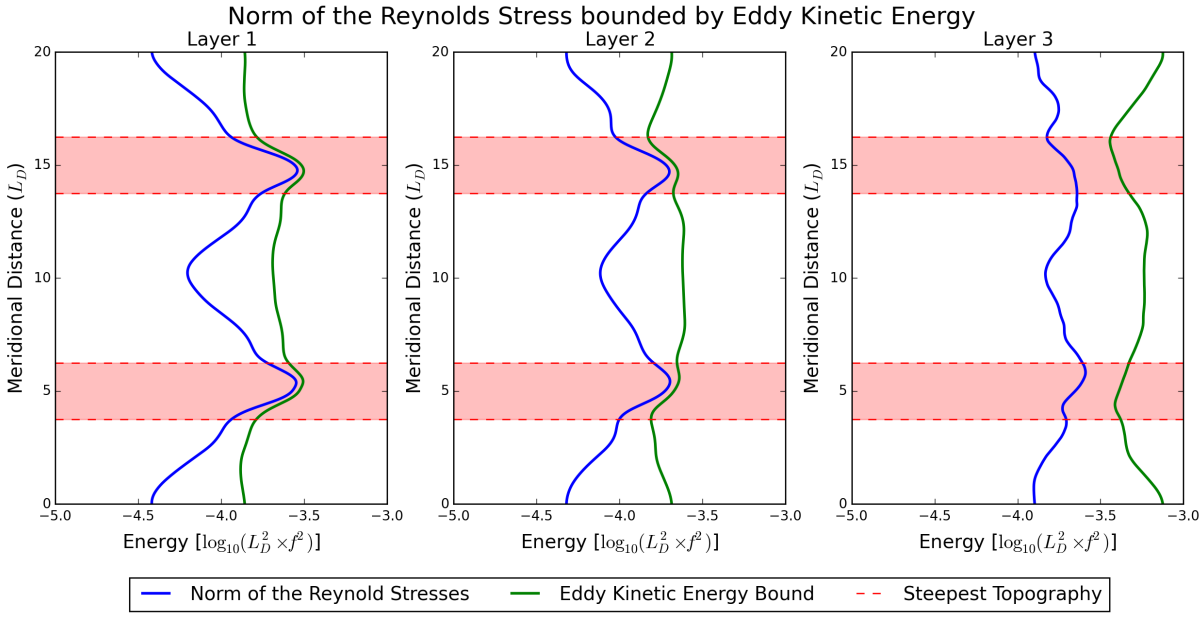


Figure 4.3.1: The norm of the Reynolds stresses and the kinetic energy bound for each layer of the control case. Red bands show regions of steepest topography.

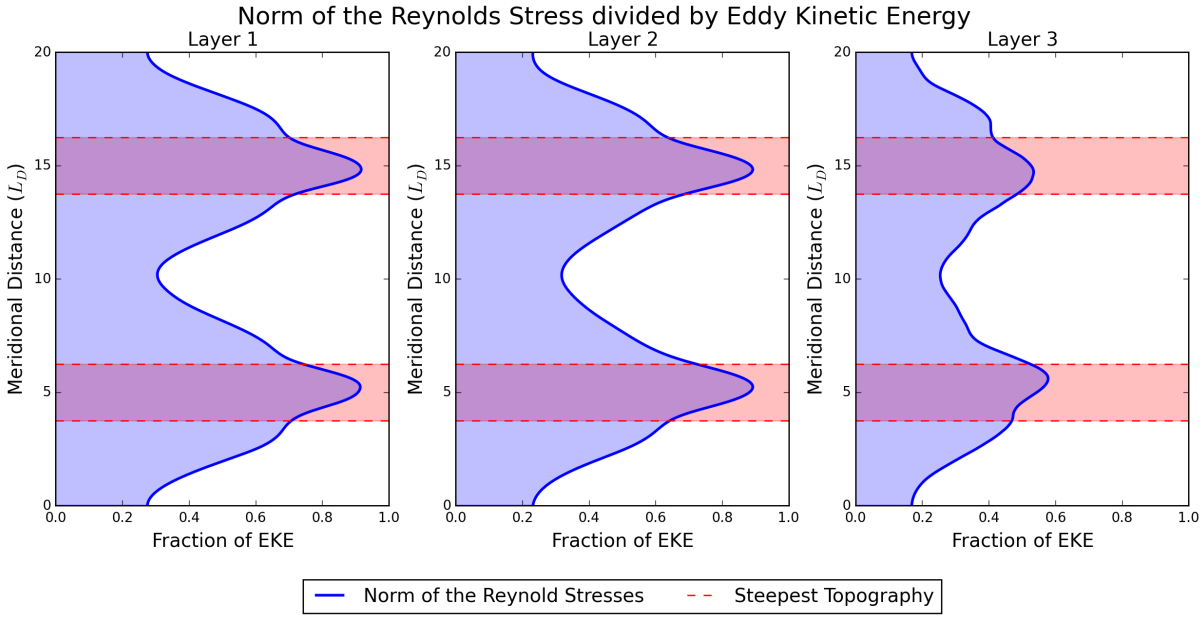


Figure 4.3.2: The ratio between the Reynolds stresses and the kinetic energy bound for each layer of the control case. Red bands show regions of steepest topography.

two layers. As demonstrated in Section 4.2, the Reynolds stresses attempt to push the flow along the topography and are balanced by the bottom friction. As expected, the Reynolds stresses are strongest over the steepest topography. However, this also takes the norm of the Reynolds stresses closer to their eddy kinetic energy bound (Figure 4.3.2); a situation which is critical for explaining some of the momentum balances in Section 4.2.

Firstly, when we examine what happens when we change the magnitude of the wind stress. We discussed in Section 4.2 how an increase of factor two in the magnitude of the wind stress increases the eddy stresses by a factor of four. Figure 4.3.3 shows the magnitude of the Reynolds stesses and the eddy kinetic energy for our three different wind strengths. Note that the energy does bound the stresses, and more strongly over the topography. This is shown more clearly in Figure 4.3.4 which plots the eddy anisotropy,

$$\lambda_m = \frac{\sqrt{M^2 + N^2}}{K}, \tag{4.3.6}$$

the magnitude of the Reynolds stress as a fraction of the eddy kinetic energy. This shows a persistent structure for the three wind stresses ranging between $0.3 \lesssim \lambda_m \lesssim 0.9$, with the Reynolds stress most constrained over the steepest topography ($\lambda_m \sim 0.9$).

In contrast, when systems with similar eddy energy but different topography are compared the Reynolds stresses give noticeably different eddy anisotropies, λ_m. When we change the depth of the topography, Figure 4.3.5 shows that for higher topography, the norm of the Reynolds stresses really pushes against the kinetic energy bound, whilst for shallower topography it is much less constrained by the bound. This is made even more clear by taking a look at the eddy anisotropies for the Reynolds stresses in Figure 4.3.6, we can see that for the higher topography the anisotropy is much more close to 1 for much more of the domain than it is in the control case, whilst for the shallower topography, the anisotropy does not go above 0.6. It is also worth noting that minimum anisotropy is around $0.2 \leq \lambda_m \leq 0.3$ in all three of the models whenever the topography is flat, i.e. at the top and bottom of the ridge. This indicates that the anisotropies are in some way dependent on the topographic slope. By making the ridge slope narrower or wider we

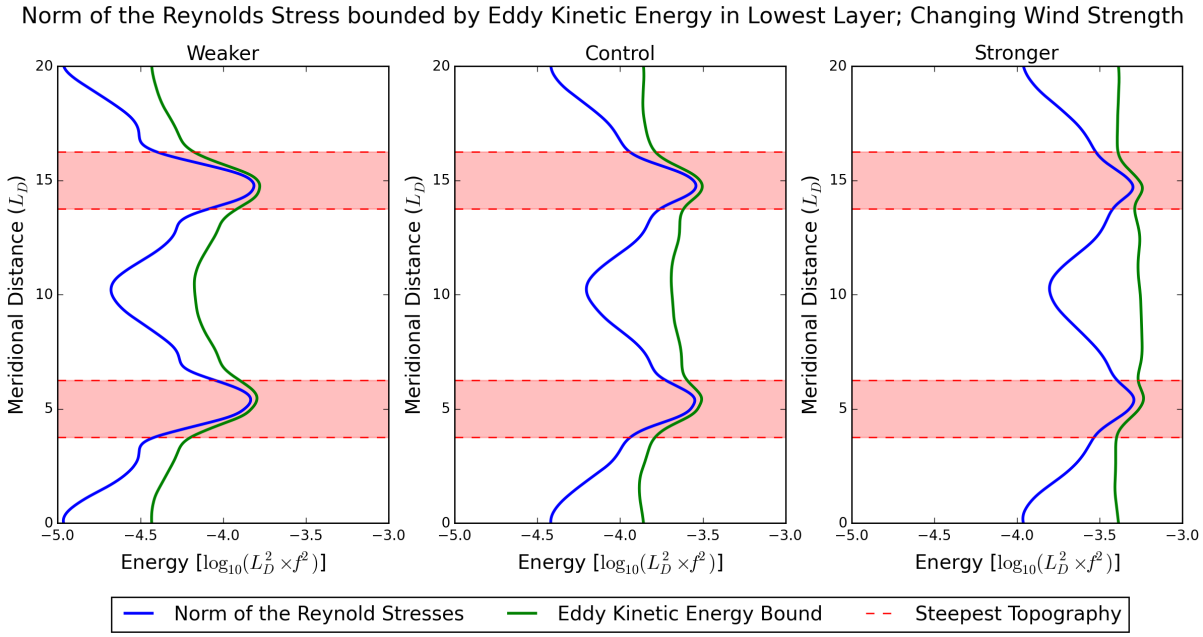


Figure 4.3.3: The norm of the Reynolds stresses and the kinetic energy bound in the lowest layer for the control case, 2× and 0.5× wind strength. Red bands show regions of steepest topography.

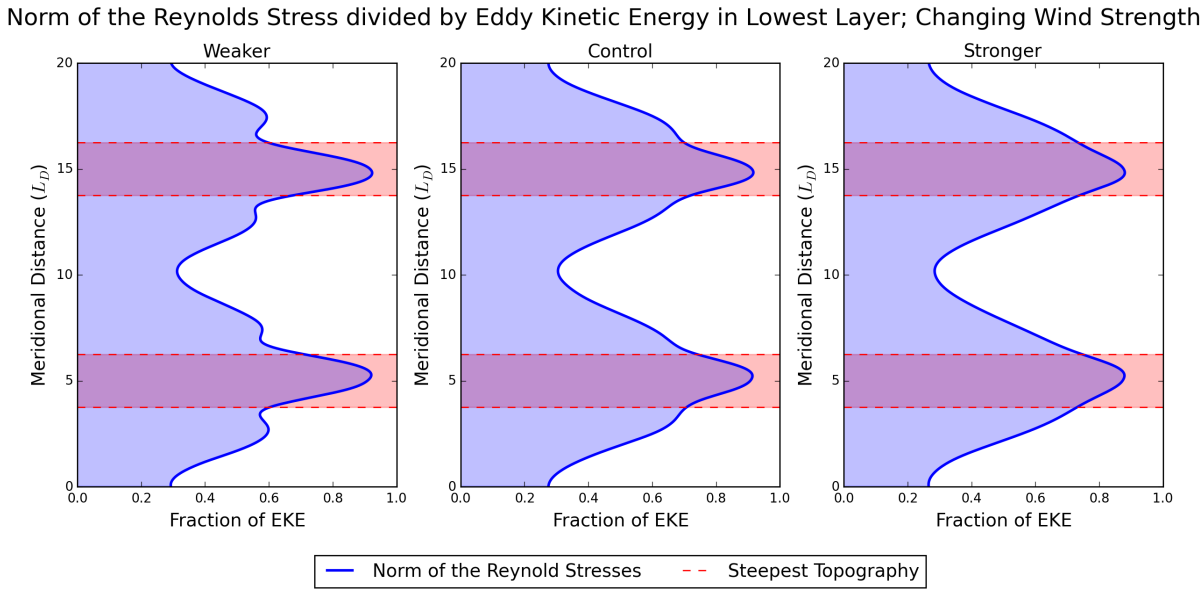


Figure 4.3.4: The eddy anisotropy, the ratio between the Reynolds stresses and the kinetic energy bound, in the lowest layer for the control case, 2× and 0.5× wind strength. Red bands show regions of steepest topography. The anisotropies of the three configurations are re-markedly similar.

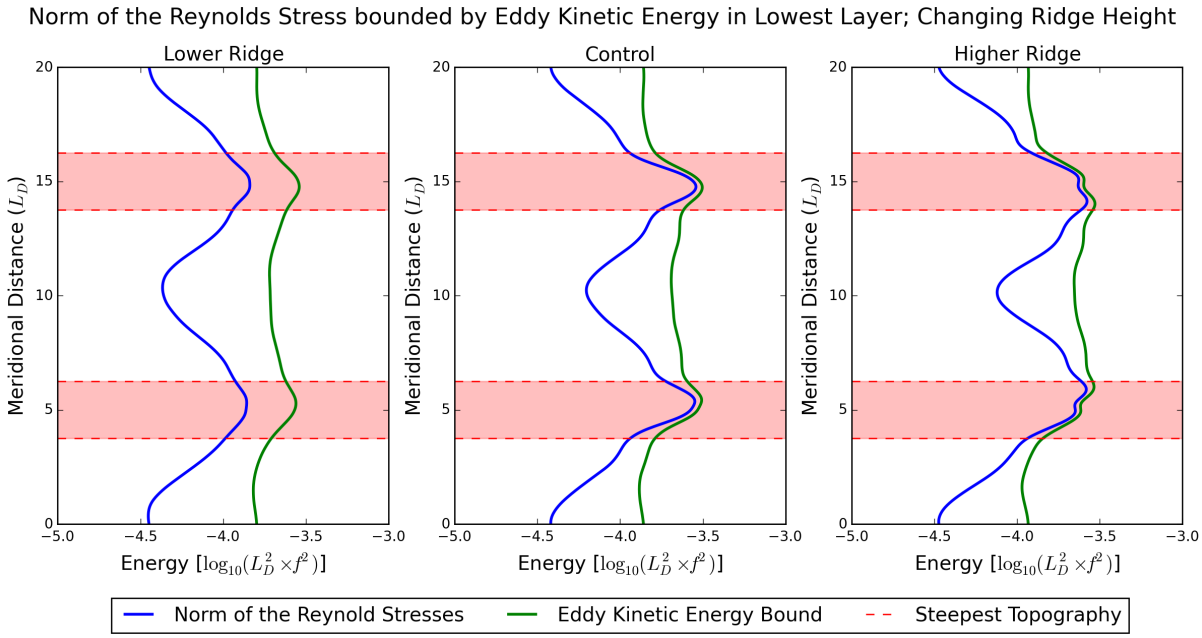


Figure 4.3.5: The norm of the Reynolds stress and the kinetic energy bound in the lowest layer for the lower ridge height, control case and higher ridge height. Red bands show regions of steepest topography. The norm of the Reynolds stress is much closer to the bound when the topography is more extreme than less extreme.

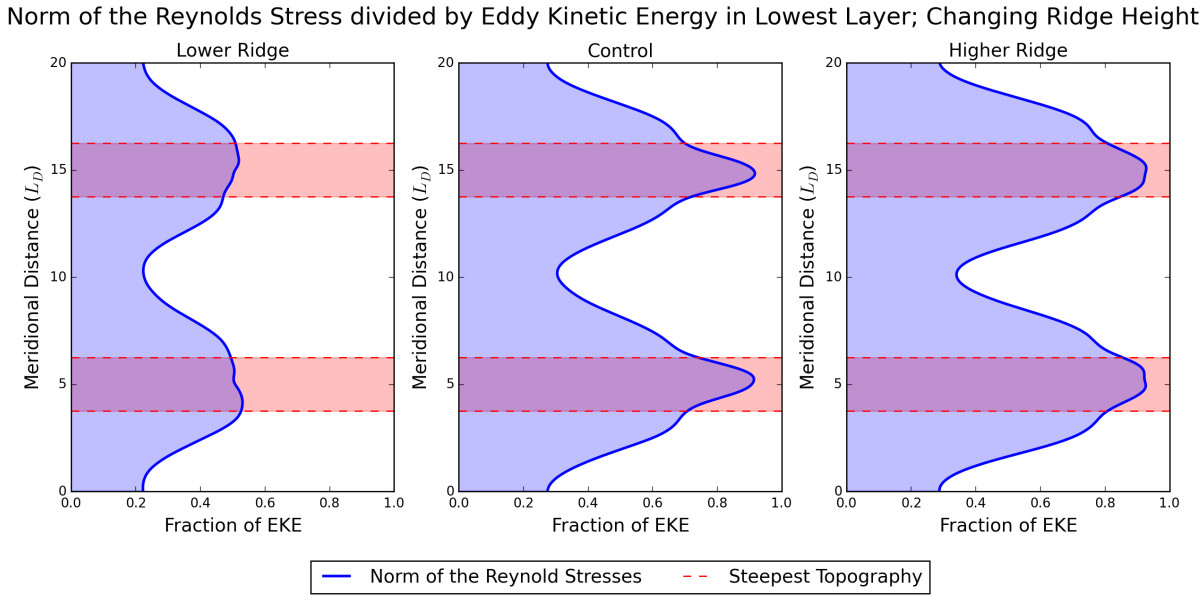


Figure 4.3.6: The eddy anisotropy, the ratio between the Reynolds stresses and the kinetic energy bound, in the lowest layer for the lower ridge height, control case and higher ridge height. Red bands show regions of steepest topography. When the topography is more extreme much more of the eddy anisotropy is closer to 1 whereas when the topography is less extreme the anisotropy is always less than 0.6.

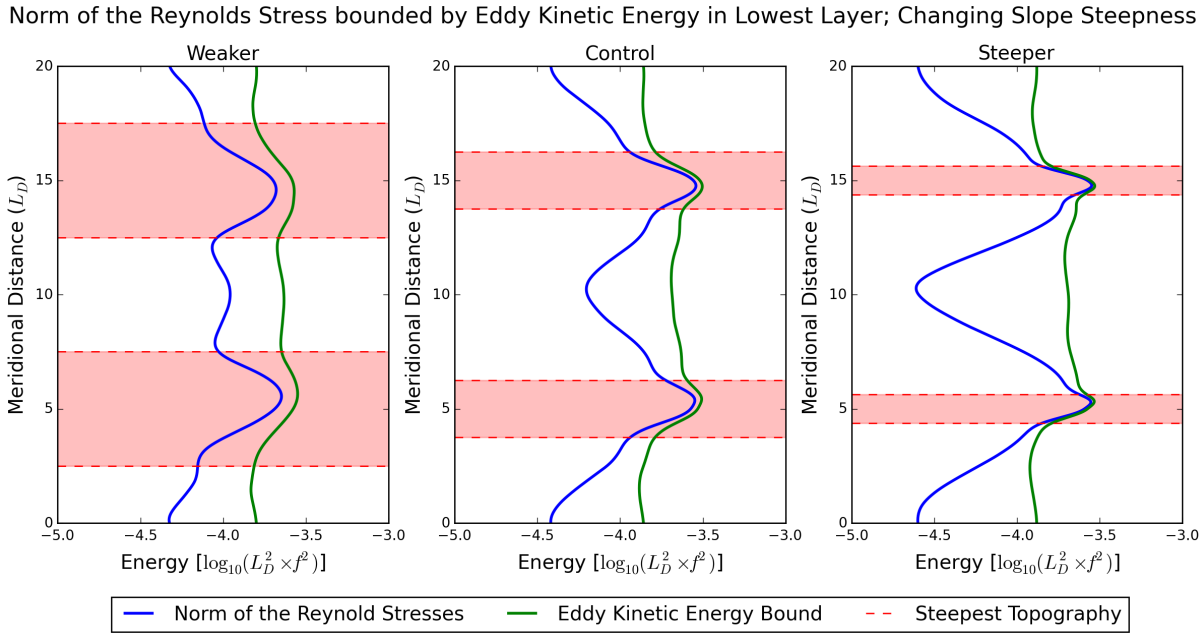


Figure 4.3.7: The norm of the Reynolds stress and the kinetic energy bound in the lowest layer for the shallower topographic slope, control case and steeper topographic slope. Red bands show regions of steepest topography. The norm of the Reynolds stress is much closer to the bound when the slope is more extreme than less extreme.

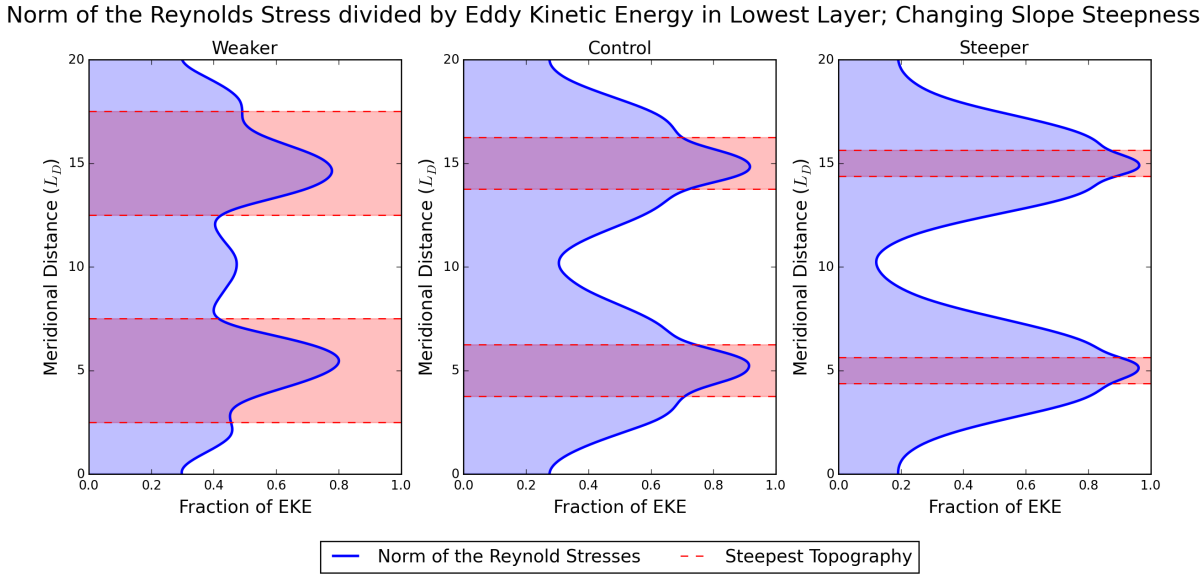


Figure 4.3.8: The eddy anisotropy, the ratio between the Reynolds stresses and the kinetic energy bound, in the lowest layer for the shallower topographic slope, control case and steeper topographic slope. Red bands show regions of steepest topography. When the slope is more extreme the maximum eddy anisotropy is closer to 1 whereas when the topography is less extreme the anisotropy is less than 0.8.

gain a similar result, shown in Figures 4.3.7 and 4.3.8, The model where the ridge has a wider slope has an anisotropy which is much less constrained than when the slope is steeper.

In summary, the bound on the Reynolds stresses can be highly constraining. This is predominantly when the eddy kinetic energy is limiting and when topographic slope is the strongest. This constraint has the effect of limiting the along topography stress that generates the along-topography flow, demonstrating how the along-topography flow is limited by the available eddy kinetic energy.

4.3.2 Form Stress Bound

To bound the form stresses recall that the meridional component of the form stress is large in comparison to the zonal component. Hence, we shall diagnose each component of the form stress individually. Using the Cauchy-Schwartz Inequality we have

$$\frac{1}{\rho_N^2}\left\langle \eta^{\#}_{n-\frac{1}{2}}\frac{\partial m^{\#}_n}{\partial x}\right\rangle^2 \sim f^2\left\langle \eta^{\#}_{n-\frac{1}{2}}v^{\#}_n\right\rangle^2 \leq f^2\left\langle \eta^{\#}_{n-\frac{1}{2}}\eta^{\#}_{n-\frac{1}{2}}\right\rangle\left\langle v^{\#}_n v^{\#}_n\right\rangle \tag{4.3.7}$$

and

$$\frac{1}{\rho_N^2}\left\langle \eta^{\#}_{n-\frac{1}{2}}\frac{\partial m^{\#}_n}{\partial y}\right\rangle^2 \sim f^2\left\langle \eta^{\#}_{n-\frac{1}{2}}u^{\#}_n\right\rangle^2 \leq f^2\left\langle \eta^{\#}_{n-\frac{1}{2}}\eta^{\#}_{n-\frac{1}{2}}\right\rangle\left\langle u^{\#}_n u^{\#}_n\right\rangle \tag{4.3.8}$$

for the zonal and meridional components respectively. By combining the two components we retain the original form stress bound used to give Equation (3.2.7),

$$\left\| \begin{array}{cc} R & S \end{array} \right\| \lesssim \frac{2f}{\sqrt{g_{n-\frac{1}{2}}}}\sqrt{KP}. \tag{4.3.9}$$

However, we can interpret the zonal form stresses as the transfer of along-topography momentum between layers, whilst the meridional form stress could be interpreted as the baroclinic instability generated by the sloping interfaces between the layers, or isopycnals, and hence it makes sense to discuss the components separately.

The first thing to note is the differences between the zonal form stress and meridional

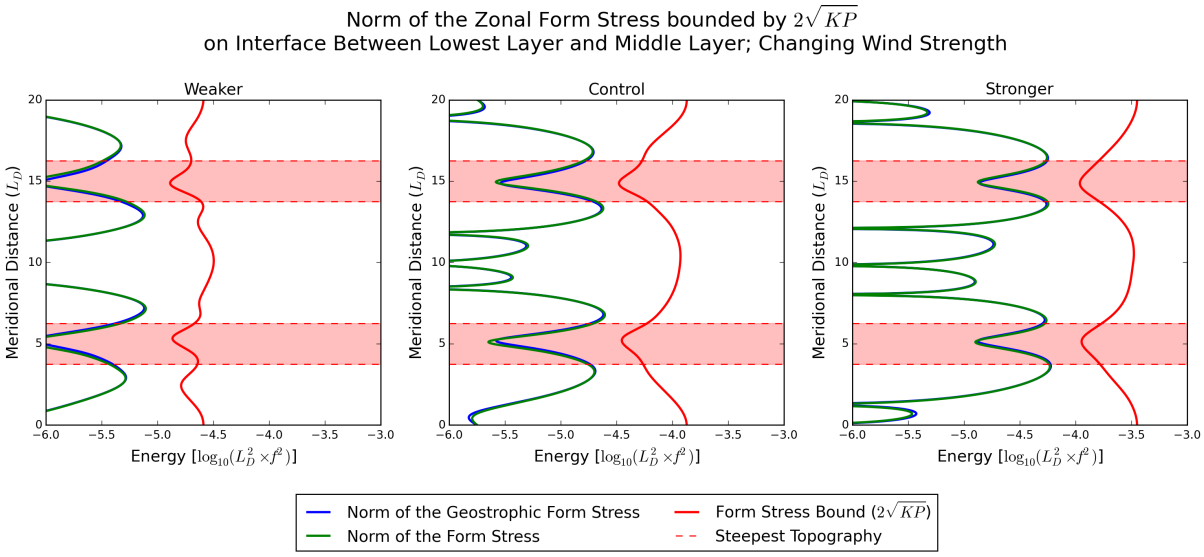


Figure 4.3.9: The magnitude of the zonal form stress and the potential energy bound for the interface between the lowest layer and middle for the control case, 2× and 0.5× wind strength. Red bands show regions of steepest topography.

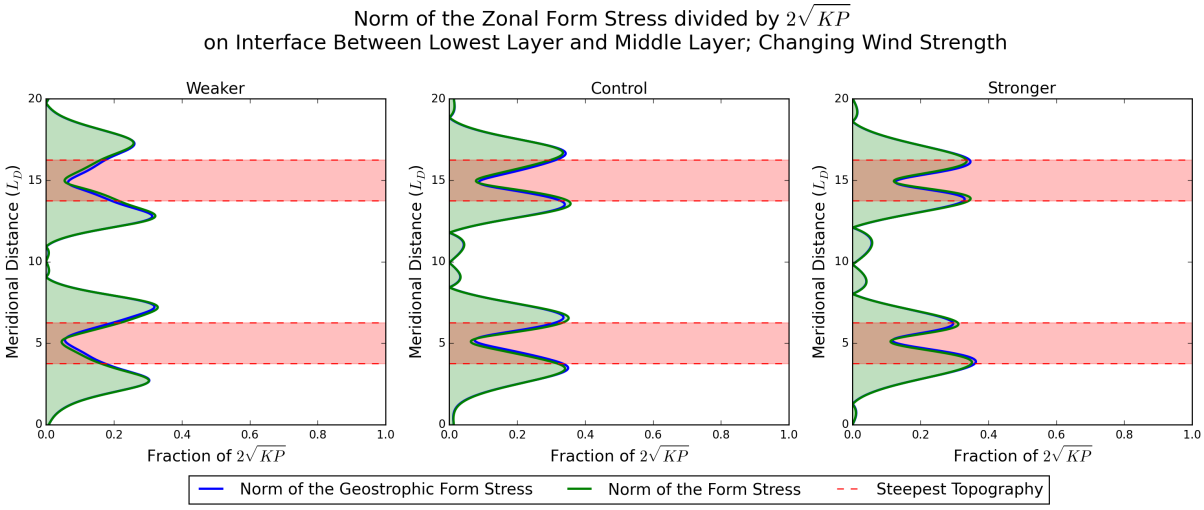


Figure 4.3.10: The ratio between the magnitude of the zonal form stress and the potential energy bound for the interface between the lowest layer and middle for the control case, 2× and 0.5× wind strength. Red bands show regions of steepest topography.

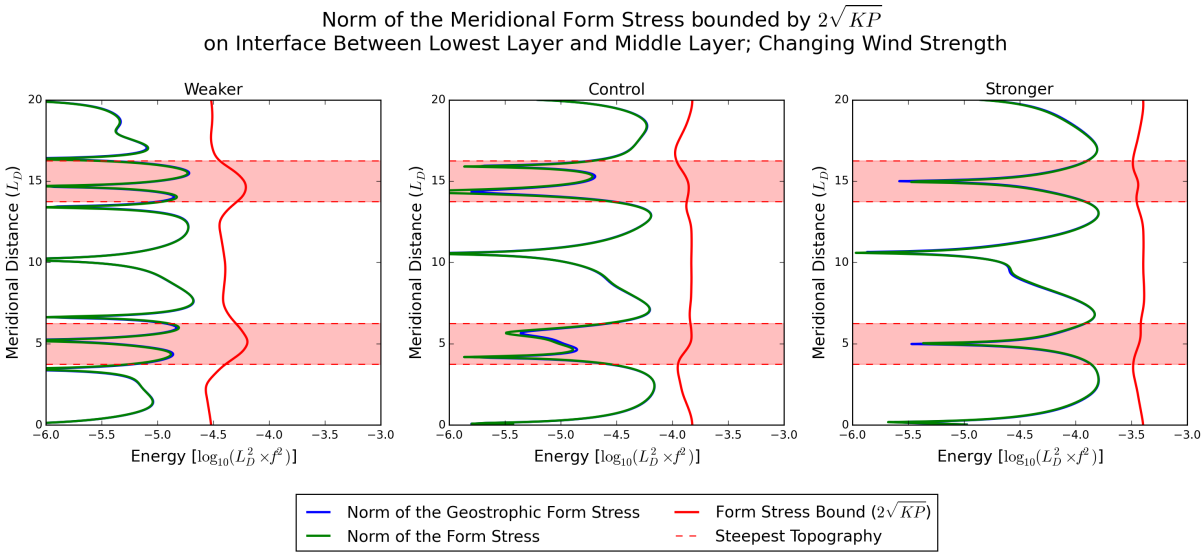


Figure 4.3.11: The magnitude of the meridional form stress and the potential energy bound for the interface between the lowest layer and middle for the control case, 2× and 0.5× wind strength. Red bands show regions of steepest topography.

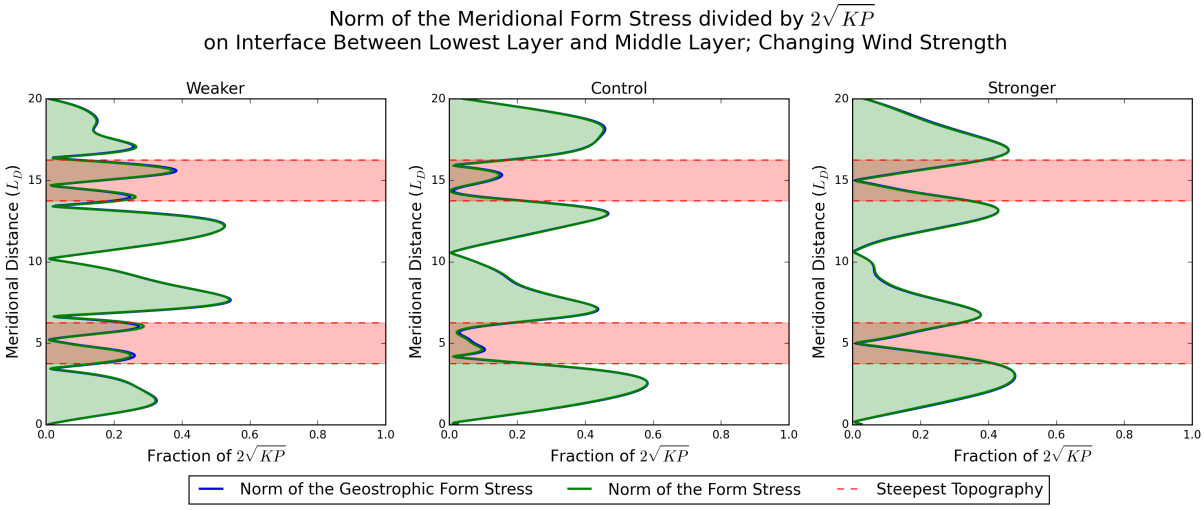


Figure 4.3.12: The ratio between the magnitude of the meridional form stress and the potential energy bound for the interface between the lowest layer and middle for the control case, 2× and 0.5× wind strength. Red bands show regions of steepest topography.

form stress. Figure 4.3.9 shows that the zonal form stresses are largest above the topographic slopes for each of the three wind stress strength with a similar form in each one. The ratio shown in Figure 4.3.10 demonstrates that the zonal form stress is proportional to the bound given in Equation (4.3.7) under varying wind strength. Meanwhile, Figure 4.3.11 shows the meridional form stress is characterised by the changes of sign that occur fairly consistently at different points on the topography. Namely, at the point of steepest topography as well as at the top and the bottom of the ridge. However, in terms of the proportion of the meridional form stress to its bound given in Equation (4.3.8), Figure 4.3.12 the different wind stresses are vastly different.

In terms of the along-topography flow, the zonal component is the most interesting. As suggested earlier, it represents the transfer of the along-topography momentum between layers. Interestingly the transfer appears to take place, not at the steepest topography, but on the slope either side. The bound also dips at the points of steepest topography; however, by looking at the ratios between the form stresses and bound, Figure 4.3.10, it is clear that the bound is not the critical factor in the drop. It is instead likely that form stresses have this shape because the zonal momentum is generated in upper layer at these meridional positions by the Reynolds stress and hence is transferred directly downwards by the form stresses. Hence, as well as the being bounded by $2\sqrt{KP}$, the zonal form stress is more strongly determined by the momentum generated in the layers above, for example, by the Reynolds stresses in this case.

Manipulating the topography, however, appears to change the zonal form stress in the way one might expect. Both lowering the height of the ridge, Figure 4.3.13, and shallowing the topographic slope, Figure 4.3.14, reduces the kink that occurs at the point of steepest topography; meanwhile, the reverse strengthens it. Also the shallowing in Figure 4.3.14 spreads out the form stress across the slope with the steepening sharpens it.

Finally, it can also be seen that the geostrophic approximation that is made when deriving the bound for the form stress holds almost perfectly. In other words, and in

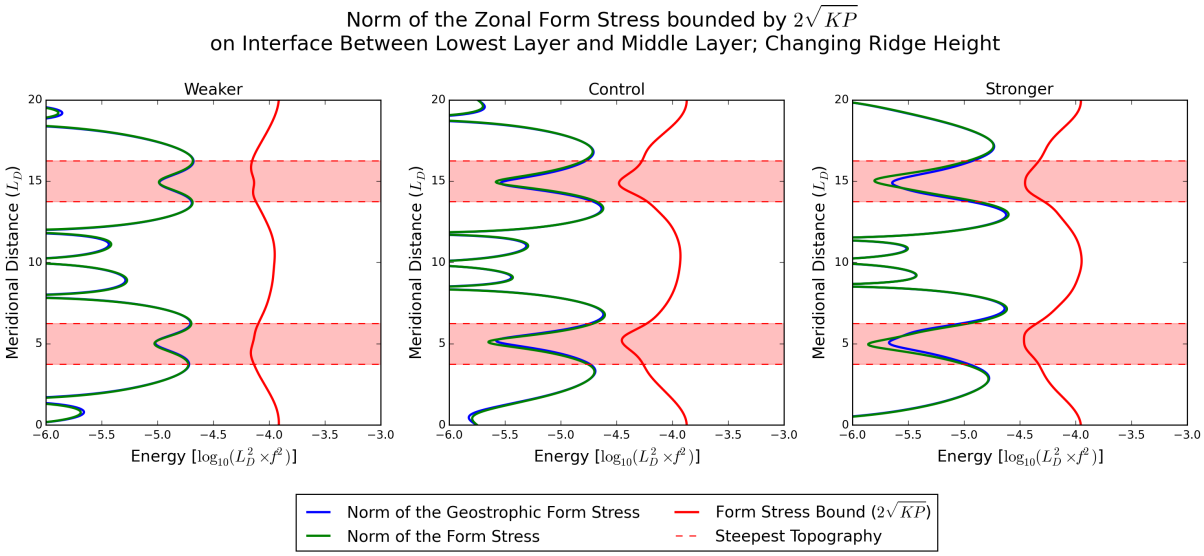


Figure 4.3.13: The magnitude of the meridional form stress and the potential energy bound for the interface between the lowest layer and middle for the control case, lower ridge height and higher ridge height. Red bands show regions of steepest topography.

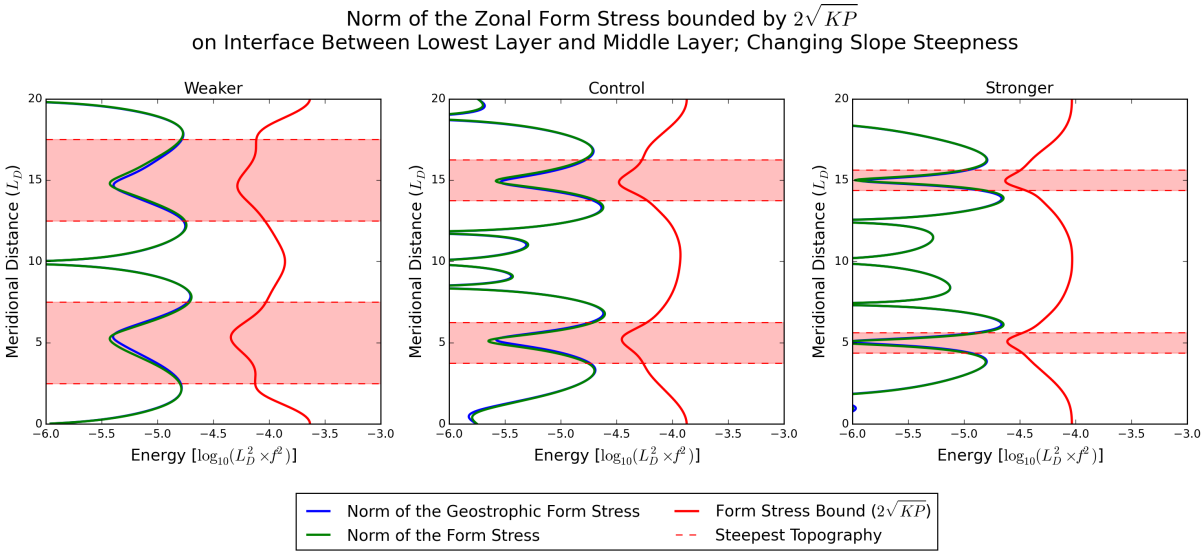


Figure 4.3.14: The magnitude of the meridional form stress and the potential energy bound for the interface between the lowest layer and middle for the control case and, shallower and steeper topographic slope. Red bands show regions of steepest topography.

contrast to the large scale flow, we have that

$$\frac{1}{\rho_n}\frac{\partial m_n^{\#}}{\partial x} \sim f v_n^{\#} \tag{4.3.10}$$

and

$$\frac{1}{\rho_n}\frac{\partial m_n^{\#}}{\partial y} \sim -f u_n^{\#} \tag{4.3.11}$$

and the eddy field is in geostrophic balance.

Overall, we have satisfied ourselves that the geostrophic approximation is appropriate in this scenario and hence that the form stress bound derived in Section 3.2 is valid. However, unlike the kinetic energy bound on the Reynolds stresses, the bound is much less constraining and the form stresses appear to be defined much more by where momentum is being generated and then they are able to transfer it to other layers. Our models also appear to exhibit large meridional form stresses, although this is likely due to the double-periodic domain, the ageostrophic mean flow that arises from it and the need to balance it.

4.4 PV Conservation and Comparison of Mean PVs

As discussed in Section 3.2.1, there are two different formulations that could be used to describe the mean field PV; the first being the thickness weighted average of the full PV,

$$\overline{q}_n = \frac{f + \frac{\partial \langle v \rangle_n}{\partial x} - \frac{\partial \langle u \rangle_n}{\partial y}}{\langle h_n \rangle},$$

and the other, the PV derived from the thickness weighted averaged momentum equations,

$$\mathring{q}_n = \frac{f + \frac{\partial \overline{v}_n}{\partial x} - \frac{\partial \overline{u}_n}{\partial y}}{\langle h_n \rangle}.$$

The pragmatic choice would be to use the second definition, $\mathring{q}$, since it is defined by the thickness weighted velocities, rather than the non-thickness weighted velocities, which are

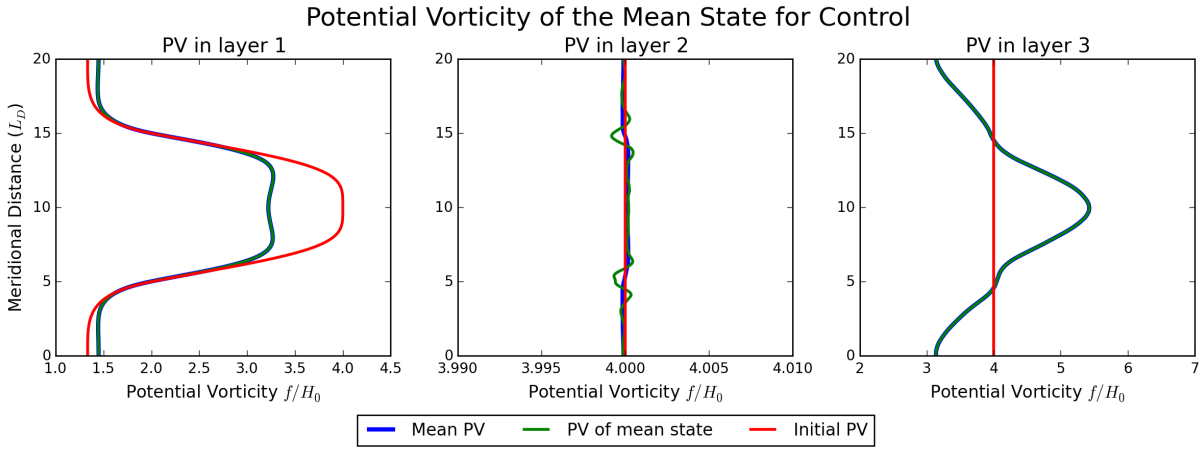


Figure 4.4.1: The mean PV and PV of the mean state in comparison to the initial PV in the control state.

the velocities we hope to represent in at a coarse resolution. As well as this, the eddy fluxes in the time-evolution equation for $\mathring{q}$ can be defined in terms of the Eliassen-Palm flux tensor. However, as discussed earlier, $\overline{q}_n$ cannot be discounted since its time-evolution equation gives an eddy flux which can be mathematically bounded. Hence, in this section we shall compare the two definitions of mean PV and examine how they are bounded.

Firstly, let us discuss how the mean PV looks in our model. Recall that the model is initialised from rest, hence the upper two layers initialise with uniform PV, whilst the lowest layer has PV,

$$q_1 = \frac{f}{h_1}.$$

Figure 4.4.1 shows the two definitions of the mean PV in contrast to the initial PV field. The figure shows that in the lowest layer, the PV field has become more homogenised, whilst in the upper most layer a PV gradient has been created, with the strongest PV over the ridge, and weakest in the trench. The middle layer is almost completely homogeneous. It can also be noted that the two definitions of PV basically agree. In fact, the difference between the two definitions, which can be seen in the PV for the second layer in Figure 4.4.1, is less than 1%.

Once again, varying the model parameters results in different mean PV fields. As one might expect, Figure 4.4.2 and Figure 4.4.3 show that stronger winds allow for greater

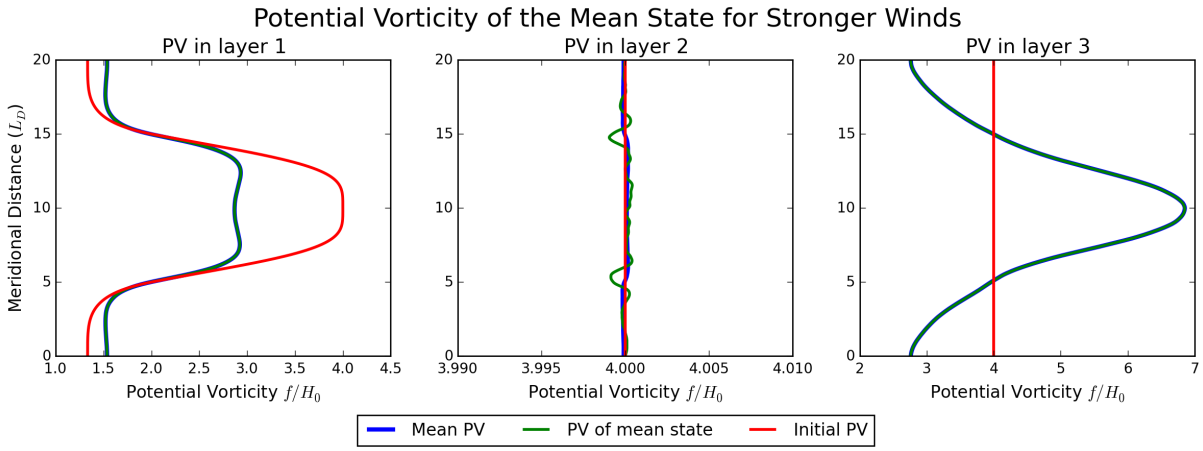


Figure 4.4.2: The mean PV and PV of the mean state in comparison to the initial PV for 2× stronger winds.

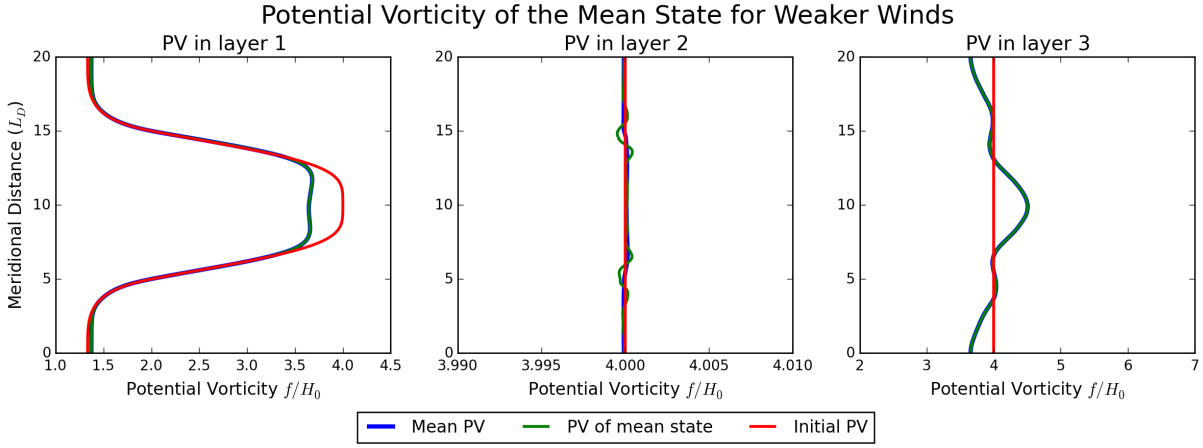


Figure 4.4.3: The mean PV and PV of the mean state in comparison to the initial PV for 2× weaker winds.

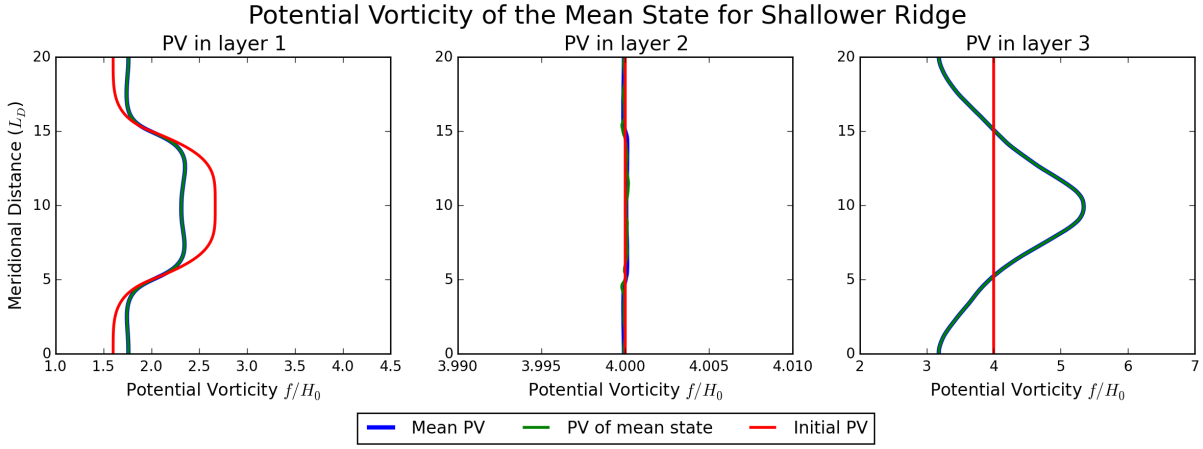


Figure 4.4.4: The mean PV and PV of the mean state in comparison to the initial PV for lower ridge height.

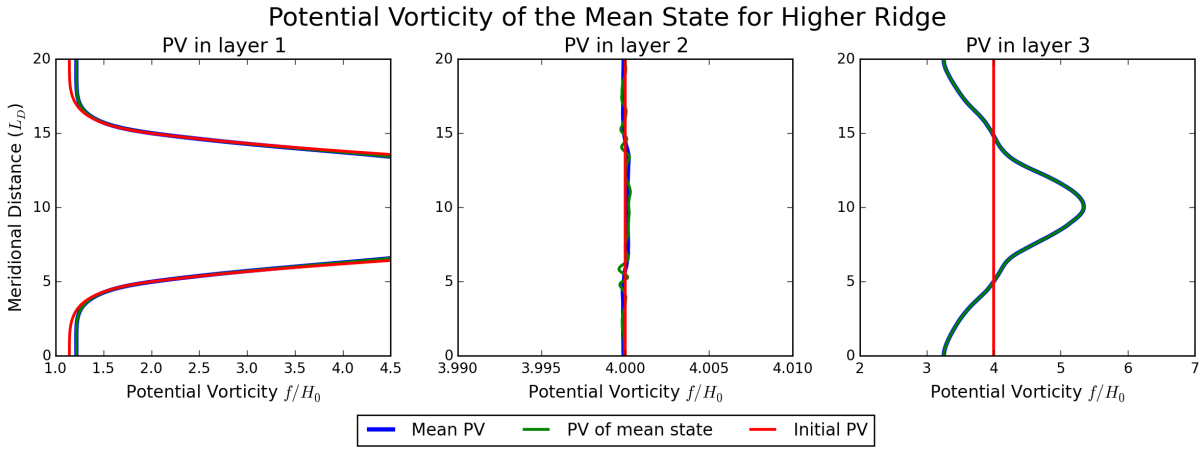


Figure 4.4.5: The mean PV and PV of the mean state in comparison to the initial PV for higher ridge height.

homogenisation in the lowest layer and a greater PV gradient in the upper layer, whilst weaker winds leads to a less homogenised lower layer, and smaller PV gradient in the upper layer. This could be understood as the result of there being more available eddy energy when the winds are stronger than when they are weaker. In contrast, Figure 4.4.4 and Figure 4.4.5 show that increasing or decreasing the height of the ridge has comparatively little effect on the PV gradient in the upper layer. Meanwhile, in the lowest layer, the initial PV gradient is homogenised roughly the same amount in each case and hence there is a much smaller proportional effect on the huge initial PV gradient than there is on the smaller one.

Focusing just on the PV of the thickness weighted averaged equations, $\mathring{q}$, we can discuss how its time-evolution equation is balanced in the steady state. Recall that we have Equation (3.2.9),

$$\frac{\mathring{D}\mathring{q}_n}{Dt} = -\langle h_n \rangle^{-1} \boldsymbol{\nabla} \cdot \mathring{\boldsymbol{F}} + \mathring{G},$$

where $\mathring{G}$ has been added to include all of the forcing and dissipation terms. Firstly, the left hand side is vanishingly small since $\mathring{q}_t \sim 0$ and $\overline{v}\mathring{q}_y \sim 0$ in each layer because of our long averaging window and $\overline{u}\mathring{q}_x = 0$ since we also average zonally. Hence, our PV eddy stresses must balance the forcing and dissipation term, $\mathring{G}$. However, by construction the wind stress is vanishingly small in the average, as is the viscosity, and hence layers 2 and

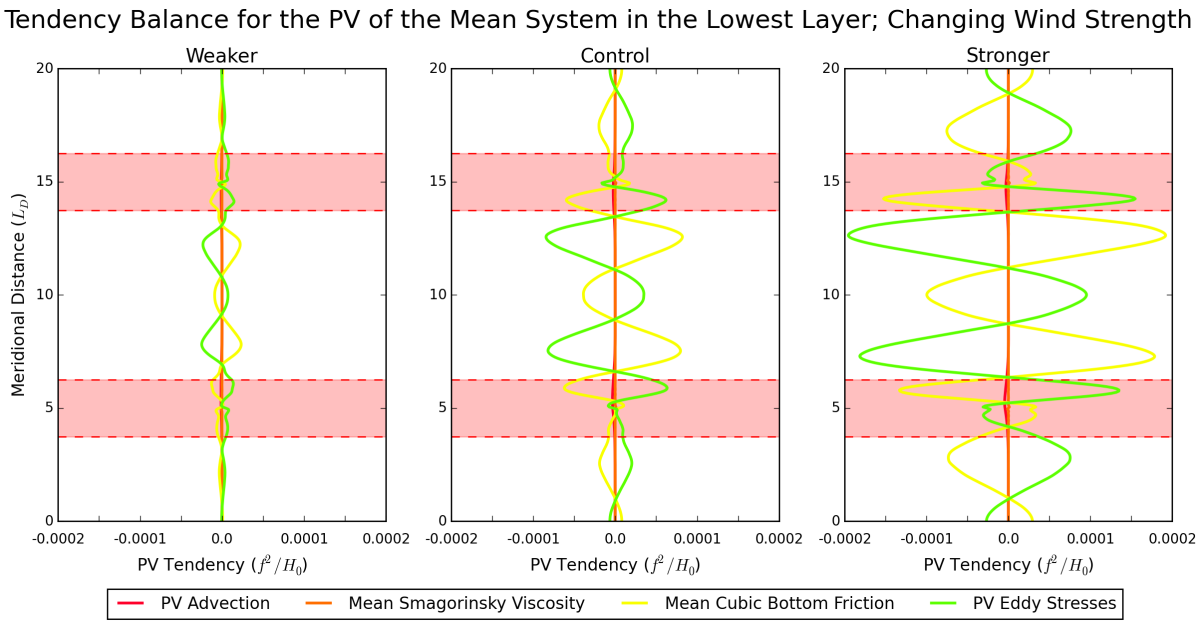


Figure 4.4.6: PV tendency balance in the lowest layer for the control and, 2× and 0.5× wind strength. The eddy stresses balance the bottom friction.

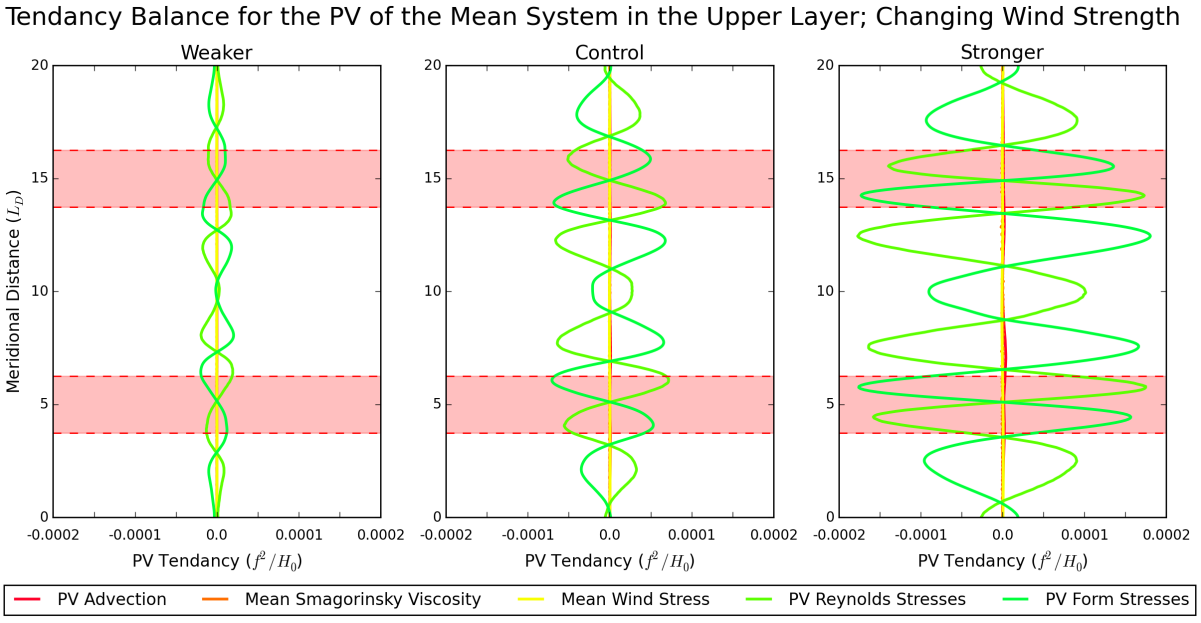


Figure 4.4.7: PV tendency balance in the uppermost layer for the control and, 2× and 0.5× wind strength. The eddy stresses balance to zero with the Reynolds component of the stress balancing the form stress component.

3 have no forcing or dissipation for the eddy stresses to balance. Meanwhile, in the lowest layer the eddy stresses must balance the bottom friction. In the PV equations this has become

$$\mathring{G} = \frac{\frac{\partial}{\partial x}\left(D_{\overline{v}_1}\right) - \frac{\partial}{\partial y}\left(D_{\overline{u}_1}\right)}{\langle h_1 \rangle} \tag{4.4.1}$$

where

$$D_{\overline{u}_1} = -r\frac{1}{|\boldsymbol{u}^*|^2}\left\langle |\boldsymbol{u}_1|^2 u_1 \right\rangle / \langle h_1 \rangle \qquad \text{and} \qquad D_{\overline{v}_1} = -r\frac{1}{|\boldsymbol{u}^*|^2}\left\langle |\boldsymbol{u}_1|^2 v_1 \right\rangle / \langle h_1 \rangle .$$

Of course, with zonal averaging, Equation (4.4.1) reduces to just $\mathring{G} = -\left(D_{\overline{u}_1}\right)_y / \langle h_1 \rangle$. Figure 4.4.6 demonstrates how the PV eddy stresses balance the bottom friction in the lowest layer for our three different strength winds. However, this balance isn't very informative, in the momentum balances from earlier, Figure 4.2.4 and Figure 4.2.6, we found that momentum is generated by the Reynolds stresses and transferred between layers and hence we were able to discuss how momentum generated throughout the water column is able to be balanced by the bottom friction. If, instead, we split the PV eddy stress, $\langle h_n \rangle^{-1} \boldsymbol{\nabla} \cdot \mathring{\boldsymbol{F}}$, into the curl of the Reynolds stresses,

$$\begin{aligned} &\frac{1}{\langle h_n \rangle}\frac{\partial}{\partial x}\left(\frac{1}{\langle h_n \rangle}\frac{\partial N}{\partial x} + \frac{1}{\langle h_n \rangle}\frac{\partial M}{\partial y}\right) \\ &\qquad - \frac{1}{\langle h_n \rangle}\frac{\partial}{\partial y}\left(-\frac{1}{\langle h_n \rangle}\frac{\partial M}{\partial x} + \frac{1}{\langle h_n \rangle}\frac{\partial}{\partial y}[N]\right), \end{aligned} \tag{4.4.2}$$

and the curl of the form stress,

$$-\frac{1}{\langle h_n \rangle}\frac{\partial}{\partial x}\left(\frac{1}{\langle h_n \rangle}\frac{\partial R}{\partial b}\right) - \frac{1}{\langle h_n \rangle}\frac{\partial}{\partial y}\left(\frac{1}{\langle h_n \rangle}\frac{\partial S}{\partial b}\right), \tag{4.4.3}$$

we show how these terms balance each other in the upper layers where the full PV eddy stress is zero; Figure 4.4.7 demonstrates how the terms balance each other. Here, M, N, R and S are defined in Equations 3.2.6. This highlights a potential flaw in attempting to parameterise $\overline{\boldsymbol{u}'q'}$ when creating a PV closure; as well as parameterising the generation of PV from smaller scales within an isopycnal layer there also needs to be communication

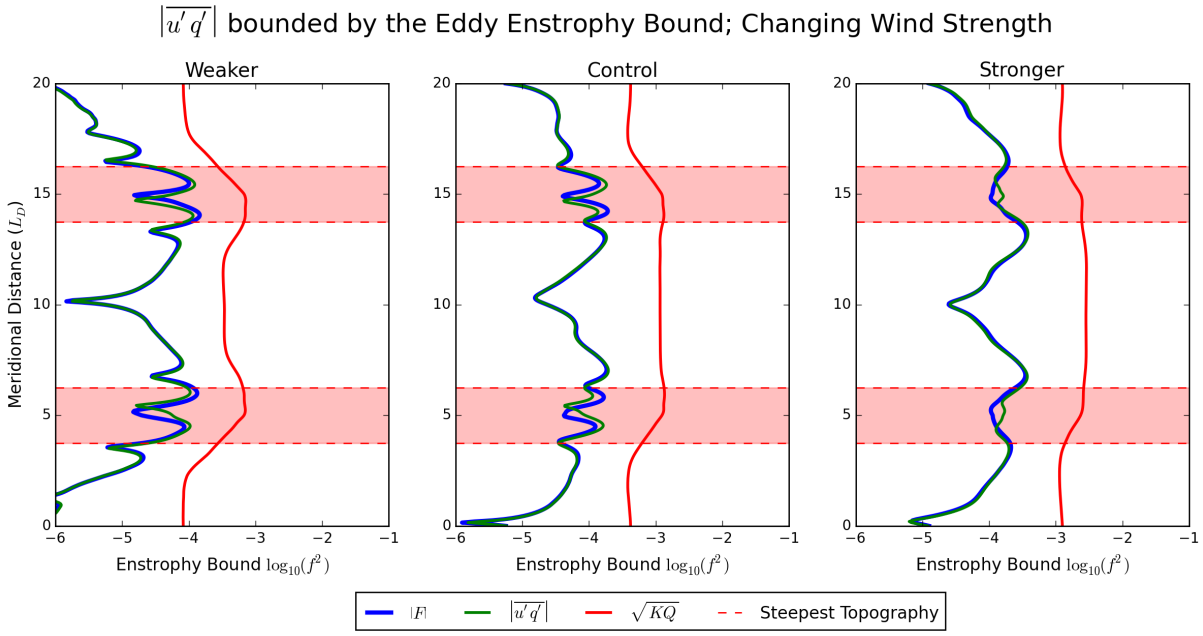


Figure 4.4.8: The norm of the eddy stresses for the mean PV and PV of the mean state with the enstrophy bound for the control and, 2× and 0.5× wind strength. Red bands show regions of steepest topography.

between layers.

From another perspective $\overline{\boldsymbol{u}'q'}$ is still useful, recall that it is a vital component to bounding the PV eddy fluxes. However, we have demonstrated that the thickness-weighted averaged PV and the PV of the mean state are similar, and hence the bound derived for $\overline{\boldsymbol{u}'q'}$ should also apply to $\mathring{\boldsymbol{F}}$. Figure 4.4.8 demonstrates how the eddy stresses, $\overline{\boldsymbol{u}'q'}$ and $\mathring{\boldsymbol{F}}$ are bounded by $\sqrt{KQ}$. Meanwhile, Figure 4.4.9 demonstrates that the bound is less-constraining than the kinetic energy bound is on the Reynolds stresses in this situation but the PV eddy stress is still around 20% of the bound, which is substantial.

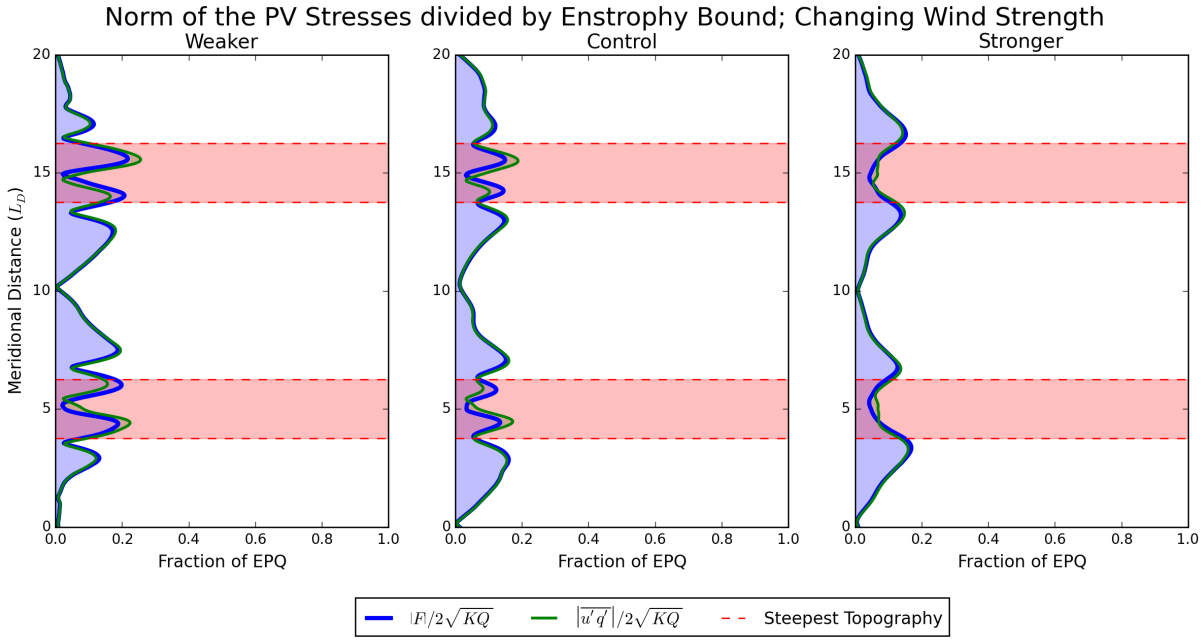


Figure 4.4.9: The ratios of the norm of the eddy stresses for the mean PV and PV of the mean state with the enstrophy bound for the control and, 2× and 0.5× wind strength. Red bands show regions of steepest topography.

Chapter 5

Conclusions and Discussion

In Chapter 1 we discussed a major failing of GCMs when attempting to model the Arctic Ocean. We compared the observed circulation with typical output available from a GCM and noted that the AWL in these models is often woefully different from observations. We then explored possible explanations for the cyclonic circulation observed in the AWL including the PV budget suggested in Yang (2005) before settling on the role of eddies in generating flow along topography. From this it is possible to conclude that the error present in the AWL of GCMs is due to the models not fully resolving the eddy field. Since fully resolving the eddy field would require more computing power than is available with present technology we suggested that an improvement in the parameterisation of the effect of eddies on the large scale flow is required to achieve more accurate GCMs.

The next chapter was therefore a brief overview of eddy-mean flow interaction theory. Beginning with the problems created by horizontal diffusion, we explored the development of the most successful eddy parameterisation to date, the Gent and McWilliams parameterisation. We re-derive certain attributes of the parameterisation and show that it is highly dissipative, and hence its high success due to it being very stable. However, it is clear that the parameterisation is no help to us as the along-topography flow observed in the Arctic Ocean is clearly generated by a mechanism that is not dissipative. We therefore followed the works of Greatbatch (1998), Adcock and Marshall (2000), Young (2012), Marshall et al. (2012) and Maddison and Marshall (2013) in attempting to develop a

parameterisation that, rather than being purely dissipation, correctly encapsulates mean-eddy interactions. The work discussed in this Chapter lead the reader to three main questions:

- To what extent does finite eddy energy inhibit the ability of eddies to generate a mean along-topography flow?
- To what extent is the topographic slope the controlling factor for the structure of the eddy stresses in eddy-mean flow interactions over variable bottom topography?
- To what extent is $\mathring{q} \sim \overline{q}$, and so does the enstrophy bound holds for $\mathring{F}$? And hence, to what extent are the eddy stresses inhibited by the available eddy potential enstrophy?

To answer these hypotheses, eddy-mean interaction theory was developed in Chapter 3 specifically for the stacked shallow water equations. Problems were encountered, such as how to define potential energy, whilst a configuration was created which allowed for an eddy field to be generated over topography with the smallest amount of complexity. By generating a temporal and spatial varying random wind stress with zero mean, an eddy field was able to be generated without first creating a large-scale flow. Then it was possible to diagnose the eddy stresses to demonstrate how an eddy field is involved in generating along-topography flows.

Firstly, we changed the strength of the wind stress, effectively increasing or decreasing the input of eddy energy. As one would expect, the bottom friction increased and decreased in magnitude to match the changing input of eddy energy. But also it was demonstrated that increasing wind stress allowed for more available eddy energy, which meant the eddy stresses were less constrained whilst by decreasing the wind stress would constrain the eddy stresses much more. We also discovered that the geostrophic approximation used to derive the bound on the form stress is appropriate. In the end this indicated that the eddy energy bound is a useful and constraining bound on the eddy stresses, and providing we have access to the eddy energy, probably by some ad-hoc

approximation as discussed in Section 3.2.2, it is perhaps possible to create an energy constrained parameterisation.

Secondly, we kept the wind stress, and hence the energy input, the same but varied the topography. Simply raising and lowering the height of the ridge had little or no effect on the eddy stresses. This is an indication that the eddy energy is constraining the eddy stresses, as one would expect a larger ridge would have greater along-topography flows. This could indeed be seen in Figure 4.3.6 where the magnitude of the eddy stresses are much closer to the bound when the ridge is more extreme than the control and further from the bound when the ridge is less extreme. On the other hand changing the width of the ridge slope does make a difference since the eddy stresses are focused in a much smaller region when the slope is narrow. But again Figure 4.3.8 shows how the eddy stresses are much more tightly constrained when the topography is steeper and narrower. This indicated that the eddy stresses are dependent on the strength of the topographic slope but only when they are not being tightly constrained by the available eddy energy.

Finally, it has been shown that the mean PV, $\overline{q}$, and the PV of the mean equations, $\mathring{q}$, are almost identical; and hence, the eddy stresses for the PV of the mean equations, $\mathring{F}$, is bounded by eddy enstrophy bound. However, in this situation the bound does not strongly constrain the PV eddy fluxes with the magnitude of the PV eddy stresses at about 20% of the bound. This is most likely due the particular configuration, and perhaps a model that generates a sharp PV gradient, such as a double gyre or jet in a channel, would have eddy stresses more strongly constrained by eddy enstrophy. We also noted that it is perhaps helpful to split $\mathring{F}$ into its vertical and horizontal components and that attempting to parameterise just $\overline{\boldsymbol{u}'q'}$ may be overly simplistic.

Obviously, in these experiments only a coarse sample of the possible parameter space was explored. This was mostly due to a time limitation, and if the experiments were continued they would be run with a larger number of smaller incremented, say, wind strength magnitudes to allow for a much more detailed picture to emerge of how the eddy stresses are characterised. Also, a ridge in a doubly re-entrant domain with a zero-mean

wind stress is obviously a fairly limiting case, but useful in demonstrating the eddy-mean flow interactions, and how the eddy energy and topography both are important factors in determining the eddy stresses. In future developments it will be important to determine whether the enstrophy bound can be limiting and how the eddy stresses manifest a more active environment. On top of that, the eddy fields near a domain's boundary are also likely to play a major factor and so channels or closed domains would be important to explore. Having boundaries also allows for more interesting topography such as coastal shelves more akin to the Arctic Ocean than just a ridge.

Also recall that in the derivation of the eddy stresses for the shallow water equations there is some ambiguity involving the definition of potential energy. Using an isopycnal model with more layer would help this problem, as in the limit of a large number of layers the range of values for the potential energy density function for a column in a single layer becomes vanishing small. However, whilst having many more layer would remove the ambiguity, the model would be significantly more costly in terms of time and computer power. Another problem would be that the model would have to be robust enough to deal with outcropping both between layer and with a topography - a problem that was circumnavigated by have a small number of deep layers. This is a problem which has been discussed in Dell (2010) and explored in Diehl (2012). More sophisticated isopycnal models, such as MICOM and GOLD, do exist the technical challenges associated with applying diagnostics discussed here to these models are beyond the scope of this thesis.

Overall, we have answered the hypotheses that were set out, at least for one specific situation. We have successful demonstrated that approximations made in the derivation of the eddy bounds are justified and that there are situations where the eddy stresses are strongly constrained by the eddy energy. We hope that these preliminary results can provide the seeds of a dynamically-consistent parameterisation of eddies over topography, and hence to improve the ability of ocean models to reproduce the circulation patterns observed in the AWL of the Arctic Ocean.

Bibliography

Aagaard, Ko and EC Carmack (1989). "The role of sea ice and other fresh water in the Arctic circulation". In: *Journal of Geophysical Research: Oceans (1978–2012)* 94(C10), pp. 14485–14498.

Adcock, Susan T and David P Marshall (2000). "Interactions between geostrophic eddies and the mean circulation over large-scale bottom topography". In: *Journal of physical oceanography* 30(12), pp. 3223–3238.

Andrews, DG and Mo E McIntyre (1976). "Planetary waves in horizontal and vertical shear: The generalized Eliassen-Palm relation and the mean zonal acceleration". In: *Journal of the Atmospheric Sciences* 33(11), pp. 2031–2048.

Arbic, Brian K and Robert B Scott (2008). "On quadratic bottom drag, geostrophic turbulence, and oceanic mesoscale eddies". In: *Journal of physical oceanography* 38(1), pp. 84–103.

Bönisch, Gerhard and Peter Schlosser (1995). "Deep water formation and exchange rates in the Greenland/Norwegian Seas and the Eurasian Basin of the Arctic Ocean derived from tracer balances". In: *Progress in Oceanography* 35(1), pp. 29–52.

Brannigan, Liam, David P Marshall, Alberto Naveira-Garabato, and AJ George Nurser (2015). "The seasonal cycle of submesoscale flows". In: *Ocean Modelling*.

Bretherton, Francis P and Dale B Haidvogel (1976). "Two-dimensional turbulence above topography". In: *Journal of Fluid Mechanics* 78(01), pp. 129–154.

Bryan, Kirk (1969). "A numerical method for the study of the circulation of the world ocean". In: *Journal of Computational Physics* 4(3), pp. 347–376.

Courant, Richard, Kurt Friedrichs, and Hans Lewy (1928). "Über die partiellen Differenzengleichungen der mathematischen Physik". In: *Mathematische Annalen* 100(1), pp. 32–74.

Cronin, Meghan (1996). "Eddy-mean flow interaction in the Gulf Stream at 68 W. Part II: Eddy forcing on the time-mean flow". In: *Journal of physical oceanography* 26(10), pp. 2132–2151.

Cushman-Roisin, Benoit and Jean-Marie Beckers (2011). *Introduction to geophysical fluid dynamics: physical and numerical aspects*. Vol. 101. Academic Press.

Dell, Rebecca Walsh (2010). "Abyssal mixing from bottom boundary effects in Mid-Atlantic Ridge flank canyons". PhD thesis. Massachusetts Institute of Technology and Woods Hole Oceanographic Institution.

Diehl, Benjamin W (2012). "Working Up Hills: Dynamics Over Sloping Topography With Bottom-Enhanced Diffusion". PhD thesis. Columbia University.

Duhaut, Thomas HA and David N Straub (2006). "Wind stress dependence on ocean surface velocity: Implications for mechanical energy input to ocean circulation". In: *Journal of physical oceanography* 36(2), pp. 202–211.

Eliassen, Arnt and Enok Palm (1961). "On the transfer of energy in stationary mountain waves". In: *Geofysiske Publikasjoner* 22, pp. 1–23.

Emery, WJ and J Meincke (1986). "Global water masses-summary and review". In: *Oceanologica Acta* 9(4), pp. 383–391.

Gent, Peter R (2011). "The Gent–McWilliams parameterization: 20/20 hindsight". In: *Ocean Modelling* 39(1), pp. 2–9.

Gent, Peter R and James C Mcwilliams (1990). "Isopycnal mixing in ocean circulation models". In: *Journal of Physical Oceanography* 20(1), pp. 150–155.

Gent, Peter R, Jurgen Willebrand, Trevor J McDougall, and James C McWilliams (1995). "Parameterizing eddy-induced tracer transports in ocean circulation models". In: *Journal of Physical Oceanography* 25(4), pp. 463–474.

Gerdes, Rüdiger and Ursula Schauer (1997). "Large-scale circulation and water mass distribution in the Arctic Ocean from model results and observations". In: *Journal of Geophysical Research: Oceans (1978–2012)* 102(C4), pp. 8467–8483.

Greatbatch, Richard J (1998). "Exploring the relationship between eddy-induced transport velocity, vertical momentum transfer, and the isopycnal flux of potential vorticity". In: *Journal of Physical Oceanography* 28(3), pp. 422–432.

Grianik, N, IM Held, KS Smith, and GK Vallis (2004). "The effects of quadratic drag on the inverse cascade of two-dimensional turbulence". In: *Physics of Fluids (1994-present)* 16(1), pp. 73–78.

Haynes, PH and ME McIntyre (1987). "On the evolution of vorticity and potential vorticity in the presence of diabatic heating and frictional or other forces". In: *Journal of the Atmospheric Sciences* 44(5), pp. 828–841.

Haynes, PH and ME McIntyre (1990). "On the conservation and impermeability theorems for potential vorticity". In: *Journal of the Atmospheric Sciences* 47(16), pp. 2021–2031.

Holloway, Greg (1987). "Systematic forcing of large-scale geophysical flows by eddy-topography interaction". In: *Journal of Fluid Mechanics* 184, pp. 463–476.

Holloway, Greg (1992). "Representing topographic stress for large-scale ocean models". In: *Journal of Physical Oceanography* 22(9), pp. 1033–1046.

Holloway, Greg and Zeliang Wang (2009). "Representing eddy stress in an Arctic Ocean model". In: *Journal of Geophysical Research: Oceans (1978–2012)* 114(C6).

Holloway, G, F Dupont, E Golubeva, S Häkkinen, E Hunke, M Jin, M Karcher, F Kauker, M Maltrud, Morales Maqueda, et al. (2007). "Water properties and circulation in Arctic Ocean models". In: *Journal of Geophysical Research: Oceans (1978–2012)* 112(C4).

Hughes, Chris W and Chris Wilson (2008). "Wind work on the geostrophic ocean circulation: An observational study of the effect of small scales in the wind stress". In: *Journal of Geophysical Research: Oceans (1978–2012)* 113(C2).

Iselin, CO'D (1939). "The influence of vertical and lateral turbulence on the characteristics of the waters at mid-depths". In: *Eos, Transactions American Geophysical Union* 20(3), pp. 414–417.

Jones, E Peter (2001). "Circulation in the Arctic Ocean". In: *Polar Research* 20(2), pp. 139–146.

Karcher, Michael J, Sebastian Gerland, Ingo H Harms, Mikhail Iosjpe, Hilde E Heldal, Peter J Kershaw, and Morten Sickel (2004). "The dispersion of 99 Tc in the Nordic Seas and the Arctic Ocean: a comparison of model results and observations". In: *Journal of environmental radioactivity* 74(1), pp. 185–198.

Kazantsev, Evguéni, Joël Sommeria, and Jacques Verron (1998). "Subgrid-scale eddy parameterization by statistical mechanics in a barotropic ocean model". In: *Journal of Physical Oceanography* 28(6), pp. 1017–1042.

Koszalka, Inga, Annalisa Bracco, James C McWilliams, and Antonello Provenzale (2009). "Dynamics of wind-forced coherent anticyclones in the open ocean". In: *Journal of Geophysical Research: Oceans (1978–2012)* 114(C8).

Maddison, James R and David P Marshall (2013). "The Eliassen–Palm flux tensor". In: *Journal of Fluid Mechanics* 729, pp. 69–102.

Marshall, David P, James R Maddison, and Pavel S Berloff (2012). "A framework for parameterizing eddy potential vorticity fluxes". In: *Journal of Physical Oceanography* 42(4), pp. 539–557.

Montgomery, RB (1940). "The present evidence on the importance of lateral mixing processes in the ocean". In: *Bull. Amer. Meteor. Soc* 21, pp. 87–94.

Münchow, Andreas, Humfrey Melling, and Kelly K Falkner (2006). "An observational estimate of volume and freshwater flux leaving the Arctic Ocean through Nares Strait". In: *Journal of Physical Oceanography* 36(11), pp. 2025–2041.

Nøst, Ole Anders, Johan Nilsson, and Jonas Nycander (2008). "On the asymmetry between cyclonic and anticyclonic flow in basins with sloping boundaries". In: *Journal of Physical Oceanography* 38(4), pp. 771–787.

Plumb, R Alan (1986). "Three-dimensional propagation of transient quasi-geostrophic eddies and its relationship with the eddy forcing of the time-mean flow". In: *Journal of the atmospheric sciences* 43(16), pp. 1657–1678.

Polyakov, Igor (2001). "An eddy parameterization based on maximum entropy production with application to modeling of the Arctic Ocean circulation". In: *Journal of physical oceanography* 31(8), pp. 2255–2270.

Proshutinsky, Andrey, Klaus Dethloff, Ralf Doescher, Jean Claude Gascard, and Frank Kauker (2008). "Toward reducing uncertainties in Arctic climate simulations". In: *Eos, Transactions American Geophysical Union* 89(16), pp. 150–152.

Proshutinsky, Andrey, Yevgeny Aksenov, Jaclyn Clement Kinney, Rudiger Gerdes, Elena Golubeva, David Holland, Greg Holloway, Alexandra Jahn, Mark Johnson, Ekaterina Popova, et al. (2011). "Recent advances in Arctic ocean studies employing models from the Arctic Ocean Model Intercomparison Project". In:

Proshutinsky, A, Jinpeng Yang, R Krishfield, R Gerdes, M Karcher, F Kauker, C Koeberle, S Hakkinen, W Hibler, D Holland, et al. (2005). "Arctic Ocean study: Synthesis of model results and observations". In: *EOS, Transactions american geophysical union* 86(40), pp. 368–371.

Rhines, Peter B and William R Holland (1979). "A theoretical discussion of eddy-driven mean flows". In: *Dynamics of Atmospheres and Oceans* 3(2), pp. 289–325.

Rhines, Peter B and William R Young (1982). "Homogenization of potential vorticity in planetary gyres". In: *Journal of Fluid Mechanics* 122, pp. 347–367.

Salmon, Rick (1998). *Lectures on geophysical fluid dynamics*. Oxford University Press.

Smagorinsky, Joseph (1963). "General circulation experiments with the primitive equations: I. the basic experiment*". In: *Monthly weather review* 91(3), pp. 99–164.

Smith, Richard D (1999). "The primitive equations in the stochastic theory of adiabatic stratified turbulence". In: *Journal of Physical Oceanography* 29(8), pp. 1865–1880.

Thomson, Stephen I and Michael E McIntyre (2015). "Jupiter's unearthly jets: a new turbulent model exhibiting statistical steadiness without large-scale dissipation". In: *Journal of the Atmospheric Sciences*.

Treguier, AM (1989). "Topographically generated steady currents in barotropic turbulence". In: *Geophysical & Astrophysical Fluid Dynamics* 47(1-4), pp. 43–68.

Tsubouchi, Takamasa, Sheldon Bacon, AC Naveira Garabato, Y Aksenov, SW Laxon, E Fahrbach, A Beszczynska-Möller, E Hansen, Craig M Lee, and RB Ingvaldsen (2012). "The Arctic Ocean in summer: A quasi-synoptic inverse estimate of boundary fluxes and water mass transformation". In: *Journal of Geophysical Research: Oceans (1978–2012)* 117(C1).

Vallis, Geoffrey K (2006). *Atmospheric and oceanic fluid dynamics: fundamentals and large-scale circulation*. Cambridge University Press.

Veronis, G (1975). "The role of models in tracer studies". In: *Numerical models of ocean circulation*, pp. 133–146.

Wilson, Simon J, Janine L Murray, Henry P Huntington, and Arctic Monitoring (1998). *AMAP assessment report: Arctic pollution issues*. Arctic Monitoring and Assessment Programme (AMAP).

Woodgate, Rebecca A, Knut Aagaard, Robin D Muench, John Gunn, Göran Björk, Bert Rudels, AT Roach, and Ursula Schauer (2001). "The Arctic Ocean boundary current along the Eurasian slope and the adjacent Lomonosov Ridge: Water mass properties, transports and transformations from moored instruments". In: *Deep Sea Research Part I: Oceanographic Research Papers* 48(8), pp. 1757–1792.

Yang, Jiayan (2005). "The Arctic and Subarctic Ocean Flux of Potential Vorticity and the Arctic Ocean Circulation". In: *Journal of physical oceanography* 35(12), pp. 2387–2407.

Young, William R (2012). "An exact thickness-weighted average formulation of the Boussinesq equations". In: *Journal of Physical Oceanography* 42(5), pp. 692–707.

Young, WR, PB Rhines, and CJR Garrett (1982). "Shear-flow dispersion, internal waves and horizontal mixing in the ocean". In: *Journal of Physical Oceanography* 12(6), pp. 515–527.

Zhai, Xiaoming and Richard J Greatbatch (2007). "Wind work in a model of the northwest Atlantic Ocean". In: *Geophysical research letters* 34(4).

Zhai, Xiaoming, Helen L Johnson, David P Marshall, and Carl Wunsch (2012). "On the wind power input to the ocean general circulation". In: *Journal of Physical Oceanography* 42(8), pp. 1357–1365.

Zhao, Mengnan, Mary-Louise Timmermans, Sylvia Cole, Richard Krishfield, Andrey Proshutinsky, and John Toole (2014). "Characterizing the eddy field in the Arctic Ocean halocline". In: *Journal of Geophysical Research: Oceans* 119(12), pp. 8800–8817.